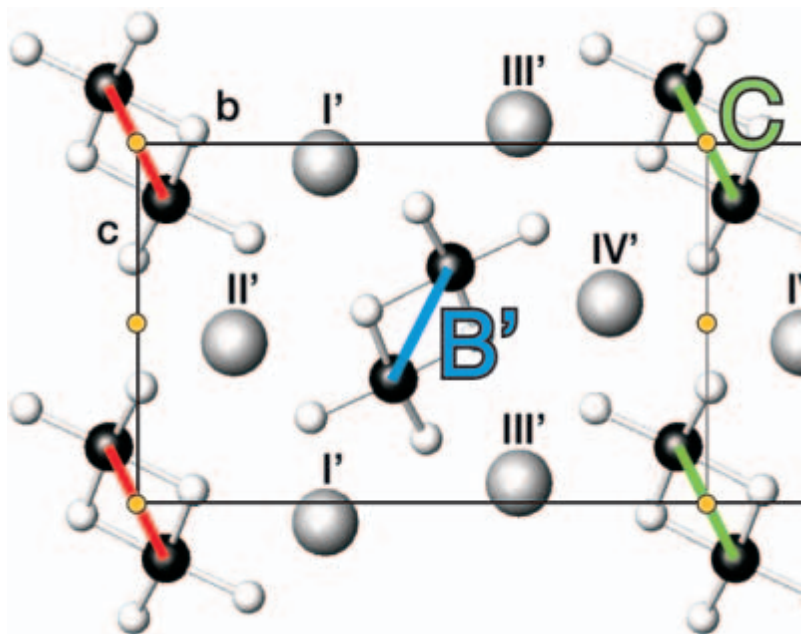
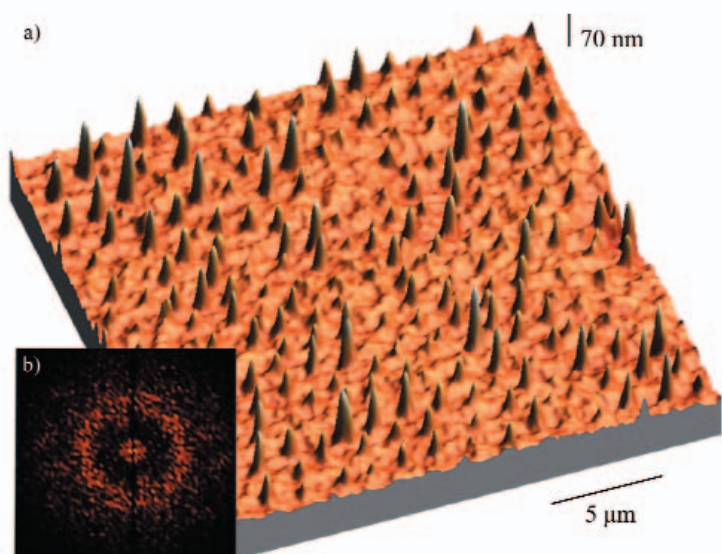
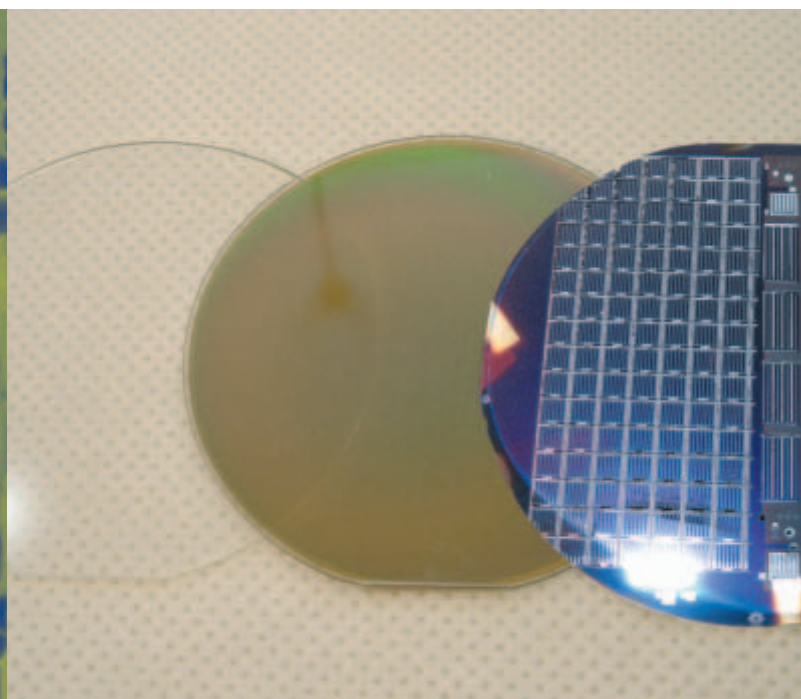
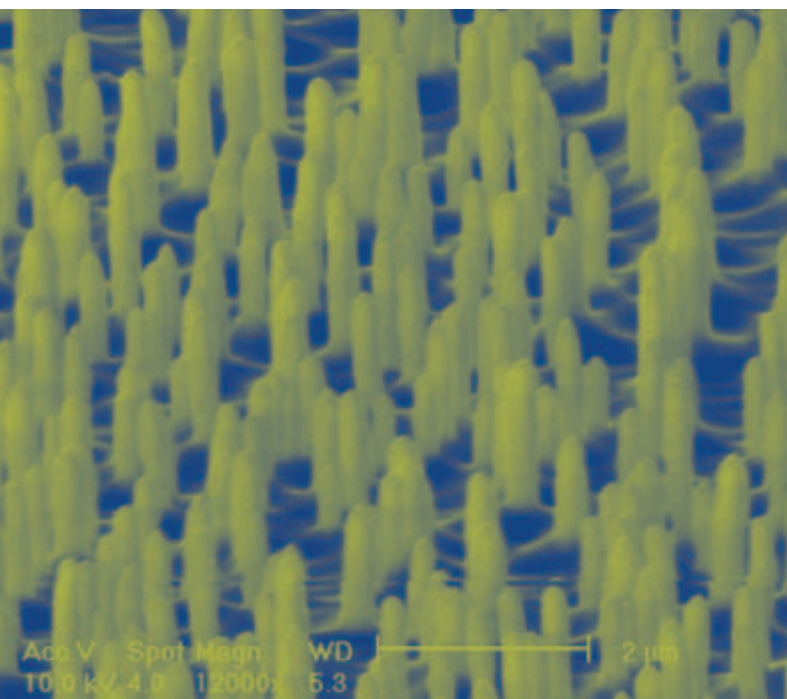


Annual Report 2004 Selected Results



Legend to Cover Figures:

- top left:** *Nano-towers* produced by fast-ion irradiation in a thin NiO-layer deposited on a SiO₂ substrate. The *towers* have diameters of approx. 200 nm and heights of 1 μm. For details see p. 43.
- top right:** The three major steps to a poly-Si thin-film solar cell on glass (substrate – seed layer – epitaxy and cell processing)
- bottom left:** Surface morphology of laser crystallized poly-SiGe
- bottom right:** Low-temperature structure of NH₄CuCl₃.
The interesting magnetic properties of this compound were investigated at HMI in 2004.

Annual Report 2004

Selected Results

Hahn-Meitner-Institut
Berlin, 2005

Table of contents

4	Foreword
6	HMI in brief
8	News and Events 2004
10	People
10	Two theorists leave HMI to take over professorships outside Berlin
10	Solar cells pioneer at SE3
11	New head of Department Magnetism
12	New Neutron Guide Hall
14	Meetings and Workshops
19	Technology Transfer
19	New application centre for industrial cooperation
20	Hahn-Meitner-Institut operates neutron scattering instrument in Munich
20	Contributing to the progress in proton therapy
21	Technology transfer prize goes to solar cell researchers
22	Public Relations
22	HMI's school lab inaugurated
23	HMI opens its doors to the public
24	Girls' Day 2004
24	Christoph Böhme receives Hahn-Meitner-Institut's Communicator Prize
25	Instrumentation News
25	First experiments at the 7 Tesla Wiggler beamlines
26	User Service
28	BENSC Operation
31	NAA Laboratory and Irradiation Service at BER II
32	ISL Operations and Developments
34	Scientific highlights Structural Research 2004
36	BENSC User Service
36	Magnetisation plateaus in the quantum magnet NH_4CuCl_3
38	Does antiferromagnetism survive in the superconducting phase of CeCu_2Si_2 ?
40	Tailoring surface coatings for protein immobilization
42	Structural explanation of the magnetoelectric phase transitions in HoMnO_3
44	ISL User Service
44	Nanoscale self-assembly of thin oxide films under swift heavy ion bombardment
46	10 years of materials analysis with heavy ions at ISL
48	NAA User Service
48	Investigation of heavy metal release during thermal waste treatment on a forward-acting grate using radiotracers irradiated at BER II
50	SF1, Methods and Instruments
50	Ordering upon melting dynamically enhanced
52	Search for scission neutrons using angular correlation method

54	■ SF2, Magnetism
54	■ Superconductivity? Just add water!
56	■ Competition of two AF structures in UNiAl single crystal
58	■ SF3, Materials
58	■ Metal foams
60	■ SF4, Structure and Dynamics
60	■ Magnetic anisotropy of Ni changed by extreme lattice expansion
62	■ Texture modification in nanocrystalline materials using swift heavy ions
64	■ Electronic energy-density effects in Auger angular distributions
66	■ SF5, Theoretical Physics
66	■ Melting of orientational order of colloidal molecular crystals on a triangular lattice
68	■ Force transduction in stiff polymers
70	■ SF6, Molecular Trace Element Research in the Life Sciences
70	■ Synchrotron light helps to elucidate the role of metalloproteins in health and disease
72	■ SF7, Nuclear Measurements
72	■ 25 years of the magnetic spectrometer Q3D
74	■ Chain states in ^{13}C and ^{14}C , nuclear polymers
76	■ Scientific highlights Solar Energy Research 2004
78	■ SE1, Silicon Photovoltaics
78	■ Laser-induced self-organization in Si-Ge alloys
80	■ Numerical simulation of thin-film heterojunction solar cells: open-source program AFORS-HET, version 1.2
82	■ Low-temperature Si epitaxy on polycrystalline Si seed layers on glass for thin-film Si solar cells
84	■ SE2, Heterogeneous Material Systems
84	■ Compositional and electronic characterisation of $\text{Zn}(\text{O},\text{OH})$ by PES for a better understanding of interfaces in chalcopyrite solar cells
86	■ Time dependent charge separation in a nanoporous TiO_2 model system studied by surface photovoltage
88	■ Electrical activity at grain boundaries of $\text{Cu}(\text{Ga}, \text{In})\text{Se}_2$ thin films
90	■ SE3, Technology
90	■ Production of CuInS_2 baseline modules on $5 \times 5 \text{ cm}^2$ substrates with high yield
92	■ Thin film photovoltaics: diagnostics and repair
94	■ Prototype development – flexible high efficiency $\text{Cu}(\text{In},\text{Ga})\text{Se}_2$ thin film solar cells for space applications
96	■ SE4, Dynamics of Interfacial Reactions
96	■ Hot electrons at the interface of p-InP
98	■ Ultrafast electron dynamics measured with femtosecond two-photon photoemission
100	■ Improved structure and performance of the InP/GaAsSb interface in a resonance tunneling diode
102	■ SE5, Solar Energetics
102	■ Reactive magnetron sputtering of CuInS_2 : a new prospective deposition method for thin film solar cells?
104	■ Surface passivation of MoS_2 or WSe_2 for optimised photoconversion efficiencies
106	■ Polymer electrolyte membrane (PEM) fuel cells: new catalysts and bionic aspects
108	■ SE6, Electronic Structure of Semiconductor Interfaces
108	■ Spectromicroscopy: investigating the ALILE process
110	■ Band structure and effective masses for CuInS_2
112	■ Organizational Chart
113	■ Imprint

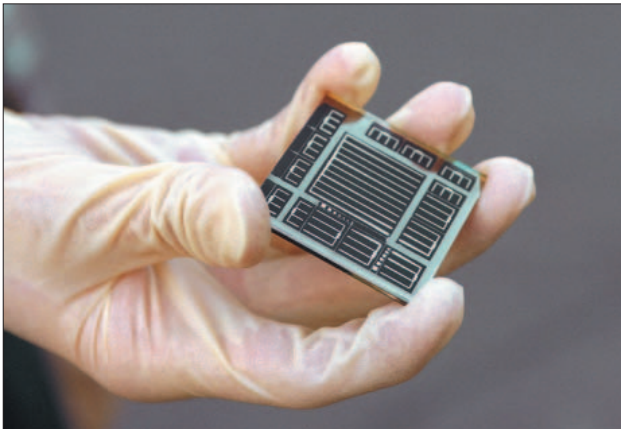
Foreword

With the Annual Report 2004 of the Hahn-Meitner-Institut, we again can present only a selection of highlights out of a large number of results. Still, we hope to help the interested reader to get an idea of the breadth and high quality of the Institute's research. Intentionally, we present results achieved by both the scientists employed at the Hahn-Meitner-Institut and the users of our facilities. It is the intimate interplay of in-house and collaborative research, which is the backbone of the top-science produced in the Hahn-Meitner-Institut.



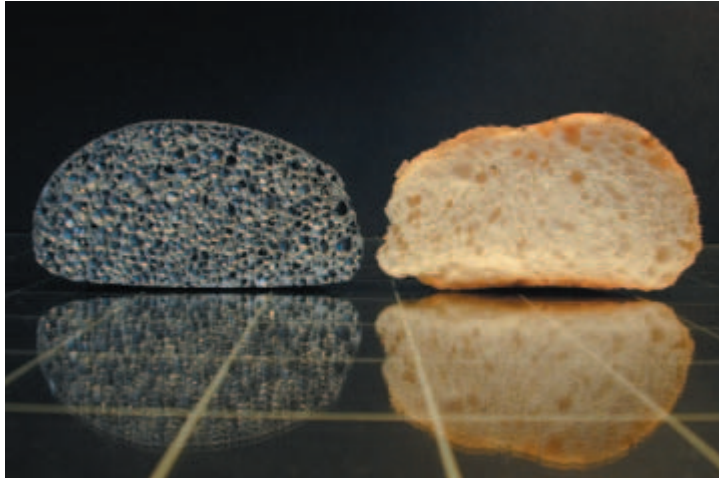
Photo: Sebastian Frenkel

For HMI and the entire Helmholtz Association, 2004 marked the completion of the new – *programme-oriented* – funding system. With *Structure of Matter* and *Key Technologies* the programmatic strategies of the remaining two out of six Helmholtz research fields were peer-reviewed. From 2005 on, the entire Helmholtz Association is funded according to the new scheme.



For Hahn-Meitner-Institut, the large-scale facilities and the major part of its division Structural Research were evaluated and the proposed programme for the period 2005–2009 got very good marks. This includes a strong support for our project N25T, to build a high- T_c -superconductivity based magnet to provide a 25 Tesla sample environment for neutron scattering experiments.

Our delight was, however, seriously damped by the recommendation, due to lacking resources and despite its scientific success, to close the Ion Beam Laboratory ISL before 2008, and to concentrate the resources on the structural research with neutrons and synchrotron radiation. Meanwhile, the deciding bodies of Helmholtz and Hahn-Meitner-Institut confirmed the shut down of ISL by the end of 2006, and we started the difficult process to realize this decision for the benefit of the future potential of the institute.



We are happy that with Dr. Schock and Prof. Tennant we could welcome two new distinguished colleagues now heading the departments SE3 (*Technology*) and SF2 (*Magnetism*), respectively. The search for the new heads of departments SE1 and SF4 is well on the way.

On the other hand, we have to announce that Prof. Frey, head of the department SF5 (*Theoretical Physics*) left Hahn-Meitner-Institut to join the LMU Munich. We will do our best to assure a continuation of the activities he started at the Hahn-Meitner-Institut over the last years.

We hope that with this Annual Report 2004 we can communicate that thanks to the very high motivation of all the staff at Hahn-Meitner-Institut and the guests and collaborators from outside 2004 was a scientifically very successful year for HMI, too. This motivation is most gratefully appreciated.

Thanks go also to the funding authorities, the Federal Government, in particular the Federal Ministry of Education and Research (BMBF), the Senate of Berlin and all the third party funding agencies for their continuing support.

By no means diminishing the difficulties due to the shut down of ISL, we are confident that the scientific achievements together with our programmatic strategy and the competence of our staff are an excellent basis for the future of the Hahn-Meitner-Institut and its standing in the community.

Michael Steiner
Scientific Director



HMI in brief



The **Hahn-Meitner-Institut** (HMI) in Berlin is one of Germany's leading centres for research on solar energy conversion, condensed matter and materials science. It has approximately 800 employees, including almost 300 scientists – most of them physicists and chemists. Most of the institute's annual budget of roughly 70 Million € is provided by the German Federal Government and the City of Berlin in a ratio of 9 to 1.

The Hahn-Meitner-Institut is member of the **Helmholtz Association** of National Research Centres, an organisation representing fifteen of Germany's largest scientific institutions. The common mission of the Helmholtz centres is to develop, set-up and operate large-scale facilities, to solve complex – often multidisciplinary – scientific and technological problems in long-term proactive research programmes and to develop high technologies for the future. The Helmholtz Association concentrates its work in six research fields: *Energy, Earth and Environment, Health, Structure of Matter, Transport and Space* and *Key Technologies*. For each of these fields, scientists develop several research programmes for 5-year periods. These programmes are then evaluated by a group of international experts. This evaluation forms the basis for the programme-oriented funding, which distributes the financial resources to the scientific programmes of the Helmholtz research fields rather than to the institutes.



Scientific work at the Hahn-Meitner-Institut is organised in two divisions reflecting the two main fields of activity: Solar Energy Research and Structural Research. The Solar Energy Research is part of the programme *Renewable Energies* within the research field *Energy*. Most of the activities of the Structural Research Division are part of the programme *Large-Scale Facilities for Research with Photons, Neutrons and Ions* in the research field *Structure of Matter*. The eye tumour therapy and the research on trace elements are conducted in the Helmholtz programmes *Cancer* and *Environmental Health* within the research field *Health*.

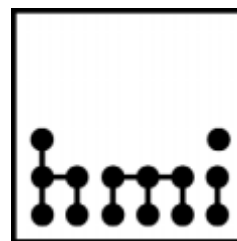
Solar energy research at the Hahn-Meitner-Institut is the largest effort in the field of sustainable energy within the Helmholtz Association and comprises approximately 25% of HMI's research and development efforts. As an interdisciplinary activity between solid state physics, material chemistry, optics and interfacial chemistry, it aims at creating scientific and technological preconditions for significantly increasing the contribution of sustainable energy to our energy supply over the next decades. This activity is taking advantage of an already well balanced research infrastructure and increasingly uses the unique measurement opportunities provided by the large scale facilities operated at the Hahn-Meitner-Institut.

At the centre of the solar energy research at HMI are materials and concepts for thin-film solar cells – activities covering the entire spectrum from basic research to the design of actual devices. The focus is on the currently most promising technologies, namely thin-film polycrystalline silicon and compound semiconductors of the I-III-VI₂ and III-V type. Research projects aim at the development of efficient photovoltaic solar cells which allow substantial reductions in the costs of solar power generation. The strategy is to develop existing thin-film technologies to a state of maturity and, in parallel, to explore new materials and concepts for solar cells of the future, e. g. nano-composite crystalline materials.



At the national level, the solar energy research programmes of the Hahn-Meitner-Institut, other Helmholtz centres, universities and other institutions are coordinated within the Solar Energy Research Association (ForschungsVerbund Sonnenenergie – FVS). In addition, the FVS represents the institutions jointly in the scientific, industrial and political communities and acts as a platform for numerous networking activities.

Structural research at the Hahn-Meitner-Institut is focused on experimental investigations of structures and materials using neutrons and fast ions as probes. These two probes are provided by two in-house large-scale facilities sited on the institute's grounds in Berlin-Wannsee: The 10MW research reactor BER II with the Berlin Neutron Scattering Center BENSC and the accelerator complex of the Ion Beam Laboratory ISL. In addition to that, the Hahn-Meitner-Institut makes use of a third complementary probe – synchrotron radiation – by operating instruments at the 3rd generation electron storage ring BESSY, an independent research institution in Berlin-Adlershof.



All facilities are primarily operated for a national and international user community. About 70 % of the beam time at the instruments is used by scientists from other research institutes, universities and industry from Germany and from abroad. It is HMI's policy to provide these users with full scale technical and scientific support, this way enabling them to make best possible use of the facilities. An outstanding highlight among the HMI activities are neutron scattering studies of samples in extreme sample environments such as very high magnetic fields and extremely low temperatures made possible by the institute's unique expertise on sample environment equipment.

At ISL, roughly a quarter of the beam time is used for the therapy of tumours in the human eye using 70MeV protons. The costs of the therapy are covered by the national health insurance companies.

Fields in the focus of in-house structural research are magnetic phenomena, properties and design of engineering components and materials, soft matter and biological systems as well as theoretical physics.



Photo: Sebastian Frenkel




NEUTR

New Neutron Guide Hall

News and Events 2004

ONENLEITERHALLE





Dr. Hans-Werner Schock
(left) together with
Prof. Michael Steiner

■ Two theorists leave HMI to take over professorships outside Berlin

Two members of HMI's department *Theoretical Physics* (SF5) have accepted professorships at German universities outside Berlin. After three years at HMI, Prof. Erwin Frey, head of the department, takes over the chair of statistical and biological physics at the newly founded Arnold Sommerfeld Center for Theoretical Physics of the Ludwig-Maximilians-University Munich. Dr. Klaus Kroy becomes professor in the condensed matter group of the Institute of Theoretical Physics at the University of Leipzig.

■ Solar cells pioneer at SE3

In October 2004, Dr. Hans-Werner Schock took up his activity as leading scientist at the department SE3 *Technology* of solar cells and modules. For solar researchers he is an old acquaintance. Being busy with Chalcopyrite solar cells, looking for relevant literature or examining the corresponding conference volumes, one will inevitably encounter the name Hans-Werner Schock. Dr. Schock ranks among the pioneers of this technology. Since the early seventies he is concerned with thin-film technologies and associated with material analytics. So far, he was active at the University of Stuttgart. Scientific inquiries led him away again and again: On behalf of the UNESCO, he was an advisor at the Universidad Nacional de Colombia in Bogotá. His last excursion led him to the Institute for Energy Conversion, University of Delaware, USA. He directed numerous national and European research projects on photovoltaics, among them the development of solar cells for space travel and a project with research institutions from the states of the Former Soviet Union. The Hahn-Meitner-Institut has been known to him for a long time: In the context of an advisory contract he held at the beginning of the nineties, he established evaporating facilities at the institute. In his new function, he would like to exhaust the potentials of the CuInS_2 technology to its borders. Despite this enormous task, there is also a chance to meet Mr. Schock outside the institute: for example in the opera, in the theatre or on the Wannsee lake, then with ice skates or a sail depending upon the water's state of aggregation.



Prof. Alan Tennant, head of the department *Magnetism* (SF2)

■ New head of Department Magnetism

On December 28, 2004, Prof. Alan Tennant took over the post of head of the department *Magnetism* (SF2). In addition, he became Full Professor at the Institute of Condensed Matter Physics at the Technische Universität Berlin.

Alan Tennant has been a regular user of the HMI facility for a considerable length of time. In the 90s, he visited the institute several times attracted by the unique possibility of performing neutron scattering experiments on samples simultaneously exposed to high magnetic fields and low temperatures. This was essential for his pursuit of measuring the exact Hamiltonian in a model-quantum-magnet and thus of bridging the gap between theory and experiment.

This multi-faceted approach to a scientific problem is typical for Alan Tennant's way of doing science. Although neutron scattering is his main method for investigating condensed matter, he has also performed synchrotron experiments and worked extensively with theorists. It is this integrated science he finds most promising, and he is excited about the idea of working at an institute providing all the most important experimental methods for his work: neutron scattering, X-ray scattering and heat capacity measurements.

Alan Tennant's fascination with scientific questions began in his childhood. Inspired by the beauty of his native Scotland he began to wonder about the workings of nature. Led by this fascination, he decided to study physics at the University of Edinburgh. His studies were followed by a PhD at Oxford about *Neutron scattering investigations of spinons* and employments

at Oxford University, Oak Ridge National Laboratory in the US, Risø National Laboratory in Denmark, the ISIS facility in England and the University of St Andrews. At ISIS, he held responsibility for developing the research programme on quantum magnetism; in St. Andrews he worked as a lecturer.

The fields of Alan Tennant's scientific interests cover a wide range of current topics in condensed matter physics, from very fundamental research to technologically relevant questions. His main interests are in quantum dominated magnetism at the nanoscale. Here, he is interested in unconventional excitations and the emergence of fractional statistics – statistics intermediate between Bose and Fermi statistics emerging in low dimensional systems. Two fields more relevant for applications are the transition between quantum and classical behaviour in nanomaterials and superconductivity, which he currently investigates on silver fluorides – systems with a structure resembling traditional cuprates.

In his work, Alan Tennant is driven by the desire to understand how nature works and is thrilled by the thought that as a scientist he can be the first one to see particular aspects of nature's behaviour. But he will not only enrich HMI by doing science himself. It is equally important for him to share his knowledge and experience with others and to create an inspiring environment in order to help other scientists and students develop their scientific creativity.



April 21, 2004

Progress of construction work



May 18, 2004

■ Construction of Neutron Guide Hall II finished

In late 2004, the construction work at Hahn-Meitner-Institut's new Neutron Guide Hall – the institute's major construction project – was completed. After the beginning of the work in autumn 2003, the foundation stone was laid in December 2003; in June 2004 the completion of the building shell was celebrated with a topping-out ceremony. The rest of the year had to be used for the interior accessories. Now that the hall has been finished, the scientists begin to install the neutron scattering instruments to be operated there. But before the start of this phase, the staff of the Hahn-Meitner-Institut had the opportunity to get an impression of the hall's interior, where the traditional New Year's reception was held.



Topping-out ceremony (June 30, 2004)

Keeping the leading role in neutron scattering in high magnetic fields

An important goal of the new hall is to secure Hahn-Meitner-Institut's leading role as provider of strong magnetic fields for neutron scattering experiments. The building's layout is adjusted to the need of accommodating a stationary magnet of the highest field. A design study for a 25 T superconducting magnet is on the way. One of the instruments in the new hall, the Extreme Environment Diffractometer (EXED), a powder diffractometer using the time-of-flight technique, has been designed to comply with the needs of experiments using such a magnet. Thanks to the novel multi-spectral beam extraction technology, to be implemented on the new neutron guide devoted to EXED, both thermal and cold neutrons will be available. This will allow access to a wide range of scattering vectors in spite of the magnet's layout limiting the scattering angles to values smaller than 30° . Despite the importance of EXED's dedication to the new magnet, it is an excellent high-resolution powder diffractometer in its own right and will add to the range of instruments at the Berlin Neutron Scattering Center BENSIC even before the magnet's arrival.

Interior view of the finished but still empty hall





September 23, 2004



Exterior view of the new neutron guide hall

Beyond magnets

The second new instrument in the Neutron Guide Hall II will be VSANS, Hahn-Meitner-Institut's second neutron small-angle-scattering instrument. The purpose of this instrument is to meet the growing user demand for experiments in the field of soft matter and biological physics. A novel collimation technique developed at the Hahn-Meitner-Institut will allow extending the range of accessible structure sizes to $1\ \mu\text{m}$, which is about one order of magnitude beyond the reach of conventional SANS instruments. Finally, the spin-echo spectrometer SPAN will move from the first neutron guide hall and benefit from the higher neutron flux and a better controlled magnetic environment in its new position.

A building with character

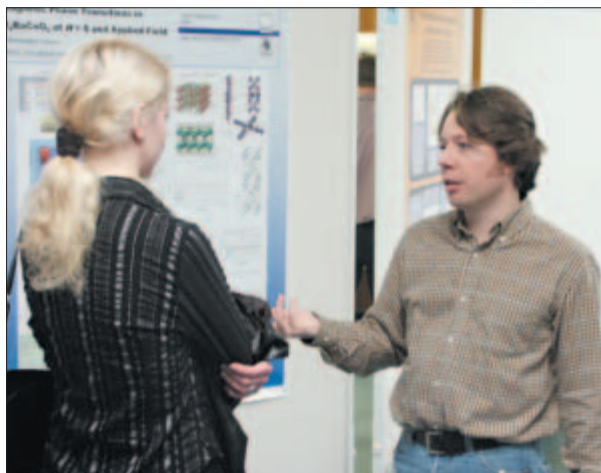
The finished hall is a large building with more than 1000 square metres, well suited for the instrumentation and its infrastructure. Architectural elements such as a bluish facade, sun-blinds and a stained glass window contribute to a friendly working atmosphere and even triggered some interest among people fascinated by modern architecture.

An investment for the future

In his address at the topping-out ceremony, the chairman of Hahn-Meitner-Institut's Supervisory Board, Dr. Hermann-Friedrich Wagner from the German Federal Ministry of Education and Research (BMBF) emphasized the institute's outstanding position in the field of research with neutrons. This position is reflected in numerous highly ranked scientific papers presenting results achieved at BENS instruments and is confirmed in the outcome of recent evaluations. The new hall with its novel instruments will ensure that Hahn-Meitner-Institut can maintain and develop this position for a dynamic future of structural research using neutrons.



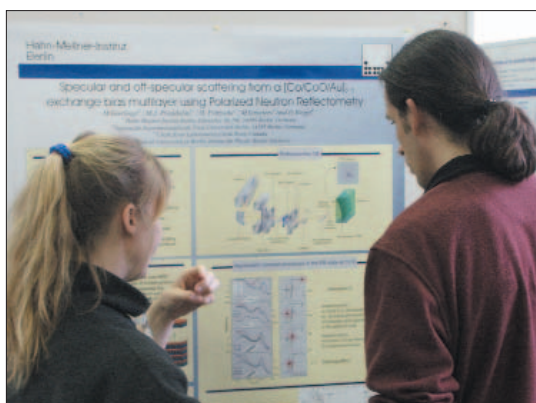
Dr. Hermann-Friedrich Wagner, the chairman of Hahn-Meitner-Institut's Supervisory Board, speaking at the topping-out ceremony



Discussions at the BENS User-Meeting

■ Meetings and Workshops

In 2004, as in every year the Hahn-Meitner-Institut invited students or researchers to come to Berlin and to participate in the institute's workshops or meetings. Many participants from Germany and abroad came and used the opportunity to learn about the science performed at the Hahn-Meitner-Institut, to present their work and to discuss with other colleagues. Here, we would like to present a brief overview of these workshops and meetings.



Discussion at the BENS User-Meeting



Future and current neutron researchers meeting at the Hahn-Meitner-Institut

The 25th Tutorial Session on Neutron Scattering

In February, BENS invited students and young researchers from different countries to take part in the 25th Tutorial Session on Neutron Scattering. During this one-week tutorial, the participants got a broad overview of neutron scattering techniques. After an introductory lecture by the BENS Director, Prof. Ferenc Mezei, the instrument scientists introduced the participants to the different neutron scattering instruments used at the Hahn-Meitner-Institut. About 30 students from 15 countries attended the course. Perhaps, some of them will come back to Berlin in the near future in order to work as Ph.D. students at HMI or to perform their own experiments as BENS users.

The 12th BENS User-Meeting

Three months later, on May 14–15, around 90 experienced BENS users came to Hahn-Meitner-Institut for the 12th BENS User Meeting. Here, they had the opportunity to present and discuss their experiments done at Hahn-Meitner-Institut's neutron scattering instruments and to get information about new developments at HMI. During the conference dinner organised at the Hahn-Meitner-Institut canteen, they had time to discuss in a relaxed atmosphere. On May 13, the Thursday preceding the User Meeting, the BENS User Committee convened in order to evaluate the submitted BENS proposals and to allocate beam time for the following half-year period.



Participants of the 3rd Berlin Workshop on Orbital Physics and Novel Phenomena in Transition Metal Oxides

New traditions – two workshops hosted for the third time

In two fields of science, there is an emerging tradition of coming to Hahn-Meitner-Institut in autumn to discuss the latest scientific results. This is reflected in the fact that two workshops organized in autumn 2004 by departments within the Structural Research Division of the Hahn-Meitner-Institut took place for the third time.

The 3rd Berlin Workshop on Orbital Physics and Novel Phenomena in Transition Metal Oxides

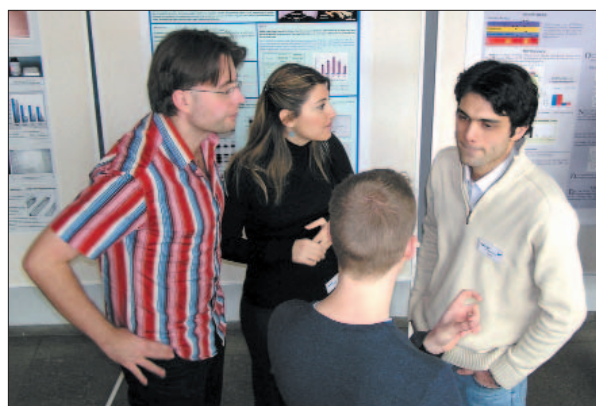
On October 6–7, the department SF2 (*Magnetism*) together with the Physics Department of the University of Hamburg invited researchers to present their latest results on *Orbital Physics and Novel Phenomena in Transition Metal Oxides*. About 40 scientists from Germany and abroad discussed current topics in this field concentrating on relations between magnetism and ferroelectricity in multiferroic oxides as well as superconductivity in Sodium Cobaltites.



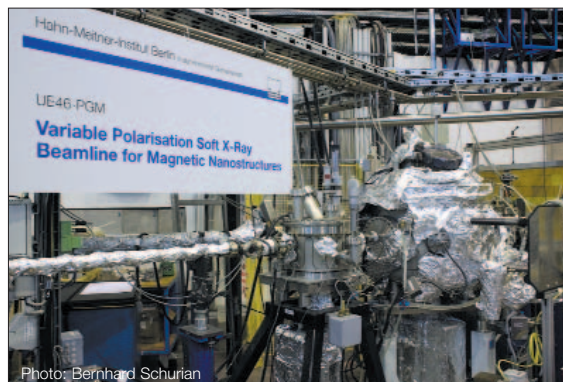
Dr. Martina Hedrich (Federal Institute for Materials Research and Testing – BAM) discussing with Prof. Dietrich Behne (HMI, SF6) during the 3rd Workshop on Metalloproteins and Metalloidproteins

The 3rd Workshop on Metalloproteins and Metalloidproteins

Almost two months later, on November 27–28, the department SF6 (*Trace Elements*) together with the GSF National Research Center for Environment and Health in Neuherberg (Bavaria) organised the third Workshop (*Herbsttagung*) on *Metalloproteins and Metalloidproteins*, which attracted scientists working in this field from Universities, Research Institutes and BioTech-Companies from all over Germany. The topics of the talks and posters covered the whole field ranging from new discoveries of the – benign or malign – roles metals play in proteins in human or animal organisms to new developments of analytic methods.



Students discussing during the 3rd Workshop on Metalloproteins and Metalloidproteins



The UE-46 PGM at BESSY operated by the Hahn-Meitner-Institut. Here, XAFS Experiments as those discussed at the XAFS-workshop are performed



The participants of the IAEA Workshop on Neutron Radiography visiting Park Sanssouci in Potsdam

Discussing instrument developments

The development and improvement of experimental instrumentation were the topics of three further workshops.

Workshop about a new high resolution time-of-flight powder diffractometer with extreme environment conditions (EXED) at the Hahn-Meitner-Institut Berlin

In May, instrument scientists working at different neutron sources came to Berlin to participate in the *EXED workshop* organized by the department SF1 (*Methods and Instruments*). The goal of this workshop was to create an opportunity for discussing the design of the powder diffractometer EXED, which will be installed in Hahn-Meitner-Institut's new neutron guide hall. The fruitful discussions among the thirteen participants will be reflected in improvements to the instrument's final design.

Status seminar Soft X-Ray XAFS at L-Edges

State of the art techniques and objectives using soft X-ray absorption methods were presented at the Status seminar *Soft X-Ray XAFS at L-Edges*, organised at the Hahn-Meitner-Institut by the department SF2 (*Magnetism*) in mid-November. Emphasis was on the physics that can be investigated at the Hahn-Meitner-Institut undulator beamline UE-46 PGM at BESSY. Twenty scientists from several countries presented their view on the investigation of magnetic properties of various materials together with underlying geometrical structures. The speakers stressed that the rapid development in this field was not only due to the availability of new synchrotron sources but also of modern methods of data acquisition and handling.

Second IAEA Research Coordination Meeting on the Development of Improved Sources and Imaging Systems for Neutron Radiography

In late July, the second meeting on the *Development of Improved Sources and Imaging Systems for Neutron Radiography* took place at the Hahn-Meitner-Institut. This series of meetings has been initiated by the International Atomic Energy Agency IAEA with the purpose of facilitating the exchange between scientists experienced in running neutron radiography instruments and those new to this field. As the meetings are particularly aimed at researchers from developing countries, one focus of the discussions were the possibilities of using cost-effective technologies.



Coffee break during the joint workshop on silicon photovoltaics. In the background: the mountains surrounding Kleinwalsertal



Dr. Hermann Schunck (Federal Ministry of Education and Research – BMBF) and Prof. Martha Lux-Steiner (Head of department *Heterogeneous Material Systems* – SE2) at the Science Forum on Renewable Energies

Silicon Photovoltaics – Joint workshop of the Hahn-Meitner-Institut and Research Centre Jülich

The Hahn-Meitner-Institut department *Silicon Photovoltaics* (SE1) and the Institut für Photovoltaik (IPV) of the Research Centre Jülich (FZJ) concentrate their research activities on the development of thin-film silicon solar cells. Whereas the IPV focuses on the development of amorphous/micro-crystalline stacked solar cells, the emphasis at the Hahn-Meitner-Institut is on the development of thin-film solar cells made of polycrystalline silicon and on the research on alternative cell concepts based on silicon heterostructures e.g. A-Si:H/c-Si-cells. Evidently, the research programmes at Hahn-Meitner-Institut and FZJ have several topics in common – a fact leading to numerous opportunities for intensive cooperation.

Based on such common topics, the 1st *Photovoltaics Workshop* – a joint research seminar of the two institutes – took place from September 19 to 24, 2004 in the Waldemar Petersen House of the TU Darmstadt in Hirschegg (Kleinwalsertal, Austria). The workshop was attended by 35 scientists and graduate students from SE1 and the IPV. Dr. S. Gall (HMI) and Dr. F. Finger (IPV) organised an ambitious programme covering the whole field: Deposition procedures and growth mechanisms of thin silicon films, the nature of defects, recombination mechanisms, surfaces and interfaces as well as solar cells. The various analytic tools and the procedures used to characterise thin-film semiconductors were discussed, too.

How science can help in the struggle against poverty The Science Forum on Renewable Energies in Bonn

In June 2004, the Solar Energy Research Association (ForschungsVerbund Sonnenenergie – FVS) participated in the *Renewables2004* in Bonn – the official international conference on scientific and political strategies to promote the renewables. The conference, which took place in Bonn, was opened by the German Federal Minister for Economic Cooperation and Development, Mrs. H. Wieczorek-Zeul, and the Federal Minister for the Environment, Nature Conservation and Nuclear Safety, Mr. J. Trittin.

Besides participating in the international conference on June 1st, the FVS was in honour bound to organise the Science Forum, a one-day satellite meeting focused on research on renewable energies. The Science Forum attracted about 300 participants from the international scientific community. Approximately one third came from developing and emerging countries. The Hahn-Meitner-Institut was represented by Prof. M. Lux-Steiner, head of the department *Heterogeneous Material Systems* (SE2), and the Scientific Director, Professor M. Steiner. Prof. Lux-Steiner chaired an excellent panel discussion with Osman Benchikh (UNESCO), Didier Mayer (EUREC Agency), Hans-Josef Fell (German Green Party – Bündnis90/Grüne), John Christensen (Risø National Laboratory and Global Network on Energy for Sustainable Development – GNESD) and Hermann Schunck (Federal Ministry of Education and Research – BMBF). In the discussion, the impact of energy politics on society and economy was highlighted. In general, the programme of the Science Forum



Panel discussion during the FVS Annual Meeting

reflected the level of awareness that the renewables among the most important resources in the struggle to overcome the lack and undersupply of energy.

In addition, the role science, research and development can play in this context was discussed. The participants agreed that the dissemination of research results on renewable energies must be improved in order to increase the share of the renewables in the energy mix.



Audience at the FVS Annual Meeting

The 2004 Annual Meeting of the Solar Energy Research Association (ForschungsVerbund Sonnenenergie – FVS)

Most topics on the agenda of the Annual Meeting of the Solar Energy Research Association (ForschungsVerbund Sonnenenergie – FVS) in November 2004 belonged to the field of research on *Hydrogen and Fuel Cells*. The FVS as a networking institution can address these topics efficiently and successfully because the member institutes perform their research activities in a strongly multi-disciplinary manner dividing the fields of research among themselves. In addition to that, the partner institutes closely collaborate with industrial companies such as BMW or Viessmann.

In his talk at this meeting, Prof. H. Tributsch (Head of HMI department *Solar Energetics – SE5*) discussed the system of fuels as well as different fuel cells. The talk attracted a great deal of attention because completely new horizons in technology and development of hydrogen systems and fuel cells were presented. At this meeting, it became once again clear that fundamental research might open up new and perhaps simple ways of solving technological problems considered so far to be insurmountable.



Brochures informing about industrial activities in the Structural Research division published within the application centre NIXE

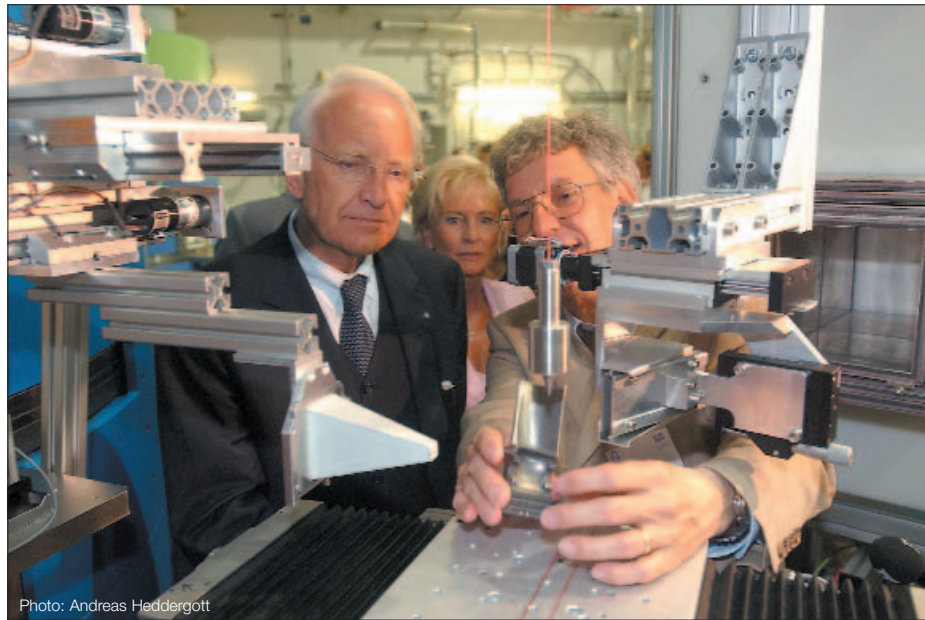
■ New application centre for industrial cooperation

Studying the structure and properties of condensed matter is the main goal of the scientific activities at Hahn-Meitner-Institut's large scale facilities. Many of the methods applied here do not only allow insights into the fundamental properties of matter but can also be highly valuable for industrial research. These methods can reveal information about technologically relevant materials that can help improve industrial products, but which is not accessible with any method available in a commercial laboratory. For example, the great value of neutron scattering is reflected in the high demand for non-destructive measurements of residual stresses deep in the bulk of engineering components, which is only possible with neutrons. Having three different probes – neutrons, ions and synchrotron radiation – at its disposal, Hahn-Meitner-Institut can operate a unique suite of instruments for investigations in materials science.

The Hahn-Meitner-Institut is strongly committed to supporting cooperations with industrial companies in the field of materials research and thus contribute with its expertise and infrastructure to the economic and technological development of the society. One result of this commitment is the installation of new instruments mainly intended for industrial use such as tomography with neutrons or synchrotron radiation.

In order to promote its offer among potential industrial users, HMI has founded the new application centre NIXE (Neutrons, Ions and X-Rays for Engineering). NIXE's main task is to identify possible applications for the methods and to establish contacts with the relevant industrial companies. Until now, NIXE has published several information flyers presenting the scope of particular methods. For the coming year a workshop for industrial partners is planned to take place at HMI. It will give the participants the opportunity to discuss their questions and ideas with the institute's scientists and to get a first-hand impression of the instrumentation used for the experiments. In addition to its role in promoting the industrial offer, NIXE acts as a first contact for industrial users offering advice on the choice of the right method and the possible forms of cooperation.

The Bavarian Minister-President Edmund Stoiber (left) and Prof. Winfried Petry, Scientific Director of the Neutron Source FRM-II, at the instrument Stress-Spec operated jointly by Hahn-Meitner-Institut and Technische Universität München at FRM II



■ Hahn-Meitner-Institut operates neutron scattering instrument in Munich

The investigation of residual stresses is one of the most successful fields of industrial cooperation in Hahn-Meitner-Institut's Structural Research division. In October 2004, the new instrument Stress Spec dedicated to stress measurements was put into operation at the research reactor FRM II in Garching near Munich. Stress Spec, operated jointly by the Hahn-Meitner-Institut and the Technische Universität München, complements the two instruments for residual stress determination operated at the research reactor BER II in Berlin.

Residual stresses are internal stresses created in engineering components during the manufacturing process. These stresses strongly influence the reliability of the components during operation, with the effect being either beneficial or detrimental depending on the exact nature and distribution of the stresses. Therefore, an exact knowledge of the stress distribution is extraordinarily valuable for the manufacturers.

Residual stresses can be determined by means of neutron scattering because they lead to distortions of the crystal structures in the component. When compared to all other methods for measuring the internal stresses, neutron diffraction has two main advantages: it is non-destructive and it provides information about the three-dimensional stress distribution deep in the bulk of the sample.

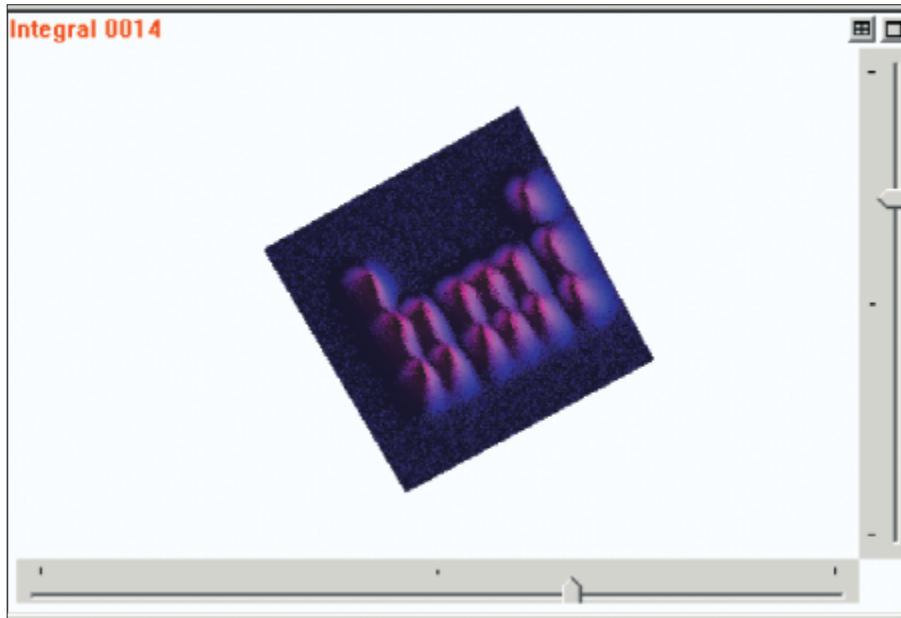
With its engagement in Garching, HMI secures its leading position as provider of services in the field of non-destructive testing reflected in the high demand for

stress measurements from the automotive, aircraft and space industries. By operating three instruments at two neutron sources, the institute can ensure reliable and fast access to the facilities. The instruments used for the determination of residual stresses with neutrons are supplemented by a new instrument using synchrotron radiation at BESSY. This instrument allows determining the stresses in the vicinity of the sample's surface.

■ Contributing to the progress in proton therapy

Since 1998, the Hahn-Meitner-Institut is operating Germany's only proton therapy facility. The proton beam used for the therapy of eye tumours is created in HMI's ion accelerator centre ISL, which most of the time acts as a source of ion beams for scientific experiments. Since the beginning of their activity, the members of the tumour-therapy team did not only treat more than 500 patients but also acquired a unique experience and expertise. This expertise and the high quality of the available proton beam attracted ACCEL Instruments GmbH to come to Hahn-Meitner-Institut in order to test a technique that will be used in a dedicated tumour therapy facility, which is currently under construction in Munich.

Whereas at HMI a narrow proton beam is first widened and then sent through an aperture representing the shape of the tumour, a scanning technique will be used in the new facility. Here, the proton beam is deflected by a system of magnets and thus scans the whole tumour volume. This active technique allows for a more accurate covering of the tumour and helps save resour-



The logo of the Hahn-Meitner-Institut written with a proton beam from ACCEL's scanning set up

ces: no material has to be used for tailor-made apertures and the complete current of the proton beam is used for therapy.

With this cooperation between the Hahn-Meitner-Institut and ACCEL, HMI's tumour-therapy team contributes to the development of the proton therapy technique even beyond the treatment of eye tumours – their traditional field of expertise.

■ Technology transfer prize goes to solar cell researchers

In 2004, the technology transfer prize of the Hahn-Meitner-Institut was awarded to Dr. Nikolaus Meyer, Dr. Ilka Luck, Dr. Rainer Klenk, Dr. Roland Scheer, Joachim Klaer and Prof. Martha Lux-Steiner from the institute's Solar Energy Division for their work with the title *Producing innovative thin-layer modules the way architectural glass is produced – Founding Sulfurcell Solartechnik*.

The laureates were the first to succeed in making efficient solar modules using Copper-Indium-Sulfide (CIS) deposited on window glass as absorber material. They thus introduced an unusually simple and robust manufacturing process that led to a reduction of the production costs for solar modules by half. In addition to developing the scientific basis for the production of the innovative modules, the laureates were successful in putting together a consortium of renowned investors funding the industrial implementation of their inventions.

The laureates were selected by a jury composed of representatives of industrial companies, the Chamber of Commerce and Industry and the Technology Foundation Berlin. The main criteria for the selection were the project's innovation potential and the prospects of using the new process on an industrial scale.

The prize was presented to the laureates in a prize-giving ceremony in HMI's lecture hall. In his welcome address, Prof. Michael Steiner emphasized the increasing importance of the transfer of knowledge between scientific institutions and industrial companies and the institute's commitment to support the industrial use of results achieved by scientists active at the Hahn-Meitner-Institut. The laureates received the prize from Mr. Joachim Hübscher, member of the management of Siemens Business Services GmbH & Co. OHG Region Ost. The prize money – 5000 € – had been donated by Siemens AG. At the end of the ceremony, Dr. Meyer presented the long path leading from the very first ideas to the beginnings of the industrial production of the novel modules at Sulfurcell Solartechnik.



Klaus Böger, Berlin's Senator for Education, Youth and Sport, visiting HMI's school lab



Prof. Michael Steiner at the school lab

■ HMI's school lab inaugurated

On September 29, 2004, Klaus Böger, the Senator for Education, Youth and Sport of Berlin and Prof. Michael Steiner, the Scientific Director of the Hahn-Meitner-Institut, officially inaugurated the institute's school lab *Blick in die Materie* (Looking into Matter).

The school lab offers pupils from secondary schools the opportunity to perform physics experiments close to real science and often far beyond the usual syllabus of science education at school. Here, the young visitors have the chance to do scientific work on their own and to develop their creativity in approaching and solving scientific problems. The pupils receive support from the lab's staff: a physics teacher and a research scientist from HMI.

The typical visit to the learning lab is the project day (Projekttag) – a group of around 20 pupils come to HMI for one day; they spend the morning performing the experiments and have a guided tour of the institute in the afternoon and, thus, get a taste of the atmosphere at a large scientific institution. In the days preceding their visit, they prepare and discuss the experiments in class using the materials provided by HMI.

The experiments at the school lab cover a broad range of topics from different fields of scientific research at the Hahn-Meitner-Institut, among them solar energy, magnetism and superconductivity. The young experimentalists build and investigate solar cells, determine the critical temperatures of superconductors and study the magnetic properties of matter. The school lab is well equipped with modern experimental instrumentation. One of the highlights of the equipment is the scanning tunnelling microscope used for investigations of the atomic structure of surfaces, e. g. of pyrolytic graphite.

The goals of the school lab are twofold. On the one hand, the lab makes a contribution to secondary school science education and helps foster the interests of young people in natural sciences. On the other hand, the establishment of the lab contributes to the HMI's visibility in the public. By supplementing the offer provided by secondary schools, the institute takes responsibility in a field beyond its usual activities but is very relevant for the development of modern society. This way, interest in the institute's work is triggered among people usually not following recent developments in the world of science. This interest was reflected by the coverage of the inauguration ceremony in the local media. Also the pupils themselves act as young ambassadors of the institute by telling their families and friends about the day in the lab and thus spreading the word about HMI and its research.

Scientists from the department *Silicon Photovoltaics* presenting their work during the *Lange Nacht der Wissenschaften 2004*



■ HMI opens its doors to the public

Many of the experiments at the school lab are relatively easy to perform and to transport. Thus, they can be used to present the main fields of HMI's scientific activities at the institute's Open Day or other popular science events such as the annual ScienceFair in central Berlin. This way, the school lab also facilitates the exchange between the institute and the general public interested in science.

The founding and operation of the school lab has been made possible by financial support from the Helmholtz-Association. Until now, the Helmholtz-Association has contributed a sum of 340,000 Euros.

By opening the school lab, HMI tries to fill a gap felt by Berlin's science teachers. This is reflected by the fact that already in the first months of the lab's operation the demand exceeded the available time. This was even before the lab had been officially inaugurated and the information about its existence was spread by word of mouth only.

Visiting the experimental halls around HMI's research reactor or watching how small metal cubes can be turned into metal foams are only two examples of the attractions offered to the visitors of HMI's Open Day on June 12, 2004. Following a long standing tradition, HMI invited neighbours, friends and the general public to visit the institute and to get a first-hand impression of the research performed here. The institute's scientists enjoyed the opportunity to show their labs and explain their work to an interested and often very impressed audience. Guests interested in doing experiments themselves, had their chance at the school lab. About 1000 people visited the institute in Berlin-Wannsee.

The department of *Silicon Photovoltaics* (SE1) in Berlin-Adlershof participated with most other scientific institutes in Berlin in the annual *Lange Nacht der Wissenschaften*, which took place on the same day. Out of the 12000 people who found their way to Adlershof, more than 3000 flocked to HMI's department in order to learn how new technologies for solar cells are developed.



Scientific discussion during the *Girls' Day*

■ Girls' Day 2004

For the fourth time, the Hahn-Meitner-Institut invited schoolgirls aged between ten and sixteen to participate in the *Girls' Day*. 60 girls came on April 22, 2004 to learn more about the broad variety of professions and topics at the institute.

First, they got an introduction to the institute (its history, structure and the scientific topics investigated at the institute). Then, seventeen groups were formed and shown the labs, offices and workshops. The girls had the opportunity to perform experiments, prepare something or collect data; they could get information about different professions and careers. Every girl could select three groups to learn more about lasers, solar cells, the preparation of a metallic trinket by CAD, designing a web-site or many other activities. In addition, some girls had the chance to visit the canteen and to learn how a canteen works and how lunch and refreshments are prepared.

At two o'clock all girls went home happily and the organizers were satisfied with the commitment of all their colleagues taking part in the arrangement of that day.



Prof. Rolf Scharwächter presents the Communicator Prize to Christoph Böhme.

■ Christoph Böhme receives HMI's Communicator Prize

Christoph Böhme, a former PhD student and now post-doc at the HMI department *Silicon Photovoltaics* (SE1) received the 2004 Communicator Prize of the Hahn-Meitner-Institut. The Prize is awarded every second year for the best popular presentation of the results of PhD research achieved at HMI. The winner is selected by a jury consisting of scientists, communication specialists and secondary-school pupils. The prize was presented in a ceremony on July 9, 2004 after the candidates' presentations. The Communicator Prize was not the first award Böhme received for his thesis *The Dynamics of spin-dependent charge carrier recombination*. In 2003, he won the Adlershof thesis award and in 2004 the science prize of the chamber of commerce and industry of Northern Hesse.



Fig. 1: The new materials science beamline EDDI operated by the Hahn-Meitner-Institut at BESSY

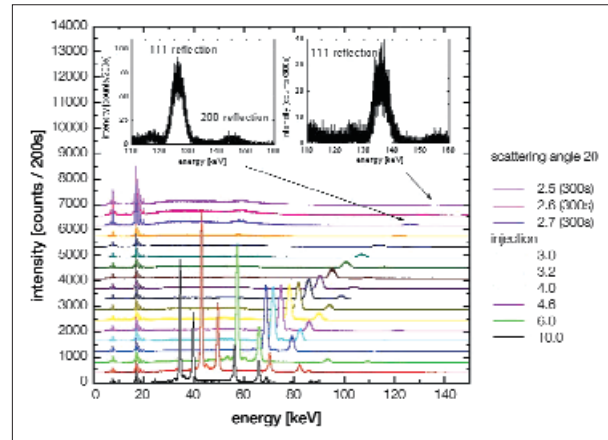


Fig. 2: Energy diffraction spectra of the alloy In718 obtained at the materials science beamline EDDI. The measurements were performed for different scattering angles 2θ at a wiggler field of 6 T. In this case, the peak position can be determined reliably for energies up to approximately 135 keV. With the full wiggler field of 7 T, energies of up to 150 keV can be used.

■ First experiments at the 7 Tesla Wiggler beamlines

In the course of 2004, the two HMI beamlines installed at the 7 Tesla wiggler at the Berlin electron storage ring BESSY in Berlin-Adlershof went operational. Following the radiation safety O.K. in April, commissioning of the instruments was started. The complex beamline instrumentation, for example an x-ray optics consisting of a silicon double crystal monochromator, two 1 m long bendable silicon mirrors polished to nanometer surface roughness, and many more components, required extensive testing. Since September 2004 the wiggler itself is operated continuously at its maximum field of 7 Tesla, allowing the HMI scientists responsible for the operation of the instruments to perform first successful test experiments.

Fig. 3: MAGS, the new instrument for resonant magnetic scattering operated by the Hahn-Meitner-Institut at BESSY

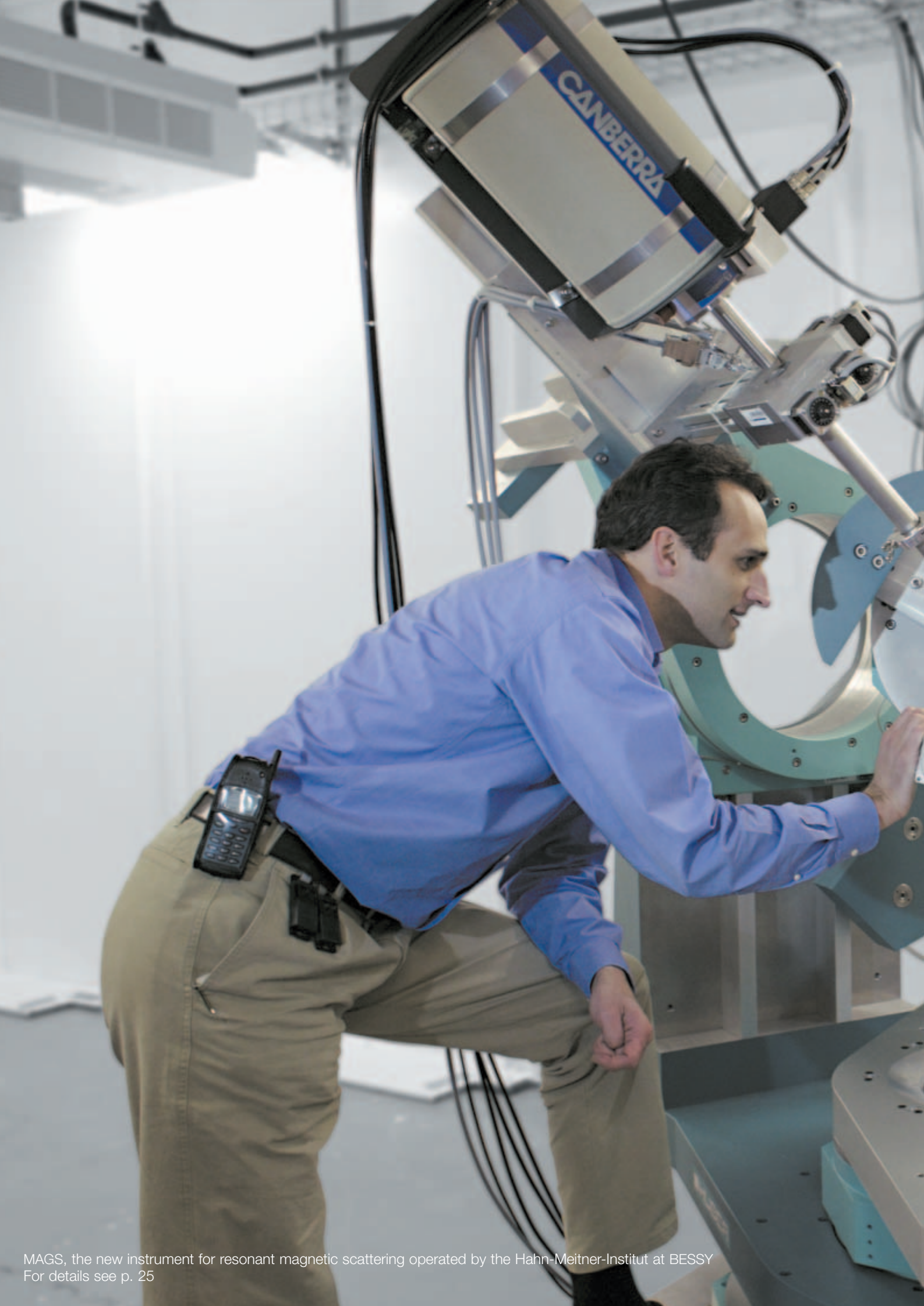


Photographs on this page:
Bernhard Schurian

The materials science beamline for **E**nergy **D**ispersive **D**iffraction (**EDDI** – see Fig. 1) was designed for the investigation of residual stresses and the microstructure in materials of technical importance. With photon energies above 100 keV, the x-rays may penetrate several hundred micrometers into the sample. This closes the experimental gap between conventional laboratory sources and neutron scattering techniques. First data taken at EDDI proved that data can be taken up to x-ray energies of 150 keV (Fig. 2), surpassing all expectations and allowing even for experiments in transmission geometry, in which the x-ray beam passes through the sample.

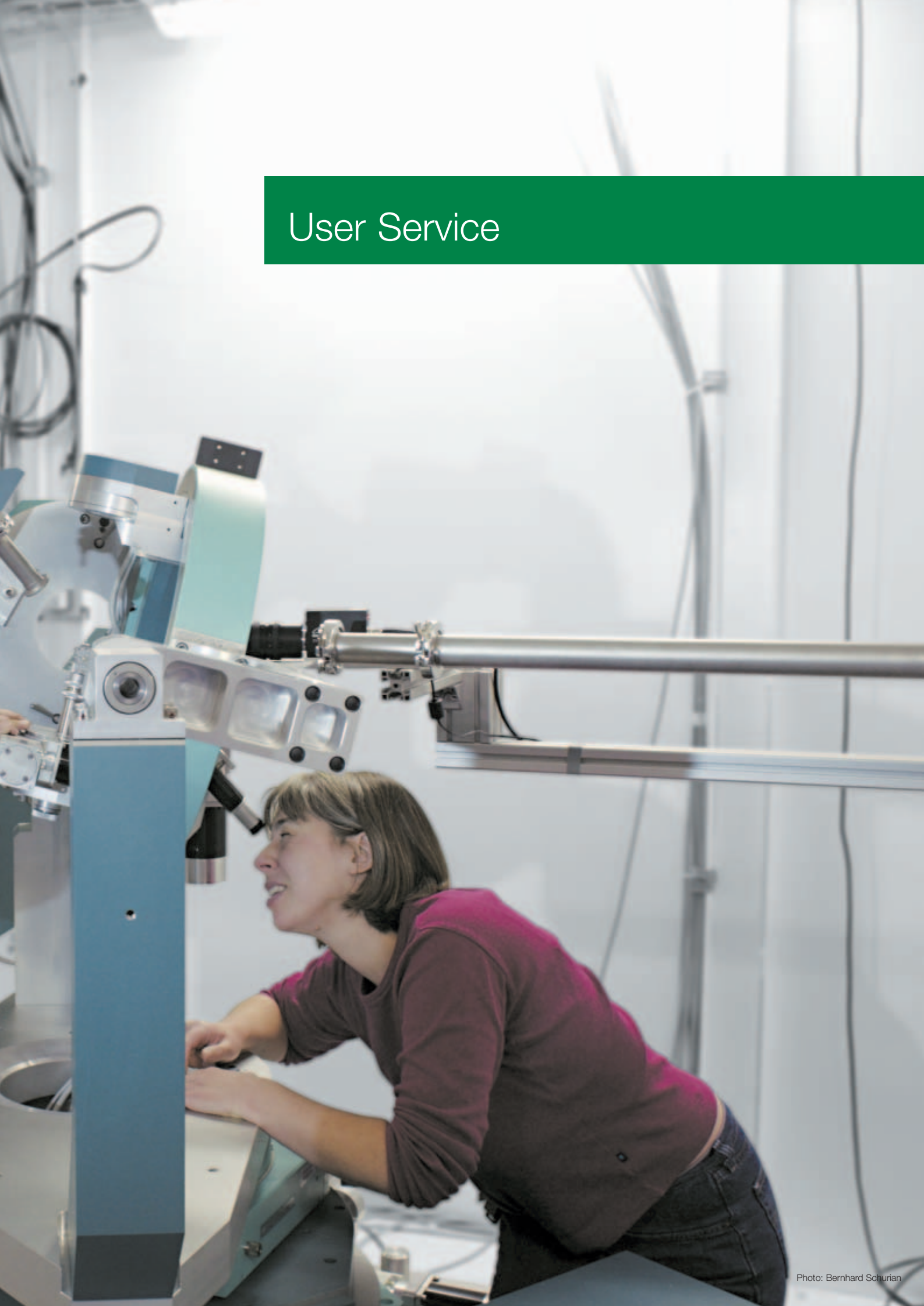
The beamline for high-resolution diffraction and resonant **M**agnetic **S**cattering (**MAGS**) is intended to be used mainly for the investigation of the interplay of various types of ordering phenomena like magnetism or superconductivity in metal oxides and intermetallic compounds. First test experiments taken at temperatures down to 6 K showed that the high intensity of the beam allows for the detection of even very weak signals which are produced, e.g., by small structural distortions induced by magnetic ordering.

Both beamlines are now ready for user service starting in April 2005. Like for the neutron scattering instrumentation at BENS in Wannsee, 70% of the available beam time will be offered to external users from universities and other research institutions. During their experiments, the guest scientists will be supported by HMI beamline staff.



MAGS, the new instrument for resonant magnetic scattering operated by the Hahn-Meitner-Institut at BESSY
For details see p. 25

User Service



BENSC Operation

Director: Prof. Ferenc Mezei

It is the mission of the Berlin Neutron Scattering Center (BENSC) to develop and operate the scientific instruments at the Berlin research reactor BER II. BENSC is open to both, the national and the international user community, whereby about 70% of the beam time is available to external users: 20% for long term collaborating groups from German universities and other research institutions and 50% for peer reviewed short term projects.

Allocations 2004 for short-term projects	accepted projects	allocated days
Germany	34	212.5
EU + Assoc + CH	68	508
RU	5	71
USA, AU, JP	11	94.5
	116	886

Table 1: Allocation of BENSC beam time for short term projects

Profile of BENSC

The profile of BENSC is characterized by the exceptionally wide range of the **instrumentation**, which allows experiments to be performed in many areas ranging from basic to applied research. Several advanced BENSC instruments provide neutron intensities and resolutions competitive with the best available worldwide, including those operating at high flux reactors. Most of the instruments have the option of using polarized neutrons. Examples for unique advanced instrument options are, e.g.,

- the polarized neutron option SANSPOL
- the multidetector option the time-of-flight spectrometer NEAT
- the spin-echo instrument (SPAN) with the wide-angle NSE option
- the flat-cone diffractometer
- and especially the sample environment.

The leading role of BENSC for sample environment at extreme conditions is accepted worldwide: Experiments can be performed over a very large range of temperatures and/or magnetic fields. The temperature range for routine use is 30 mK to beyond 2000 K; magnetic fields up to 17.5 Tesla have been made available to routine user operation. At present, two magnetic cryo-

stats operated at BENSC ($1.5\text{ K} < T < 300\text{ K}$) with split pair superconducting magnets and vertical fields up to 17.5 Tesla are the world's leading magnet systems for neutron scattering.

Detailed descriptions of all essential BENSC neutron scattering instruments are available – and updated – on the BENSC Webpage: <http://www.hmi.de/bensc/instrumentation>.

A colour printed version (brochure HMI-B 577) has been published in March 2001 and is available on request.

BENSC puts special emphasis on sample environment under extreme conditions: high fields, high pressure, high, low and ultra low temperatures. The sample environment group has published a detailed technical handbook on BENSC sample environment. The handbook is updated continuously and available on the internet under <http://www.hmi.de/bensc/sample-env/home.html>

Extension of BENSC User Service to HMI instruments at BESSY

To promote complementary use of neutrons and synchrotron radiation, the Hahn-Meitner-Institut had initiated an upgrade project for the synchrotron source BESSY including the development and installation of two new insertion devices.

The HMI UE46 undulator provides polarized soft X-rays with, by orders of magnitude, worldwide highest brightness and flux density. The undulator is operational since 2002, with full user service at the PGM-beamline for magnetic nanostructures and magnetic films. The delivery of the high field magnet for the reflectometry option is now expected for 2005. The use of this beam line is detailed in table 2.

	weeks	
HMI in-house research Structural Research	13	36 %
HMI in-house research Solar Energy Research	1	3 %
External Users under BESSY and BESSY in-house research	22	61 %

Table 2: Distribution of 2004 experiment time for the UE46-PGM beam line at BESSY

The second insertion device, a 7 T-Wiggler, went operational in 2004. The Wiggler provides X-rays for two beam lines:

- White beam for the Materials Science Diffractometer EDDI
- Monochromatic beam for Resonant Magnetic Scattering and High-resolution Diffraction (MAGS). The user service at the Wiggler beam lines will start in April 2005. (See p. 25 for details.)

New Neutron Guide Hall

The construction of the new neutron guide hall advanced in big steps. With the foundation ceremony for the building already held on December 8, 2003 due to the relatively mild winter 2003/2004, the progress had been very quick, and with the end of the year the new hall was completed. See p. 12 for further information.

It is foreseen that the Wide-Angle Spin-Echo Instrument V5 will move from the old hall to the new hall. Other planned – and fully financed – instruments in the new hall are VSANS – High resolution SANS, equipped with a novel focusing technique – and EXED – Extreme Environment Diffractometer equipped with TOF-monochromatisation. The experiment site for EXED is in addition foreseen for the project of a 25 T high field magnet.

BENSC User Service

The BENSC user services provided for scientists of German universities and other national and international research institutions include

- Allocation of beam time to individual (*short term*) projects of external groups on the basis of peer reviewing by an international user committee and extensive scientific and technical support for the preparation, the experiments and the data evaluation. Logistic support and travel support for young researchers is provided.
- Long-term scientific and technical projects on the basis of co-operation agreements.

An amount of at least 50 % of the beam time of the 14 most important instruments operated by BENSC is reserved for individual scientific projects; up to 20 % of the beam time would be made available for long-term co-operation projects.

Long-term co-operations

Long-term co-operation projects are primarily in the interest of the respective co-operations partners; but they also increase the manpower at BENSC and broaden the capacities for scientific support to the external users. In the path breaking field of soft matter research for instance, which formerly was not a core field of Hahn-Meitner-Institut's own scientific programme, BENSC has established close collaborative links with the Institute of Biochemistry, TU Darmstadt; Institut für Physikalische Biologie, Univ. Düsseldorf; Iwan-N.-Stranski Institute of the TU Berlin; Max-Planck Institute of Colloids and Interfaces in Golm/Potsdam.

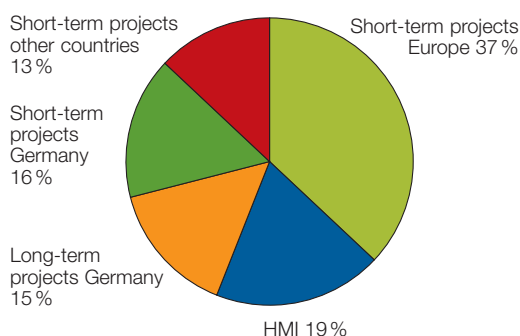


Fig. 1: Distribution of BENSC instrument time

Individual short-term research proposals of external users

It is the key issue of the BENSC user service to provide external groups with beam time and intensive scientific support for individual scientific experiments. This service is meant for both German groups and the international scientific community. The inclusion of new applications for beam time is decided by an internationally composed scientific selection panel. For 2004, more than 110 short-term projects of external users have been accepted by the panel (see table 1). The number is lower than in 2003 because of the 3-months-shut-down of the research reactor BER II at the end of the year, required for the replacement of cold neutron guide 4 in connection with the BENSC upgrade project Neutron Guide Hall II.

Co-operation with Industry

The support for industry is mainly based on co-operation agreements, where the partners provide the samples and in return profit from the highly specialized know-how of the BENSC staff and from the advanced analytical methods available at BENSC, with use of neutrons and with complementary use of X-ray or synchrotron radiation.



Photo: Sebastian Frenkel

Fig. 2: The triple axis spectrometer FLEX

Support for European Access to BENSCH from the European Commission

Right from the start of BENSCH user operation in 1993, the access of European research groups to BENSCH has been generously supported by the European Community under framework programmes FP3, FP4, and FP5 of the European Commission – with the values of the BENSCH access grants increasing from contract to contract.

The EU support is available for groups from European Member States as well as for groups from the Associated States. Within the 4 years of the FP5 contract period under the *Access to Research Infrastructures* action of the *Improving Human Potential Programme* (IHP), formally ending in February 2004, BENSCH delivered a mean annual amount of roughly 550 instrument days to the European research groups, distributed to ~80 different projects/year with a total of ~175 visits/year.

The successful European Access to BENSCH actions are now continued under the 6th EU Framework Programme (FP6) in a slightly modified contractual situation: BENSCH is now a partner in the ***Integrated Infrastructure Initiative for Neutron Scattering and Muon Spectroscopy (NMI3)***. NMI3 brings together 23 partners from 14 countries, including 11 research infrastructures, together with other interested organisations. The most important branch of NMI3 includes 12 different access activities offering European users approximately 5000 beam days of access to 150 instruments at different facilities, with support for travel and subsistence. Under NMI3 BENSCH will serve for a minimum access of 1040 instrument days.

In the first year (reactor operation period Jan.–Sept. 2004) under NMI3, BENSCH delivered already 480 instrument days for European users. A total of 117 individual users from 55 groups from 14 countries have been involved, the majority of these EU supported users, 72 individual researchers, were new users.

Scientific results of external users at BENSCH

The scientific interim reports on most recent experimental results provide rapid dissemination of the BENSCH users' results. The reports are published annually under the label of *BENSCH EXPERIMENTAL REPORTS*, and the year 2004 volume, HMI-B 601, is distributed to all users of BENSCH in May 2005 as CD ROM and/or in printed form. The reports for 2000 through 2004 are also available on the BENSCH internet pages. (<http://www.hmi.de/bensch/user-info/reports.htm>)

This rapid distribution of results is complemented by oral and poster contributions to national and international conferences. Publication in internationally renowned peer reviewed journals normally follows the experiments with a delay of 1 to 2 years. Since as a rule at least one collaborating BENSCH scientist is among the authors the year 2002 publications of external users are included in the publication lists of the departments SF1, SF2 or SF3. A complete compilation of the year 2004 publication lists for all BENSCH users and BENSCH staff members is included in the a.m. volume *BENSCH EXPERIMENTAL REPORTS 2004*, HMI-B601, May 2005. The majority of the BENSCH publications have an external user as principal author, and a remarkably high fraction is published in high ranking journals.

The impact of BENSCH to the national neutron user community has been demonstrated at the *Deutsche Neutronenstreutagung 2004 Dresden, September 2004, 1.–4.* At this meeting, a third of all contributions reported on results of experiments at BENSCH: 34% of the talks, and 32% of the posters. The majority of these BENSCH contributions have been presented by external users. For three specific scientific fields, *Magnetism*, *Biological Systems*, and *Materials* the BENSCH partition scored the 50% level.

Four examples of highlight results from external user groups are included in the Scientific-Highlights Section of this Report.

NAA Laboratory and Irradiation Service at BER II

D. Alber, G. Bukalis, B. Stanik, A. Zimmer
 ■ HMI, SF6

The laboratory for neutron activation analysis (NAAL) at the BER II provides irradiation services for universities, scientific institutions and industry. Typical fields of applications are:

- Trace elements analysis by means of neutron activation analysis (NAA) for example in biology, medicine, geology and archeology. Certification of reference materials.
- Irradiation experiments, such as isotope production for medical applications, sources for Mößbauer spectroscopy and production of tracers for scientific and industrial applications.

The operation and further development of the irradiation devices at BER II and of the NAA measuring systems are a central task of the department SF6.

Irradiation devices

Four irradiation devices are available for different applications.

DBVK: irradiation device in the reactor core

DBVR: turnable irradiation device in the Be-reflector of the reactor core

TBR: dry irradiation device outside the Be-reflector

SRT: fast rabbit system

DBVK and DBVR are used for long term irradiation experiments. Up to nine aluminum containers can be irradiated simultaneously. Short time irradiation experiments are carried out by means of TBR and SRT.

Device	Φ_{thermal} [1/cm ² s]	Φ_{fast} [1/cm ² s]	Container
DBVK	1,5E+14	4,3E+13	6
DBVR	7,5E+12	1,9E+10	9
TBR	3,4E+12	2,2E+10	1
SRT	4,4E+11	3,9E+10	1

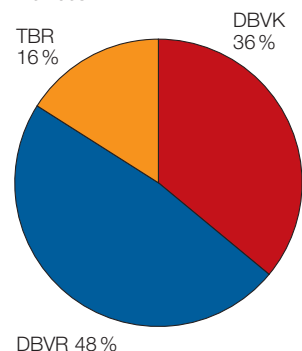
Status 2004

- Due to shortage in manpower, the project of the renewal of the SRT, the device for short time irradiation, has to be postponed.
- The upgrading of the DBVK, the in-core device, has been completed. Now irradiation of destructible materials is possible.
- New control units for DBVK and DBVR have been installed. The rotation of the carrier of the DBVR is now freely programmable, starting from one turn per second.

Irradiation experiments 2004

Since June 2004, irradiation of destructible material, particularly biological material in the DBVK has been possible. Consequently, the contribution of this device rose from 9 % in 2003 up to 35 %. During the shutdown of the BER II in the fourth quarter, we had the opportunity to irradiate some samples at the reactor of the GKSS in Geesthacht. Thanks to Mr. Pfaffenbach and Mr. Heuer.

Utilisation of the Irradiation Devices



A total of 3314 samples were irradiated in 2004. 81 % of the 265 irradiation experiments, were performed with the DBVK or DBVR. With these devices it is possible to irradiate up to 24 samples simultaneously in one aluminum container. About 40 % of the irradiation experiments and the analysis of samples done for external users.

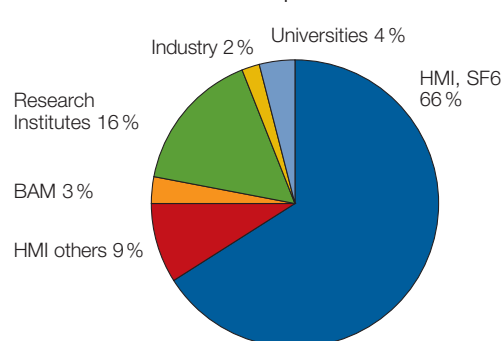
Internal users

Most of the internal users are from the Dept. SF6, but irradiation and analyses were also performed for users from other departments (SF2, SF3, SE2, SE5, RE).

External users

Irradiation experiments and NAA was performed for users from the German universities (Berlin, Gießen, Mainz, Heidelberg, Leipzig, Munich, Kiel) and from research institutes like BAM (Berlin), GSF (Neuherberg), IZW (Berlin), and the Rathgen Research Laboratory (Berlin).

Irradiated Samples



ISL Operations and Developments

Scientists: H. Homeyer, P. Arndt, W. Busse, A. Denker, C. Rethfeldt, J. Röhrich
 Operators: J. Bundesmann, R. Grünke, G. Heidenreich, H. Lucht, E. Seidel, H. Stapel

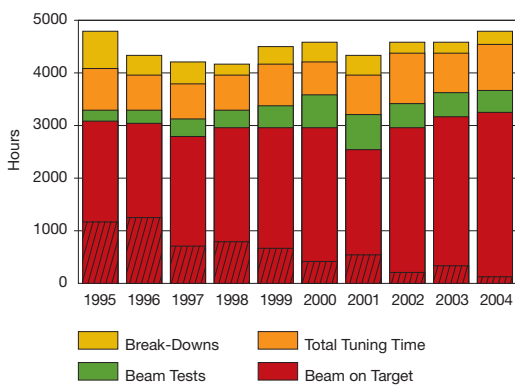


Fig. 1: ISL Operations since 1995: ISL has managed to operate the facility with an average of 3000 hours of beamtime on target. The hatched parts are low energy (Van-de-Graaff) beams. 2004 marks a new record: The highest amount of beam time on target, in particular high energy beams. This is due to the fact that the reliability for Au ion beams increased.

The Ion Beam Laboratory ISL offers ion beams from various accelerators and accelerator combinations with energies ranging from some tens of eV to several hundred MeV dedicated to the application of ion beam techniques. Internal and outside users study the basics of the interaction of ions with solids. They modify and analyse materials with ion beams and they perform radiotherapy of eye tumours with fast protons in a joint venture with university clinics. Users have at their disposal 15 different irradiation areas equipped with specific instrumentation.

ISL operations went rather smoothly in 2004 (see Fig. 1). At the beginning of the year, the only major breakdown was caused by insulation problems of the electrostatic injection element. For the repair, we had to open the extraction system. This gave us the rare occasion to have a look at the inner parts of the cyclotron as shown in Fig. 2.

The production of high energy beams within the scheduled operation time of nearly 4500 hours climbed to a new all-time high of 3200 hours. Two reasons contributed to this excellent outcome: I) improved operations of the ion source for Au-ion beams which was again the

most attractive beam used in 2004, II) a larger demand for high energy proton beams, providing an effective use of the time between the therapy sessions either for high-energy PIXE, radiation hardness testing or device testing for a large proton-therapy machine.



Fig. 2: A rare picture of the inner part of the cyclotron: The electrostatic inflector during the repair

49 different projects (41 in 2003) involving more than 100 scientists received beamtime in 2004. In total, more than 80 projects are active at ISL. At its annual meeting, the programme advisory committee accepted, on the basis of the proposals' scientific merit, 44 proposals: 20 new ones and 24 addenda to running experiments.

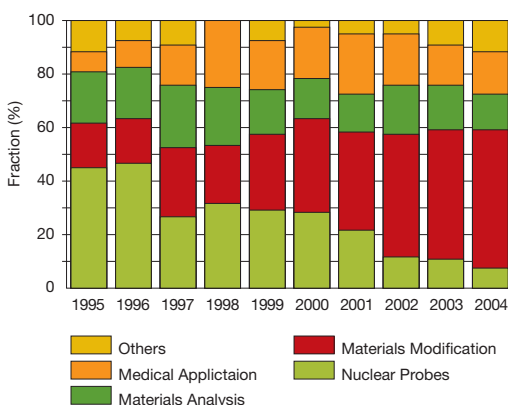


Fig. 3: Use of ISL ion beams. Materials modifications have become the largest part of research and development at ISL. The corresponding user groups come essentially from universities.

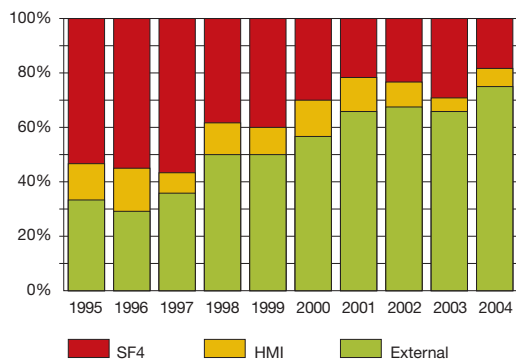


Fig. 4: ISL's development into a user facility. External users including proton therapy used 75% of the beam-time in 2004.

Materials analyses with an average of 15 % of the beam time have been performed exclusively with fast ions, either heavy ions for ERDA – predominantly to determine the stoichiometry of thin layers for the solar energy programme of the Hahn-Meitner-Institut – or protons for high-energy PIXE. Eye tumour therapy was performed at 10 therapy blocks for 100 patients. The total share of 17 % includes beam time for research work.

Beamtime used for materials modifications and ion-solid interactions is still rising. We expect this trend to continue as their share of applications for beam time at the programme advisory committee increased from 60 % to almost 80 %. The term *others* in Fig. 3 comprises radiation hardness tests as well as testing of a scanning system for a large proton therapy machine (see p. 20). The amount of beam time used by external users increased again to up to now 75 % of the total time as shown in Fig. 4.

The universities further increased their share, due to the on-going trend in the scientific programme towards ion beam modification of materials.

Though a lot of different ion species have been produced (see Fig. 6), for two thirds of the beam-time either lightest (protons) or the heaviest (Au) ions have been used. It is very clear that the intense Au-ion beam has pushed forward the materials-modification programme. Very important for this programme is an intermediate mass beam which could be supplied with a newly developed Cu-ion beam (120 MeV). Two more so-called cocktail beams, ions with the same charge/mass ratio and the same velocity, have been produced: 10 MeV/u Ne/Ar using the Van-de-Graaff as injector and 6 MeV/u O/Ar/Kr with the RFQ-injector. We assume an increasing

demand for these cocktail beams as they will allow rapid changes of the ion species and therefore the energy deposition.

Most of the development was dedicated to increasing the reliability of the facility in general. Quadrupole power supplies in the injection system were replaced. The target place TM was modified to host an industrial company for tests of parts of a proton therapy unit. The set-up of the new platform for the injection into the RFQ could be finished. When this platform is in operation, we expect a reduction of tuning times as the ECR ion-source can be tuned parallel to a running experiment. We expect the first beam from the second platform by the beginning of 2005.

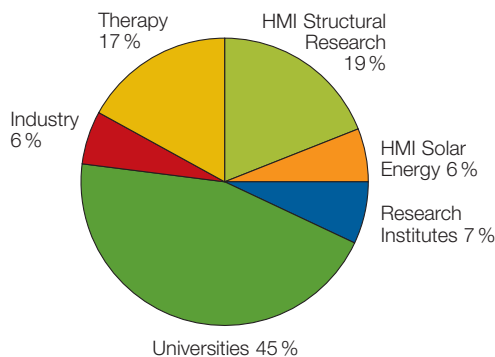


Fig. 5: Origin of ISL Users: The university share has again increased. This is due to their active involvement in the materials modification programme. The solar energy departments mainly use ERDA for the analysis of thin film solar cells.

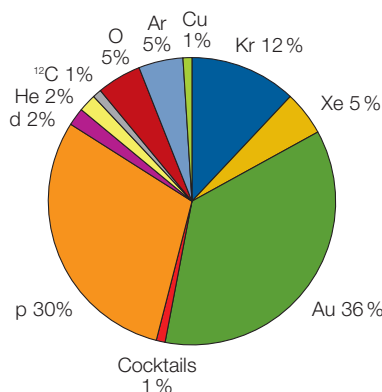


Fig. 6: Fast ion beams used at ISL: in 2004, most of the beam time used either the lightest or the heaviest ions available. In addition, so-called cocktail beams have been produced.



The cyclotron at the Ion Beam Laboratory ISL



Scientific highlights Structural Research 2004

BENSC User Service	36
ISL User Service	44
NAA User Service	48
SF1, Methods and Instruments	50
SF2, Magnetism	54
SF3, Materials	58
SF4, Structure and Dynamics	60
SF5, Theoretical Physics	66
SF6, Molecular Trace Element Research in the Life Sciences	70
SF7, Nuclear Measurements	72

Magnetisation plateaus in the quantum magnet NH_4CuCl_3

Ch. Rüegg^{1,2}, M. Oettli¹, J. Schefer¹, O. Zaharko¹, A. Furrer¹, H. Tanaka³, K.W. Krämer⁴, H.-U. Güdel⁴, P. Vorderwisch⁵, K. Habicht^{5,6}, T. Polinski⁵, M. Meissner⁶

■ 1 Laboratory for Neutron Scattering, ETH Zurich and Paul Scherrer Institute, Villigen PSI, Switzerland

■ 2 Department of Physics and Astronomy, University College London, UK ■ 3 Department of Physics, Tokyo

Institute of Technology, Japan ■ 4 Department of Chemistry and Biochemistry, University of Berne, Switzerland

■ 5 HMI, SF1 ■ 6 Institute of Solid State Physics, Technical University of Darmstadt, Germany

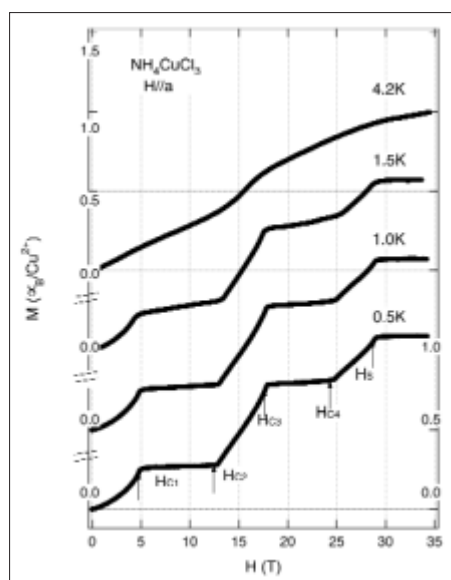


Fig. 1: Magnetisation curves of NH_4CuCl_3 measured at different temperatures with $H||a$, from Ref. [5]

The response of quantum spin systems to an external magnetic field has recently attracted the interest of experimental and theoretical physicists due to the possibility to investigate the influence of quantum effects on the macroscopic properties of a solid, e.g. its ground state and magnetisation curve [1]. The former is frequently observed to be a nonmagnetic singlet state for dimer based compounds like $\text{SrCu}_2(\text{BO}_3)_2$ and TlCuCl_3 , where two Cu^{2+} ions with an $S=1/2$ magnetic moment are coupled by a dominant antiferromagnetic exchange interaction. The resulting singlet state on each dimer is hereby protected by a spin energy gap from the magnetic triplet states as the elementary excitations. An external magnetic field can induce a quantum phase transition at the critical value H_c , where the onset of long-range magnetic order is observed [2, 3]. A related transition occurs also as a function of hydrostatic pressure [4]. However, the details of the uniform magnetisation are fundamentally different for $\text{SrCu}_2(\text{BO}_3)_2$ and TlCuCl_3 [1, 2]. The former shows distinct plateaus in this quantity at fractional values of the magnetic saturation ($m=1$) whereas the latter demonstrates the case of a uniform increase above H_c ($m=0$).

The ammonium substituted compound NH_4CuCl_3 was believed to be isostructural to TlCuCl_3 and therefore to show similar magnetic

properties. It therefore came as a surprise that the uniform magnetisation in NH_4CuCl_3 is characterised by magnetisation plateaus at $m=1/4$ and $m=3/4$, but on the other hand none at $m=0$, corresponding to a spin gap at $H < H_c$, see Fig. 1 [5]. The mystery in NH_4CuCl_3 and the mechanism leading to the plateau formation in general have consequentially been addressed by complementary experimental techniques including specific heat, NMR, and neutron scattering. The first plateau can fortunately be reached by the high-field equipment for neutron scattering at the Hahn-Meitner-Institut.

The investigations reveal the presence of several structural phase transitions leading to the space group P-1 at low temperatures with a doubling of the unit cell along the b -axis. The reduced symmetry in combination with the doubling of the unit cell defines three inequivalent dimer subsystems with volume fractions 25%, 50%, and 25%, see Fig.2 [6]. The segregation into different dimer subsystems is further reflected in the excitation spectrum measured by INS, which clearly identifies three modes in well-separated energy ranges, see

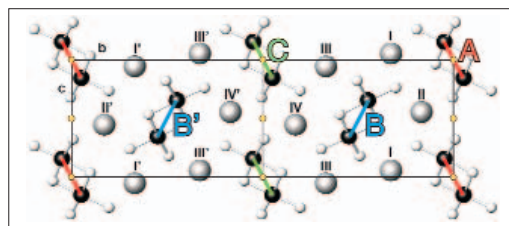


Fig. 2: Low-temperature structure of NH_4CuCl_3 in projection along the a -axis on the bc -plane. The high-temperature unit cell is doubled along the b -axis. Subsystems of Cu^{2+} dimers are marked by A, B, B' and C, inequivalent NH_4^+ groups by Roman numbers I-IV and I'-IV'. Orange circles denote inversion centres in case of space group P-1 where the primed sites become equivalent to the unprimed ones.

Fig.3 [6]. The absence of the $m=0$ plateau is explained by the gapless ground state resulting from the onset of long-range order, which is directly detected by antiferromagnetic Bragg peaks raising below $T=1.3\text{K}$ already in zero-field. The phase boundary has additionally been scanned by specific heat measurements performed at the Hahn-Meitner-Institut down to $T=0.3\text{K}$ and up to $H=6\text{T}$. The field dependence of the excitation spectrum as measured by INS identifies successive quantum phase transitions of the dimer subsystems as the driving mechanism for the unconventional magnetisation process, in complete agreement with theoretical predictions [6, 7].

In NH_4CuCl_3 the first plateau sets in, when the subsystem A is completely polarised along the field direction. Accordingly the second plateau starts, when also the subsystem B reaches its complete saturation. The magnetisation rises at the edge of the first (second) plateau, when the individual spin gap of the dimer subsystem B (C) is closed and field-induced magnetic order occurs, similar to the soft-mode transition reported for TiCuCl_3 , see Fig.3 [3, 6, 7]. The energy splittings observed at $T=0.13\text{K}$ and $T=1.8\text{K}$ are identical, i.e. they are not affected by the onset of magnetic order. This directly proves that 75% (B and C) of the spin system remain in a gapped singlet state whereas 25% (A) order. The mode linearly increasing above H_{c1} is further interpreted as the field-induced opening of a spin gap for the subsystem A. This gap can be understood as the linear increase of the Zeeman energy for a triplet-singlet transition.

The investigation of quantum phase transitions in dimer spin systems demonstrates that especially the excitations characterise a ground state or its evolution as a function of an external parameter. The detection of long-range order is in the present context not conclusive in terms of a detailed statement about the ground-state wave function. To measure the excitation spectrum, in this case by INS, is therefore essential for a successful characterisation of the above transitions. The detected singlet-triplet condensate ground states in TiCuCl_3 and NH_4CuCl_3 are summarised in Fig. 4.

Triplet states are admixed to the singlet condensate in TiCuCl_3 above H_c . This occurs in a *homogeneous* way, i.e. each dimer site is involved due to the mobility of the triplet quasi-particles. In NH_4CuCl_3 the situation is more complex because of the three dimer subsystems, which are intimately related to the plateau formation. At $H_{c1} < H < H_{c2}$ inside the $m=1/4$ plateau, 25% of the dimers are in a field-aligned triplet state, whereas

75% are gapped. The singlet-triplet spin gap for the subsystem with 50% volume fraction is closed at H_{c2} . Accordingly, for $H_{c2} < H < H_{c3}$ triplet states are admixed on these dimers. The condensate in NH_4CuCl_3 is in this sense *inhomogeneous*. The generic case, found in $\text{SrCu}_2(\text{BO}_3)_2$, where the condensate is inhomogeneous without an explicit breaking of translational symmetry by a structural phase transition, could still occur in this field range in the layers of this 50%-subsystem. This possibility is not considered in Fig. 4 and was so far not observed experimentally.

The presented results about the field-induced phases in dimer spin systems are not limited to the investigated compounds. They are also valid for other dimer-based systems. The corresponding experiments on related materials have recently been performed or are planned for the near future.

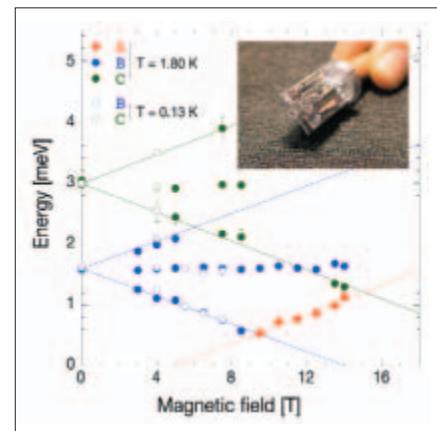


Fig. 3: Field dependence of the spin dynamics in NH_4CuCl_3 measured at $Q=(0\ 0\ 1)$, $T=1.8\text{K}$ and $T=0.13\text{K}$. Inset: Six coaligned NH_4CuCl_3 single crystals on an Al sample holder. The individual crystals are wrapped into Al foil and glued at the top and bottom onto adjustable Al plates. The arrangement fits into Hahn-Meitner-Institut's 15-T cryomagnet for neutron scattering experiments.

- [1] T.M. Rice, *Science* **298**, 760 (2002)
- [2] K. Kodama *et al.*, *Science* **298**, 395 (2002)
- [3] Ch. Rüegg *et al.*, *Nature* **423**, 62 (2003)
- [4] Ch. Rüegg *et al.*, *Phys. Rev. Lett.* **93**, 257201 (2004)
- [5] W. Shiramura *et al.*, *J. Phys. Soc. Jpn.* **67**, 1548 (1998)
- [6] Ch. Rüegg *et al.*, *Phys. Rev. Lett.* **93**, 037207 (2004)
- [7] M. Matsumoto *et al.*, *Phys. Rev. B* **68**, 180403 (2003)

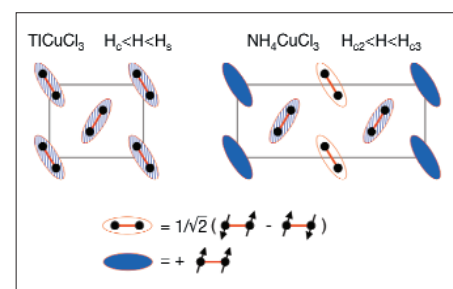


Fig. 4: Schematic representation of singlet-triplet condensates. Projection of a single unit cell along the a -axis on the bc -plane. Left: TiCuCl_3 above the critical field H_c but below saturation H_s . Right: NH_4CuCl_3 between the $m=1/4$ and $m=3/4$ plateau. 25% of the dimers are in the triplet state (field-aligned, dark blue). Light blue denotes triplet admixture.

Corresponding author:

C. Rüegg
c.ruegg@ucl.ac.uk

Does antiferromagnetism survive in the superconducting phase of CeCu_2Si_2 ?

O. Stockert¹, E. Faulhaber², K. Prokeš³, N. Stüßer³, S. Gerischer⁴, P. Smeibidl³, H.S. Jeevan¹, M. Deppe¹, C. Geibel¹, M. Loewenhaupt², F. Steglich¹

■ 1 Max-Planck-Institut für Chem. Physik fester Stoffe, Dresden, Germany ■ 2 Institut für Festkörperphysik, TU Dresden, Germany ■ 3 HMI, SF2 ■ 4 HMI, SF1

The interplay of superconductivity and antiferromagnetic order continues to be of general interest in condensed matter physics. While the coexistence of antiferromagnetism and superconductivity can easily be understood if different electronic subsystems are involved in the two phenomena, the situation might be different if the same electron system is responsible for both. In the case of the heavy-fermion compound CeCu_2Si_2 the Ce-4f electrons do not only order magnetically but are also involved in the formation of superconducting Cooper pairs. The strong electron correlations in CeCu_2Si_2 show up e. g. in a huge linear coefficient to the electronic specific heat at low temperatures, $\gamma = C/T \approx 1 \text{ J/molK}^2$, indicative of a largely enhanced effective electron mass. In consequence, such systems are called heavy-fermion systems [1].

growing technique improved quite a lot, now allowing to grow large single crystals with well defined properties. Recently, we could identify the antiferromagnetic order on a large A-phase single crystal by neutron diffraction [3]. Below $T_N \approx 800 \text{ mK}$ antiferromagnetic superstructure peaks have been detected and the ordered moment is estimated to $< 0.1 \mu_B$. The propagation vector τ of the magnetic A-phase order, $\tau = (0.215 \ 0.215 \ 0.530)$ at $T = 50 \text{ mK}$, appears to be determined by the nesting properties of the Fermi surface as indicated by renormalized band-structure calculations.

With the knowledge of the A-phase magnetism we started our investigation of the interplay between antiferromagnetism and superconductivity on an A/S single crystal with a $T_N \approx 700 \text{ mK}$ and a superconducting $T_c \approx 500 \text{ mK}$. We performed neutron diffraction experiments on the diffractometers E4 and E6 at temperatures below $T = 1 \text{ K}$ and in magnetic fields up to $B = 2 \text{ T}$. In order to address the question about the possible coexistence of superconductivity and magnetic order, it is of high importance to measure both phenomena simultaneously. Since neutrons are sensitive to antiferromagnetic order, but cannot directly probe superconductivity, we designed a setup to measure the bulk ac susceptibility in situ, i.e. during the neutron diffraction experiment. A small ac magnetic field is applied to the sample by an excitation coil and the susceptibility signal is measured by a pair of pickup coils. Excitation and pickup coils are made out of copper wire wound on a thin copper coil former to minimize absorption. The whole setup is displayed in Fig. 1a. The sensitivity to detect the superconducting transition is verified in temperature and field sweeps (cf. Figs. 1b and 3a).

Rocking scans across the positions of magnetic superstructure peaks were performed at different points in the magnetic (B, T) phase diagram as shown in Fig. 2a. Here, the (B, T) phase diagram is known from thermodynamic and transport measurements. We focused our study

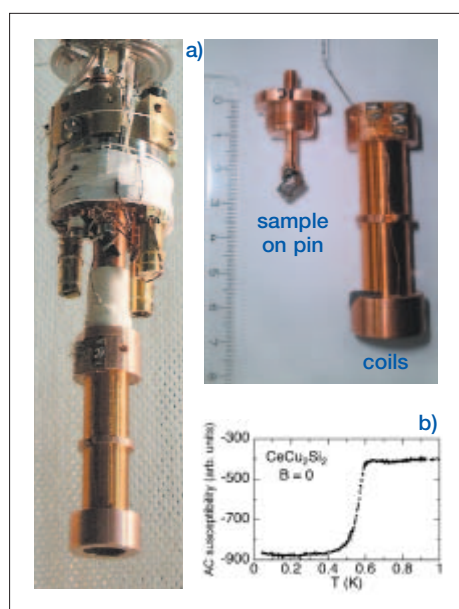


Fig. 1: a) Setup to measure the ac susceptibility on the neutron diffractometer. b) Temperature dependence of the ac susceptibility in CeCu_2Si_2 showing the onset of superconductivity at $T \approx 500 \text{ mK}$

The heavy-fermion compound CeCu_2Si_2 forms only in a very narrow range of the ternary phase diagram Ce:Cu:Si around the 1:2:2 composition. However, the ground state in CeCu_2Si_2 depends very delicately on the actual composition. Thus, Cu-rich samples exhibit only superconductivity and Si-rich only show a magnetically ordered phase called A-phase, while in stoichiometric samples (A/S-type) a complex interaction between superconductivity and magnetic order occurs [2]. During the last few years the crystal

to low temperatures and low magnetic fields in order to investigate the interplay between magnetic order and superconductivity. Our main results are displayed in Fig. 2b. In zero magnetic field just below the Neel temperature the magnetic Bragg peak is observed, but has disappeared at $T=400$ mK, i.e. well inside the superconducting phase. Applying at $T=400$ mK an overcritical magnetic field of $B=2$ T to kill superconductivity, leads to a recovery of the antiferromagnetic order. The absence of magnetic Bragg peaks in the superconducting phase gives evidence that in this crystal antiferromagnetism and superconductivity seem to exclude each other on a microscopic scale. These findings are in line with results obtained by μ SR and NMR measurements [4, 5]. A great advantage of the in situ susceptibility measurement is the possibility to perform measurements close to the phase boundaries. In particular, we investigated the transition from superconductivity to the A-phase at lowest temperature $T=50$ mK. From the bulk susceptibility the transition is at $B \approx 1.1$ T. Away from the phase boundary the results are as expected, i.e. no antiferromagnetic order in zero field and the recovery of antiferromagnetism at $B=2$ T. Surprisingly, at 1 T where the susceptibility indicates that the crystal is still superconducting, the magnetic Bragg peak is observed. We attribute this to the first-order nature of the phase boundary between superconductivity and antiferromagnetism which seems to be accompanied by phase separation. Experiments to clarify the situation in the vicinity of the phase boundaries will be continued in the near future.

In conclusion, we performed neutron diffraction with a newly developed in situ ac susceptibility setup and investigated an A/S-type CeCu_2Si_2 single crystal. Our measurements give evidence that superconductivity expels antiferromagnetism at low temperatures and that both phenomena do not coexist on a microscopic scale.

We greatly acknowledge the help of the whole sample environment team at BENSC. Without them, the experiment would not have been possible. Our work is supported by the Deutsche Forschungsgemeinschaft within Sonderforschungsbereich 463.

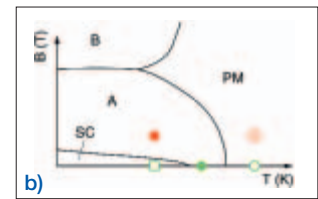
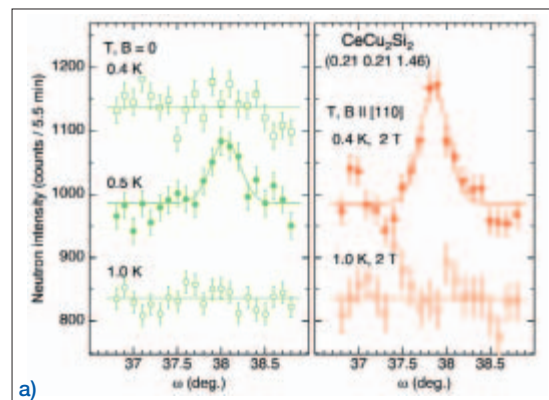


Fig. 2: **a)** Schematic magnetic (B, T) phase diagram of CeCu_2Si_2 with different magnetically ordered phases (A-, B-phase) and the superconducting phase.

The (B, T) values at which neutron diffraction measurements were performed, are marked. **b)** Rocking scans across the position of a magnetic superstructure peak in CeCu_2Si_2 at different temperatures and magnetic fields. While magnetic superstructure peaks are present in the A-phase, no magnetic peak has been detected in the superconducting phase. This indicates that superconductivity and antiferromagnetism exclude each other on a microscopic scale.

- [1] An introduction to heavy-fermion physics can be found e.g. in: N. Grewe, F. Steglich, *Handbook on the Physics and Chemistry of Rare Earths* (Elsevier Science Publishers B.V., Amsterdam, 1991), vol. 14, chap. *Heavy Fermions*, p. 343
- [2] F. Steglich *et al.*, *More is different – fifty years of condensed matter physics* (Princeton University Press, 2001), chap. 13, p. 191
- [3] O. Stockert *et al.*, Phys. Rev. Lett. **92**, 136401 (2004)
- [4] R. Feyerherm *et al.*, Phys. Rev. B **56**, 699 (1997)
- [5] K. Ishida *et al.*, Phys. Rev. Lett. **82**, 5353 (1999)

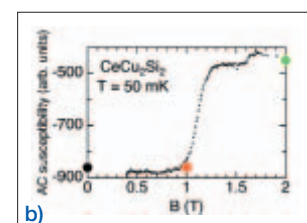
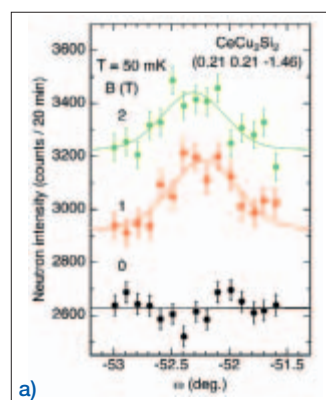


Fig. 3: **a)** Magnetic field dependence of the ac susceptibility at $T=50$ mK indicating the transition from superconductivity to the A-phase at $B \approx 1.1$ T.

b) Rocking scans as in Fig. 2 **b)** at $T=50$ mK for different magnetic fields (marked in **a)**). The existence of magnetic intensity at $B=1$ T points to a phase separation at the transition between A-phase and superconducting phase.

Corresponding author:
O. Stockert
stockert@cpfs.mpg.de

Tailoring surface coatings for protein immobilization

C. Czeslik¹, G. Jackler¹, R. Steitz²

■ 1 Universität Dortmund, Physikalische Chemie I, Dortmund, Germany ■ 2 HMI, SF1

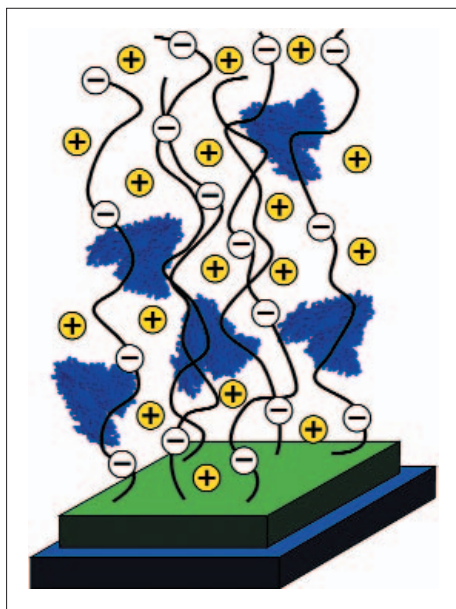


Fig. 1: Schematic drawing of a poly(acrylic acid) brush anchored on a thin poly(styrene) film that is deposited on a silicon wafer. The brush is characterized by a high concentration of trapped counterions. It can bind various amounts of protein depending on the ionic strength of the protein solution.

To vary the degree of protein adsorption at an interface, one may vary the pH-value or the ionic strength of the protein solution, in order to modify or shield the electric charge of the protein molecules and thus the electrostatic protein/interface interactions. However, a general variation of the degree of protein adsorption is principally not possible in this way. Thus, one has to develop functional surface coatings with a variable and controllable protein affinity.

As observed in numerous experimental studies, proteins adsorb spontaneously at almost all aqueous/solid interfaces [1, 2]. This phenomenon is also encountered in daily life, such as the adsorption of lysozyme onto contact lenses or the attachment of marine organism at ships using protein-based adhesives. There are also practical applications in which adsorbed proteins play a key role. For example, solid-phase immunoassays are used in medical diagnostics, such as pregnancy tests, where adsorbed protein antibodies bind antigens specifically.

In recent studies, the protein binding capacity of colloidal particles that are covered with a poly(acrylic acid) (PAA) brush has been determined [3, 4]. It has been found that these PAA brush particles bind huge amounts of proteins at low ionic strength and neutral pH-values where the PAA is dissociated and negatively charged. Interestingly, when the ionic strength of the solution is increased to a few 100 mmol/L, the PAA brush particles appear essentially protein resistant regardless of the protein net charge. Thus, by varying the ionic strength of the solution over a relatively small range, the protein affinity of the PAA brush particles can be switched between high and low. It is noted that this effect is not related to a simple electrostatic screening, since the effect has also been observed for the protein BSA that binds to the PAA brush particles under electrostatic repulsion.

Using neutron reflectometry the protein binding capacity of a planar PAA brush has been studied for the first time (Fig. 1) [5]. The planar PAA brush has been prepared by spin-coating a thin poly(styrene) film onto a silicon wafer. Then, the diblock copolymer poly(styrene)-poly(acrylic acid) was transferred to the modified Si wafer applying the Langmuir-Schäfer technique.

In Fig. 2, selected neutron reflectivity curves are shown which were obtained when the planar PAA brush was in contact with a pure buffer solution, a buffer solution containing BSA, and a buffer solution containing BSA and 500 mmol/L sodium chloride. From a simple visual inspection of the three curves, one may conclude that in the presence of sodium chloride the planar PAA brush appears to be protein resistant, since the corresponding reflectivity curve essentially overlaps with that of the pure buffer solution. This overlap indicates an unchanged interfacial structure. In contrast, without added salt, BSA binds to the planar PAA brush under electrostatic repulsion, since the reflectivity curve of the pure buffer solution is changing significantly upon adding BSA to the solution. Thus, a functional surface coating has been generated which can be used to switch the protein affinity of an interface.

A detailed analysis of all the measured neutron reflectivity curves indicates that BSA is penetrating deeply into the planar PAA during adsorption at low ionic strength (Fig. 3). Since BSA and PAA are like-charged and no adsorption takes place at elevated ionic strength, BSA must be immobilized at the planar PAA brush by a driving force different from ionic, van der Waals and hydrophobic interactions.

Indeed, a simple mean field model has been developed that predicts a large gain of free energy due to a release of BSA counterions on transferring a BSA molecule from the solution into a PAA brush [5]. The free energy of this counterion *evaporation* is entropic in nature and dominates over the direct electrostatic repulsion between the protein and the like-charged brush. The reason for this loss of ions is the enormous excess of positively charged counterions in the PAA brush requiring a lower number of BSA counterions only. As the ionic strength of the protein solution is raised, this counterion release force is vanishing rendering a PAA brush protein resistant.

The experimental and theoretical results of this study therefore suggest a new fundamental driving force for protein adsorption at interfaces. Since a change of the ionic strength over a few 100 mmol/L mainly leaves the structure and dynamics of dissolved protein molecules unaffected, the switching of the protein affinity of a PAA brush by changing the ionic strength of the protein solution is likely to be protein independent, and its use in biotechnological applications appears to be rewarding.

-
- [1] M. Malmsten (ed.), *Biopolymers at interfaces*, Marcel Dekker, New York (2003)
 [2] C. Czeslik, *Z. Phys. Chem.* **218**, 771 (2004)
 [3] A. Wittemann, B. Haupt, M. Ballauff, *Phys. Chem. Chem. Phys.* **5**, 1671 (2003)
 [4] C. Czeslik, R. Jansen, M. Ballauff, A. Wittemann, C.A. Royer, E. Gratton, T. Hazlett, *Phys. Rev. E* **69**, 021401 (2004)
 [5] C. Czeslik, G. Jackler, R. Steitz, H.-H. von Grünberg, *J. Phys. Chem. B* **108**, 13395 (2004)

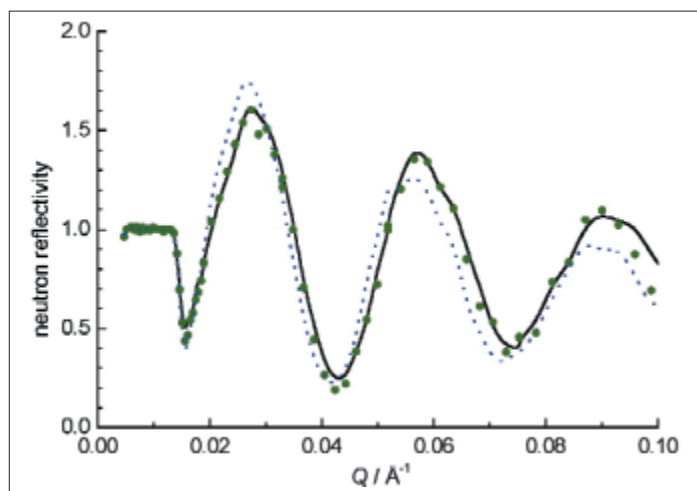


Fig. 2: Neutron reflectivity curves of a silicon/solution interface that has been modified with a planar PAA brush (see Fig. 1). The curves are normalized to that of a smooth Si/water interface. Data are shown for a pure buffer solution (black solid line), a buffer solution containing the protein BSA and NaCl (green symbols), and a buffer solution containing BSA without NaCl (blue dotted line). The data indicate BSA binding to the PAA brush in the absence of NaCl only which can be explained by a release of counterions.

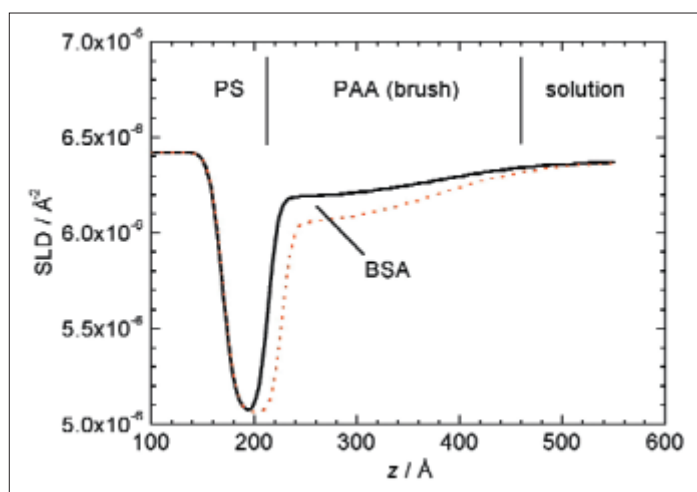


Fig. 3: Scattering length density (SLD) profile of a planar PAA brush (see Fig. 1) with and without immobilized protein (BSA). The difference between the two profiles is proportional to the protein volume fraction.

Corresponding author:

C. Czeslik
 claus.czeslik@uni-dortmund.de

Structural explanation of the magneto-electric phase transitions in HoMnO_3

Th. Lonkai^{1,2}, U. Amann^{1,3}, J. Ihringer¹, D. Hohlwein^{1,2}, Th. Lottermoser⁴, M. Fiebig⁴

■ 1 Institut für Angewandte Physik, Universität Tübingen, Germany ■ 2 HMI, SF2 ■ 3 Institut Laue-Langevin, Grenoble, France ■ 4 Max-Born-Institut, Berlin, Germany

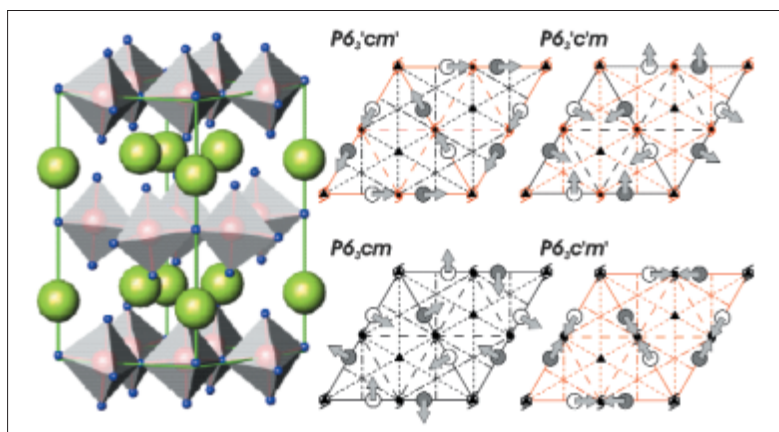


Fig. 1: Nuclear and magnetic structure of HoMnO_3 . The hexagonal manganite HoMnO_3 is formed of planes of corner connected tilted and distorted MnO_5 -coordination polyhedra, separated by corrugated R -planes, Mn red, O blue, Ho green. The magnetic space groups are depicted on the right light (dark) spheres are Mn atoms with $c=0$ ($c=1/2$).

As the data density in conventional information storage reaches its physical limits, alternative concepts are analysed. The linear magneto-electric effect, i.e. the induction of a magnetic polarization due to an electric field and vice versa, provides a possibility to manipulate magnetic data by other means than magnetic fields. In HoMnO_3 single crystals with electric field of $E \sim 10^5 \text{ V/cm}$, we evidenced the control of the magnetic ordering by magneto-optical methods, the magnetic ordering is switched from antiferromagnetic to ferromagnetic. By neutron and x-ray powder diffraction, we derived an explanation of the magneto-electric phase transitions.

In zero field hexagonal HoMnO_3 traverses the magnetic phases $P6_3c'm$, $P6_3c'm'$, and $P6_3cm$, the phase transitions are at $T_N \sim 70 \text{ K}$, $T_R \sim 40 \text{ K}$, and

$T_{\text{Ho}} \sim 5 \text{ K}$, respectively [1, 2]. With an electric field of 10^5 V/cm , a different magnetic space group, $P6_3c'm'$ is formed below Néel-temperature (see Fig. 1). This was evidenced by magneto-optical methods (second harmonic generation and Faraday rotation [3].)

For a deeper understanding of this dramatic change in the magnetic structure of HoMnO_3 due to electric fields, a detailed understanding of the structure is essential. The electric ordering process was explained recently by group-theoretical methods and confirmed by neutron and x-ray powder diffraction. Hexagonal manganites traverse through two structural phase transitions at $T_{\text{npt}} \sim 1300 \text{ K}$ and $T_{\text{FE}} \sim 1000 \text{ K}$, from the paraelectric high temperature phase $P6_3/mmc$ to the ferroelectric low temperature phase, Fig. 2. In the high temperature phase, $T > T_{\text{npt}}$, the MnO_5 coordination polyhedra are undistorted with an O-Mn-O axis parallel c , while the R -planes, separating the planes of the

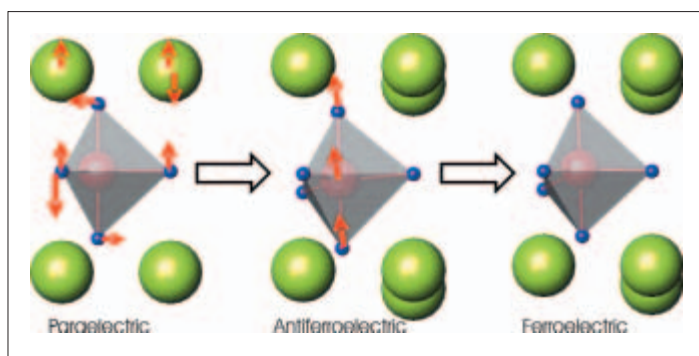


Fig. 2: Electric ordering process in HoMnO_3 in detail. In the paraelectric high temperature phase of the symmetry $P6_3/mmc$ the coordination polyhedra are straight and undistorted. In a first phase transition at $T_{\text{npt}} \sim 1300 \text{ K}$, the coordination polyhedra tilt and are distorted, while the Ho-planes become corrugated. The space group $P6_3cm$ is formed and an antiferroelectric phase is generated. Finally, at $T \sim 1000 \text{ K}$, a displacement of the O-Mn-O axis within the MnO_5 coordination polyhedra triggers a second phase transition, without a further change of symmetry, the ferroelectric low temperature phase is formed.

corner connected MnO_5 are flat – the structure is paraelectric. In a first phase transition at $T=T_{\text{npt}}$ the coordination polyhedra tilt and the R -planes become corrugated. Though the structure obeys the ferroelectric space group $P6_3cm$, it is still antiferromagnetic, until, in a second phase transition at $T=T_{\text{FE}}$ the O-Mn-O axis within the coordination polyhedra is displaced and a spontaneous electric polarization appears [4].

With a careful analysis of the results of Rietveld refinements of neutron and x-ray powder data (E2 [5], Hahn-Meitner-Institut, Berlin and high resolving Guinier diffractometer [6] with image plate [7], Tübingen [5]) of HoMnO_3 -powdered samples the magnetoelectric phase transitions can be explained. At lower temperatures, $T < T_{\text{Ho}} \sim 5$ K, the onset of Ho-ordering induces a magnetic phase transition from $P6_3c'm'$ to $P6_3cm$, and by this, a displacement of the O-Mn-O axis. Thus, the inter-planar magnetic exchange paths are changed, and by this, the electric polarization of the unit cell, Fig. 3. At higher temperatures with applied electric field, an equivalent process is induced. The electric field displaces the O-Mn-O axis of the MnO_5 coordination polyhedra, thus the magnetic exchange paths are changed and for the inter-planar coupling, a δ_3 -axis instead of a δ_3' -axis becomes favourable. The ferromagnetic space group, $P6_3c'm'$, which is formed now, requires a ferromagnetic ordering of the Ho moments parallel c , Fig. 4. In this space group, the magnetoelectric term lowers the overall energy of the system.

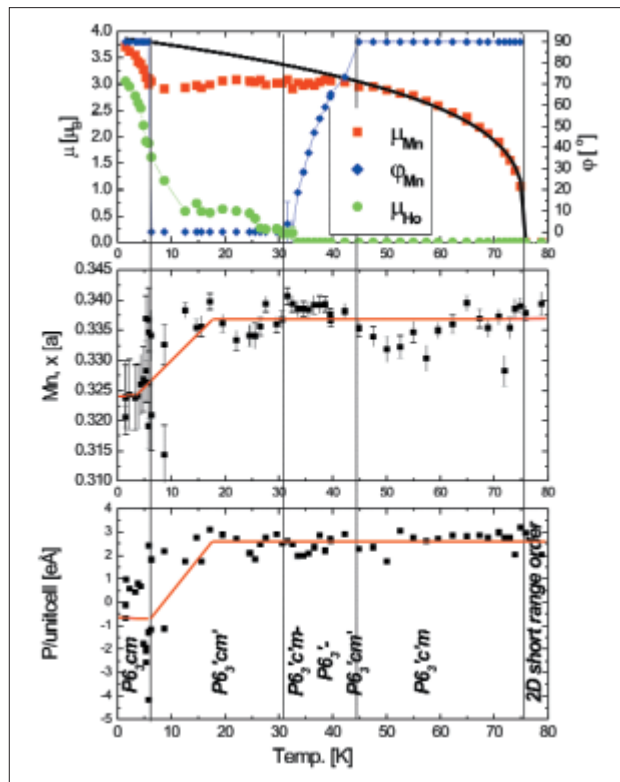


Fig. 3: Intra planar antiferromagnetic Ho ordering contradicts the symmetry $P6_3c'm'$, a new symmetry $P6_3cm$ is formed. The different coupling between the planes, δ_3 -axis instead of δ_3' -axis, requires different magnetic exchange paths, this leads to a change in the electric polarization: The O-Mn-O axis of the coordination polyhedra is shifted.

- [1] Th. Lonkai, D. Hohlwein, J. Ihringer, W. Prandl, Appl. Phys. A **74**, S843–S845 (2002)
- [2] M. Fiebig, C. Degenhardt, R.V. Pisarev, J. Appl. Phys. **91**(10), 8867–8869 (2002)
- [3] Th. Lottermoser, Th. Lonkai, U. Amann, D. Hohlwein, J. Ihringer, M. Fiebig, Nature **430**, 541–544 (2004)
- [4] Th. Lonkai, D.G. Tomuta, U. Amann, J. Ihringer, D. Toebbens, R. Hendriks, J. Mydosh, Phys. Rev. B **69**, 134108 (2004)
- [5] <http://www.hmi.de/bensc/misc/flat-cone/index.html>
- [6] <http://www.uni-tuebingen.de/uni/pki/guinier/guinier.html>
- [7] <http://www.uni-tuebingen.de/uni/pki/guinier/bildplatte.html>

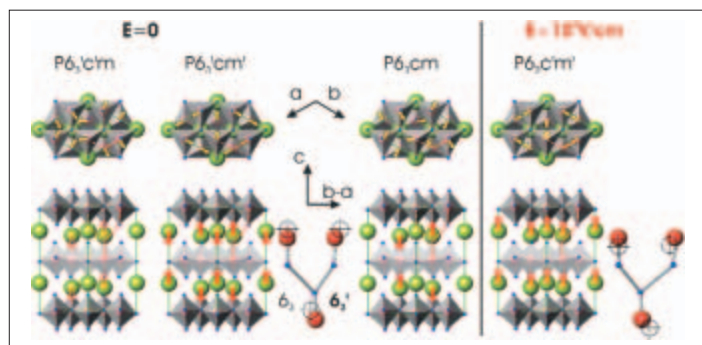


Fig. 4: The influence of the displacement of the O-Mn-O axis to the inter-planar magnetic exchange paths and structural explanation of the magnetoelectric phase transitions in HoMnO_3 . Due to the displacement of the O-Mn-O axis within the MnO_5 coordination polyhedra in an applied electric field, the inter-planar magnetic exchange paths are changed. A δ_3 -axis as inter-planar coupling becomes more favourable than a δ_3' -axis. The magnetic symmetry $P6_3c'm'$ is formed, which allows a magnetoelectric term, that leads to a lowering of the overall energy of the system.

Corresponding author:

T. Lonkai
thomas@lonkaimayer.de

Nanoscale self-assembly of thin oxide films under swift heavy ion bombardment

W. Bolse, A. Feyh, D. Etissa-Debissa, M. Kalafat

■ Institut für Strahlenphysik, Universität Stuttgart, Germany

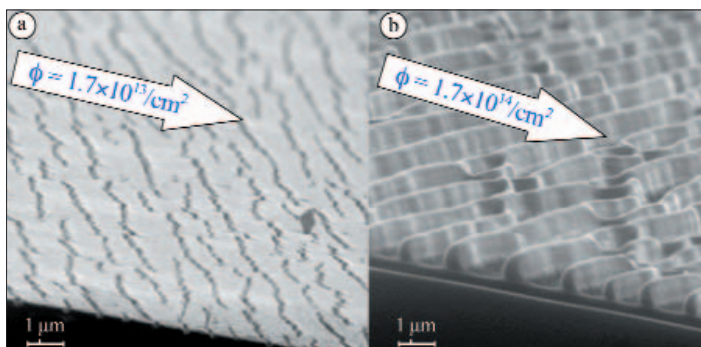


Fig. 1: Development of a 130 nm NiO/SiO₂ film during irradiation with 230 MeV Xe at a tilt angle of 75°. The arrows indicate the projection of the beam direction onto the sample surface.

During the last years, beams of swift heavy ions (SHI) of some MeV/amu have established themselves as excellent tools for nano-structuring of thin films and surfaces. A heavy ion of this kind deposits a huge amount of its kinetic energy almost instantaneously into a highly localized volume of nm-dimensions (at least laterally). The average energy deposited per atom may significantly exceed the binding energy of the solid and thus result in a nano-scale zone of extreme conditions (high temperature and pressure). The energy dissipation into the cold surrounding occurs within some tens of picoseconds and leads to rapid solidification of the excited track. This highly localized process (in space and in time)

can be regarded as a transient melting and rapid quenching mechanism, which drives the solid far from equilibrium and often leaves behind a nm-wide track of non-equilibrium material (for example the often observed amorphous tracks in insulators). Such extremely short and intense solid

state excitations, localized in a nano-scale volume, cannot be achieved by any other technique for material modification, and hence, single energetic ions offer a unique method to generate non-equilibrium phases with novel structural and physical properties and nm-dimensions. However, in recent years (and especially due to the intense and stable high energy ion beam provided by Hahn-Meitner-Institut's Ion Beam Laboratory – the Ionenstrahllabor ISL) it was discovered that not only single ion impact can be used to generate spatially separated nanoscale structures, but in many cases the application of high ion fluences may result in structural instabilities and a corresponding, often periodic, nanoscale patterning of surfaces and thin films. The properties of such self-organized structures usually surpass by far a simple superposition of the single-ion effects.

We have recently investigated the nano-scale self-assembly of thin Nickel-Oxide films triggered by SHI irradiation under inclined ion incidence [1–4]. Fig. 1 shows the scanning electron microscopy (SEM) images of a 130 nm thick NiO film on SiO₂ after irradiation with 230 MeV Xe-ions at fluences of $1.7 \times 10^{13}/\text{cm}^2$ and $1.7 \times 10^{14}/\text{cm}^2$. The sample was tilted by 75° with respect to the beam direction and kept at a temperature of 80 K. The arrows indicate the projection of the beam direction onto the surface. At low fluences, the surfaces exhibit an almost periodic crack pattern with typical distances of the order of 1 μm and oriented perpendicular to the beam direction. According to Trinkaus [5], the transient melting in the ion track generates tensile stresses along the track axis, which at grazing ion incidence results in an almost uni-axial in-plane stress field along the beam direction. As soon as these stresses exceed the critical fracture stress of NiO, the film becomes unstable (Grinfeld-instability [6]) and a periodic crack pattern forms. Further irradiation then results in shrinking of the material between the cracks and a growth in height due to the *hammering effect* [7]. Finally, a periodic lamellae-like structure is formed. The average height and distance of the *nano-walls* is of the order of 1 μm and their thickness is about 100 nm. These quantities strongly depend on the

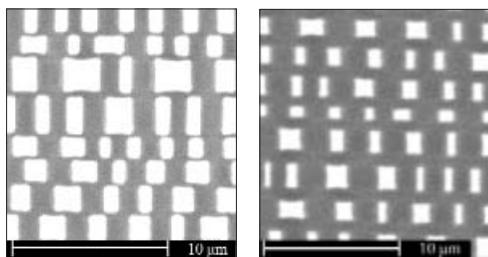


Fig. 2: a) 60 nm NiO/SiO₂ after double irradiation with 230 MeV Xe-ions (90° azimuthal rotation, $10^{14}/\text{cm}^2$ each direction, tilt angle 85°) b) same sample after additional irradiation under continuous azimuthal rotation (230 MeV Xe, 85°, $3 \times 10^{14}/\text{cm}^2$)

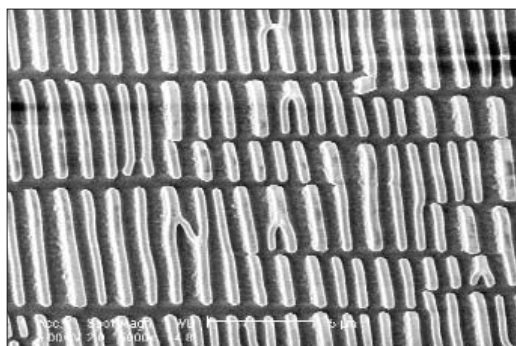


Fig. 3: Combination of Ar- and Au-irradiation, 90 nm NiO/SiO₂: stick-like structure

electronic stopping power of the ion and the initial film thickness, which on the other hand can be used to custom tailor the structural parameters. The disorder of the structure (cross-links between the lamellae) increases with increasing ion mass and decreases with increasing tilt angle and NiO thickness. Electron- and ion-microbeam analysis revealed that the initially coherent and smooth NiO-layer has quantitatively transformed into the lamellae-structure. No NiO is left on the substrate surface in between the walls.

Our knowledge of this self-assembly process, its underlying mechanisms and the way it depends on the irradiation conditions allowed us to produce more complex and custom tailored nanostructures by multiple irradiation of the sample under different azimuthal angles or even continuous rotation. Additional irradiation after an azimuthal rotation of the target by 90° again induces cracking and shrinking of the material, perpendicular to the already existing cracks. That way, rectangular structures evolve as shown in Fig. 2. With a combination of a light and a heavy ion-species in the subsequent irradiations, more

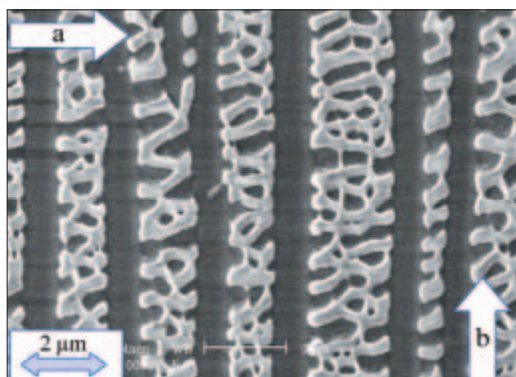


Fig. 4: Combination of Ar- and Au-irradiation, 40 nm NiO/SiO₂: nano-script

elongated structures are achieved (Fig. 3). When very thin NiO films are used, very complex patterns – like the *nano-script* shown in Fig. 4 – can be generated.

If one irradiates an existing structure at grazing SHI-incidence and under continuous azimuthal sample rotation, one can achieve an almost uniform reduction of its lateral dimensions, as is demonstrated in Fig. 2b. Consequently we have tried, instead of producing quadratic pillars by double-irradiation, to use multiple irradiations (0°, 90°, 135°, 225°, ...) and generate polygon-like structures. By finally irradiating these under continuous azimuthal rotation, we wanted to arrive at circular cylinders with diameters as small as possible. The result can be seen in Fig. 5, which shows a perspective view of a sample treated as described before. In fact, we were able to produce NiO *nano-towers* with a diameter of about 200 nm and a height of about 2 μm. The alignment of the *nano-towers* is rather regular, reflecting the periodicity of the crack formation described above. The towers cover only about 5% of the substrate surface. Since the wavelengths of the cracks depend on the film thickness the number density of the *nano-towers* decreases exponentially with the initial NiO thickness.

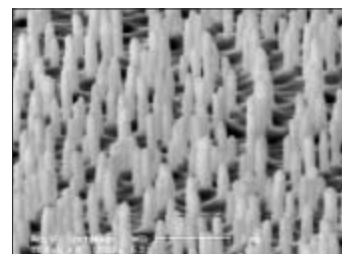


Fig. 5: Perspective SEM image of a NiO/SiO₂ sample after multiple single-step irradiations and subsequent continuous rotation irradiation. For details see text.

In conclusion we have demonstrated the very impressive potential of SHI to generate large-area covering nano-structures by initiating surface instabilities and self-assembly processes. The structures can be very much custom-tailored by choosing proper irradiation conditions.

- [1] W. Bolse, B. Schattat, A. Feyh, *Appl. Phys. A* **77**, 11 (2003)
- [2] A. Feyh, diploma thesis, Stuttgart University (2002)
- [3] D. Etissa-Debissa, master thesis, Stuttgart University (2003)
- [4] M. Kalafat, diploma thesis, Stuttgart University (2002)
- [5] H. Trinkaus, A.I. Ryazanov, *Phys. Rev. Lett.* **74**, 5072 (1995)
- [6] M.A. Grinfeld, *Dokl. Akad. Nauk. SSSR* **290**, 1358 (1986), D.J. Srolovitz, *Acta Metall.* **37**, 621 (1989)
- [7] S. Klaumünzer, G. Schumacher, *Phys. Rev. Lett.* **51**, 1987 (1983)

Corresponding author:

W. Bolse
bolse@ifs.physik.uni-stuttgart.de

10 years of materials analysis with heavy ions at ISL

W. Bohne, J. Röhrich, E. Strub

■ HMI, SF4

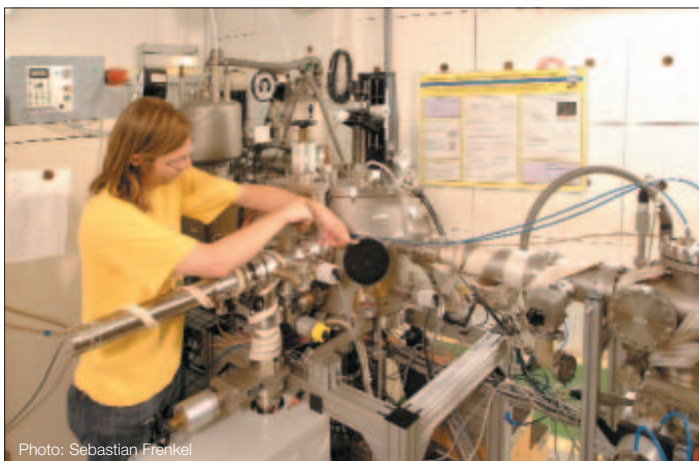


Photo: Sebastian Frenkel

Fig. 1: The time-of-flight ERDA set up

After finishing the nuclear physics research activities at VICKSI in the early nineties we started to use the modified accelerators as tools for materials characterisation. At first in 1994, a relatively simple set up was installed at the low energy beam line TR of the Van-de-Graaff accelerator to perform HI-RBS (Heavy Ion Rutherford Backscattering Spectroscopy) measurements. With 15 MeV N ions as projectiles and a detector system with a large solid angle of 22 msr a good detection sensitivity as low as 10 ppm for heavy elements in light matrices and a much better mass resolution compared to standard RBS with He beams was achieved. But, due to the dependence of the Rutherford cross section on mass and on the atomic number of the sample atom, the sensitivity decreases to only about 0.1% for light elements. And elements lighter than Ne are not detectable at all. To overcome these restrictions and drawbacks we decided to implement the ERDA method (Elastic Recoil Detection Analysis) which will be described a bit more in detail in the next paragraph.

ERDA is the complementary part of the RBS. Instead of detecting at backward angles the elastically scattered projectiles the corresponding recoiling ions of the sample constituents are measured. The situation is more complica-

ted because we are not dealing with the well known mass of the projectiles but with the normally unknown elements from the sample. That implies that in addition to the energy the mass of the recoils must be determined, that is, an energy and mass dispersive spectrometer becomes necessary. So for all contributing elements the corresponding energy spectra yield the same information as an RBS spectrum but now separately for each element. The intensity gives the atomic concentration and from the measured energy the depth where the scattering happened can be calculated. In contrast to RBS, **all** chemical elements can be detected simultaneously and the Rutherford cross section in the frame of the recoils is almost constant for all elements and even by a factor of four enhanced in the case of hydrogen, i. e., all elements are detectable with the same sensitivity. Like for RBS, the basic process for ERDA is the elastic Rutherford scattering for which the cross section can be calculated exactly. Therefore, ERDA is an absolute and quantitative method which does not need standard samples. All these advantages make ERDA a very valuable method to analyse complicated new materials.

To implement this nice technique, we designed in parallel to the operation of RBS a set up for ERDA. Owing to our experiences from nuclear physics experiments, we decided to make use of the time-of-flight (TOF) method for the mass

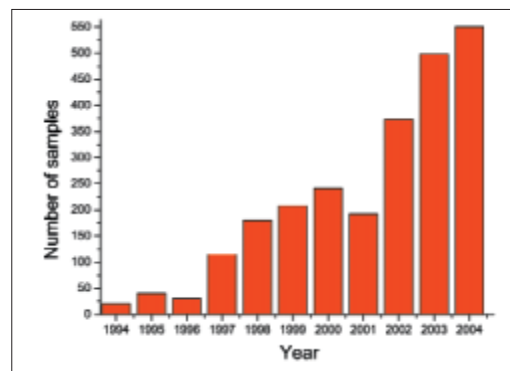


Fig. 2: Number of analysed samples per year

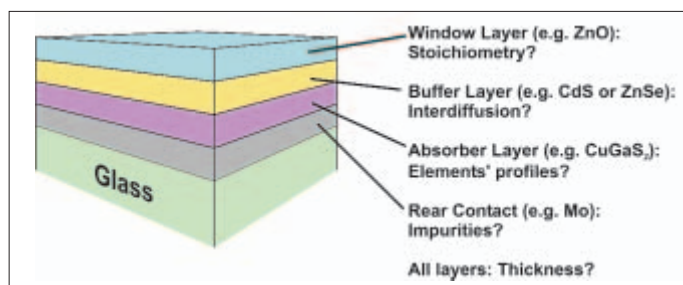


Fig. 3: Sketch of a thin film solar cell and typical questions that can be answered by ERDA

identification, because this technique offers the best dynamic energy range concerning mass separation, i. e., analysable depth. When simultaneously measuring the energy E and the corresponding velocity v via the flight time of each recoil and displaying this data in a two-dimensional spectrum, the *scatter plot*, all events of a certain mass M are grouped on one curve according to the relation $E = 1/2 Mv^2$. After disassembling the nuclear physics experimental set up, the spectrometer was realised at the high energy beam line TC. Figure 1 shows the present status. With this set up a detection sensitivity for all elements of about 10 ppm and a depth resolution in the 10 to 50 nm region, depending on depth, can be achieved. Films with a thickness of a few mono-layers up to some microns become analysable. A detailed description is given in [1]. Already in summer 1996 the first experiments had been performed. After presenting the first results, many materials scientists took stock in this method and the amount of samples we analysed grew steadily as demonstrated by Fig. 2.

Since the late nineties the new materials for the construction of thin film solar cells are a main focus of the ERDA studies. A fruitful collaboration between the ion-beam analysis and many groups from the solar-energy department at the Hahn-Meitner-Institut has developed, now using about 60% of the ERDA beam time. A thin film solar cell consists of several layers on a substrate as schematically depicted in Fig. 3. Especially in the case of the chalcopyrite cells, different physical and chemical deposition methods are implemented for the absorber, for the buffer, and for the TCO-window layer as well, resulting in various problems concerning contamination, stoichiometry, homogeneity, etc. By ERDA measurements many of these questions for certain layers and complete stacks have been answered, often allowing an improvement of the deposition process and of the quality of the cells. As an exam-

ple Fig. 4 shows the scatterplot obtained with 350 MeV Au ions as projectiles from a heterojunction consisting of a ZnSe buffer on a Cu(In,Ga)(S,Se)₂ absorber with a Mo back contact deposited on glass. The apprehension was that at higher temperatures used for the chemical vapour deposition (CVD) of the ZnSe an interdiffusion of elements of the absorber and buffer may happen. And indeed, at process temperatures above 350°C the diffusion of In into the buffer was observed [2, 3]. By the way, the iodine used as transport medium for the CVD can be clearly seen as a contamination in the ZnSe film. The inset, showing the surface region, demonstrates that due to the good mass resolution a separation of the overlapping Cu and Zn is possible with the aid of the well isolated ⁶⁸Zn isotope.

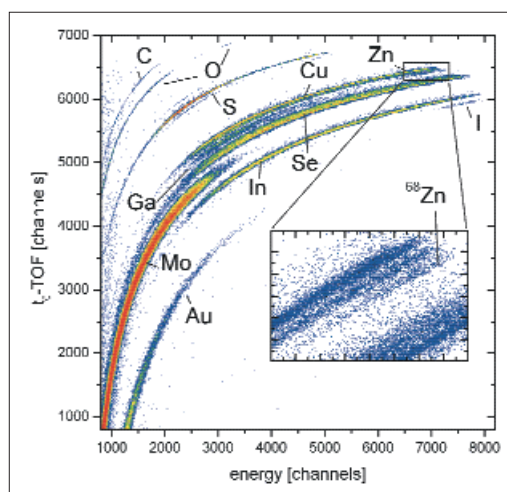


Fig. 4: Time-of-flight vs. energy spectrum for a heterostructure Cu(In,Ga)(S,Se)₂/ZnSe (~1000/70 nm thick) on Mo covered glass measured at 40° with a beam of 350 MeV Au. The inset shows in detail the Cu/Zn interface region.

- [1] W. Bohne, J. Röhrich, G. Röscher, Nucl. Instrum. and Meth. B **136–138**, 633 (1998)
- [2] W. Bohne, S. Lindner, J. Röhrich, Nucl. Instrum. and Meth. B **188**, 1–4, 55 (2002)
- [3] S. Lindner, W. Bohne, A. Jäger-Waldau, M. Ch. Lux-Steiner, J. Röhrich, G. Vogl, Thin Solid Films **403–404**, 432 (2002)

Corresponding author:

W. Bohne
bohne@hmi.de

Investigation of heavy metal release during thermal waste treatment on a forward-acting grate using radiotracers irradiated at BER II

T. Jentsch¹, D. Alber²

■ 1 Fraunhofer Institute for Nondestructive Testing, Branch Lab Dresden, Germany ■ 2 HMI, SF6

The possibilities for optimizing the process control in the so-called classical combustion of residual waste in grate systems have not yet been completely explored. One of the main objectives of the optimization is the improvement of the ash quality. The immediate goal of these investigations is the production of an ash that can be implemented in the construction industry with the condition that the necessary quality is achieved by primary measures, i.e. the process control itself, only. A prerequisite for this is the maintenance or reduction of the eluate and solid concentration of inorganic salts and heavy metals below the limiting values. The process conditions (in particular temperature, gas atmosphere, residence time) are adjusted in such a way that these pollutants are either evaporated and are therefore not present in the ash or are strongly mineral-bound in such a manner that they no longer leach out. Results concerning the behaviour of heavy metals and salts are available from experiments performed in batch operation on laboratory scale, i.e. using small charges (several g to kg). In order to be able to transfer this knowledge into practice and to optimize the process on a

large scale, one has to determine the location and amount of heavy metal evaporation under realistic conditions, in other words in a continuously-operated pilot plant.

The heavy metal content is usually determined by sampling the total flue gas flow and a subsequent analysis of the gases. Detecting the heavy metals directly at the location of evaporation using conventional sampling and analysis is, due to the harsh conditions in the combustion chamber, particularly difficult. The analysis itself cannot be carried out on-line. In addition, a very complex measurement network is necessary for an investigation covering the complete firing bed surface.

The radiotracer method provides the opportunity to follow the behaviour, location and concentration of a certain heavy metal species on-line during the entire combustion process in a technical waste treatment plant. When the combustion process in a grate system on the pilot plant-scale is used as an example, the following quantities can be determined with this method:

- the location of the heavy metal evaporation,
- the time course of the heavy metal evaporation,
- the amount of heavy metal evaporated.

The investigations discussed here were carried out in a pilot plant-scale forward-acting grate at the Clausthaler Umwelttechnik Institut GmbH (CUTEC) in Clausthal-Zellerfeld. Figure 1 shows the grate and the combustion chamber as the main components of the plant. The plant has a thermal capacity of 0.4MW, so a transfer of the results obtained to the industrial scale possible. A model fuel, consisting of 60 mass-% wood,

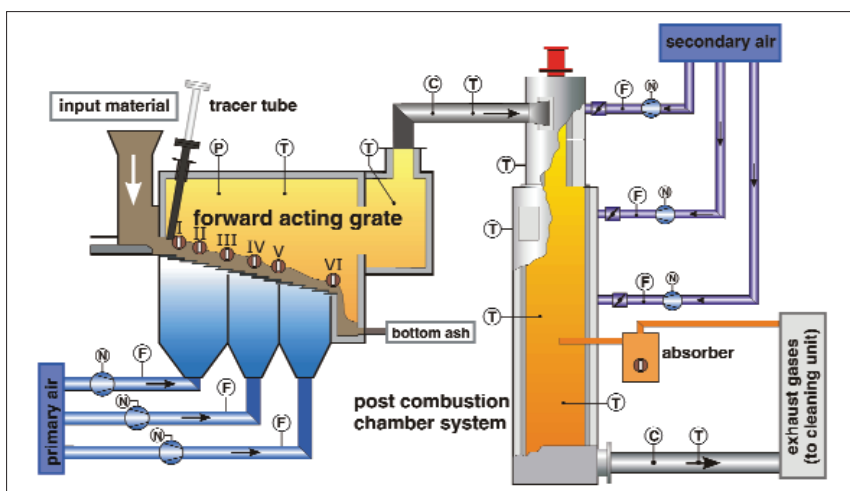


Fig. 1: Technical flowchart of the forward-acting grate plant (D radiation detector)

30 mass-% lava, and 10 mass-% RDF (refuse derived fuel), was used for the investigations. The pilot plant was operated steady-state with a fuel mass flow of 60 kg/h.

Out of the many elements of interest, copper and zinc were selected for the investigations in the pilot plant. Copper is representative of the nearly nonvolatile elements and zinc of a species which can be easily evaporated under certain conditions.

^{64}Cu and $^{69\text{m}}\text{Zn}$ ¹ were used as tracers for copper and zinc, respectively. The radioactive isotopes were generated by irradiation of metallic granules of ^{63}Cu or ^{68}Zn in the research reactor BER II. The tracer (^{64}Cu and $^{69\text{m}}\text{Zn}$ in different experiments), embedded in a RDF-pellet, was given into the plant as a short pulse (a so called DIRAC-impulse) by a special tracer tube (Fig. 1). Narrow-collimated and well shielded radiation detectors located along the sides of the grate registered the time course of the tracer concentration in the waste mass flow at different positions. They allowed for a determination of

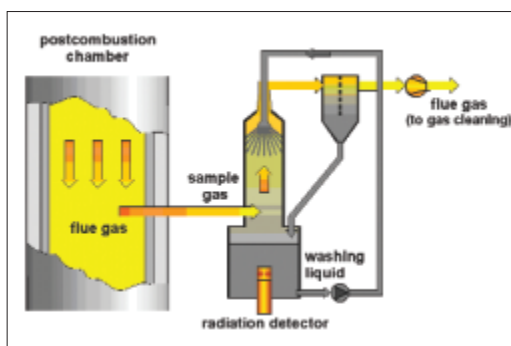


Fig. 2: Scheme of the absorber for the washing of the partial gas flow and quantification of the amount of heavy metal tracer evaporated

the location of the marked heavy metal species during the entire residence time in the solid bed. The heavy metals evaporated during the combustion process and carried out of the combustion chamber with the flue gas are caught to a certain degree by the absorber (Fig. 2). A radiation detector in this absorber registers the temporal concentration course of the heavy metal tracer evaporated. Since the collection of measured values by all detectors was started simultaneously with the introduction of the tracer, concentration changes in the time course of the measured signal at the absorber detector in the range of the combustion chamber could be assigned and the heavy metal evaporation could then be localized in the solid bed.

The quantification of the amount of heavy metal evaporated was made possible by a calibration of the absorber detector signal.

Figure 3 and Fig. 4 show exemplary the results of a copper and zinc evaporation experiment, respectively. The lower diagrams in the figures show the measuring results of the detectors positioned alongside the grate, the upper diagram the time course of the absorber detector signal.

In all experiments, a copper evaporation of 3 or 5% could be established. As can be seen in the upper diagram in Fig. 3, the evaporation takes place continuously during the entire tracer residence time on the grate. In contrast, an almost complete zinc evaporation could be observed, which takes place within a time period of a few minutes in a narrowly restricted section of the grate, in the section in which the local reducing conditions prevail.

Due to the fluctuations of heavy metal content and specification in the waste, clearer results could be obtained with the help of radiotracer measurement than by means of a classical mass flow analysis.

The project was financially supported through the Schweizerischer Nationalfonds (Swiss national fund), whom the author would like to thank.

¹ The letter m in the superscript indicates the metastable state of an isotope.

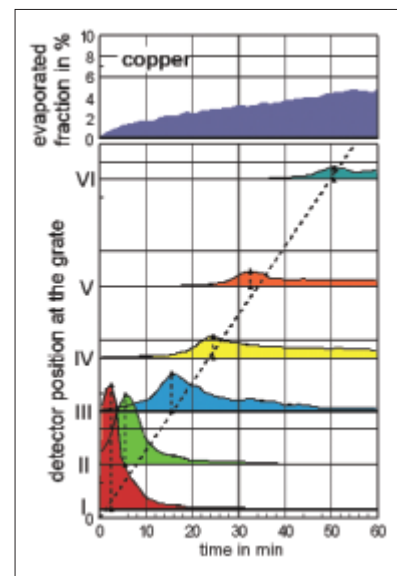


Fig. 3: Results of a copper evaporation experiment

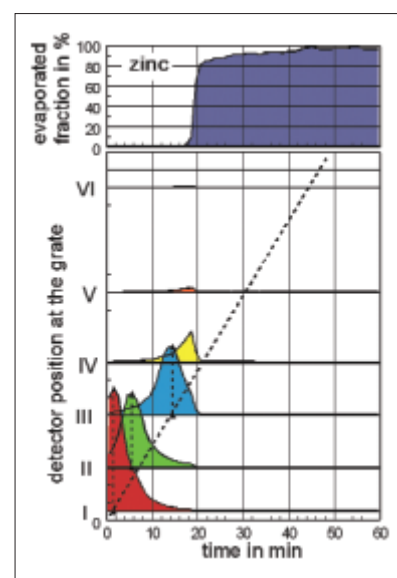


Fig. 4: Results of a zinc evaporation experiment

Corresponding author:

T. Jentsch

thorsten.jentsch@izfp-d.fraunhofer.de

Ordering upon melting dynamically enhanced

O. Russina¹, A. Triolo², F. Mezei¹, M. Russina¹

■ 1 HMI, SF1 ■ 2 Istituto per i Processi Chimico-Fisici, C.N.R., Messina, Italy

To understand the relation between molecular structure, dynamics and properties in non-crystalline matter [1] is of great current interest in nanoscale phenomena. Indeed, macromolecular systems, such as polymers and biopolymers are examples of pronounced local structures on the nanoscale, as shown in Fig. 1 by the neutron diffraction pattern measured in deuterated atactic polypropylene (DaPP), a representative of the class of polyolefins. Due to its chemical architecture, this form of polypropylene is fully amorphous over its thermal stability window. Accordingly, it is an ideal model system to investigate the correlation between structure and dynamics in amorphous materials. The local range order appears as a peak around 3.2 \AA^{-1} in the structure factor $S(Q)$ and reflects the atomic space correlation between close neighbours inside the chain (intra-chain order). The nearest neighbour interchain distance is reflected in the peak around 1.1 \AA^{-1} (interchain order).

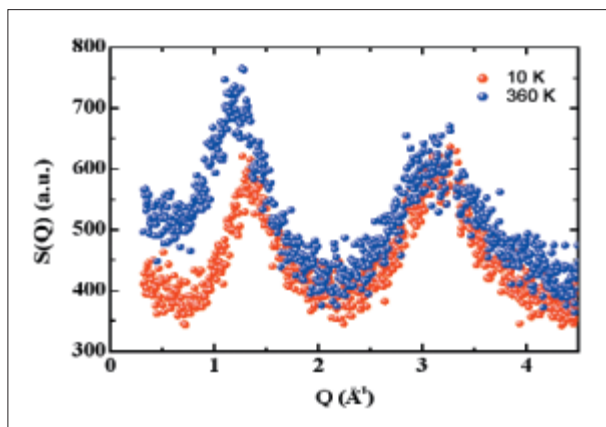


Fig. 1: Structure factor, $S(Q)$, of DaPP at two selected temperatures, below and above the glass transition ($T_g = 280 \text{ K}$). Data were collected at the E9 diffractometer

While the intramolecular peak does not change significantly with temperature, the intermolecular peak moves to smaller Q values and its amplitude increases with temperature. This shift of the peak position is mainly related to thermal expansion density change. However, the rise of its amplitude is remarkable and indicates an increase of the interchain correlation in the melt state (360 K) as compared to the glassy one (10 K). This strong increase of order upon heating and melting is very much in contrast with the usual notion that order is reduced by thermal motion.

Inelastic neutron scattering allows us to observe the evolution of this order in time via the determination of the dynamic structure factor, $S(Q, \omega)$. Here as the wave number Q is related to the distance as $r \sim 2\pi/Q$, the energy ω is related to the time by the relation $t \sim 1/\hbar\omega$. DaPP was investigated at the time-of-flight spectrometer NEAT. $S(Q, \omega)$ was measured at different temperatures ranging from the glassy state (20, 150 and 200 K) to the melt (300 and 340 K). After standard corrections (subtraction of background and correction for absorption) the data were corrected for multiple scattering in order to achieve the “real” scattering function. A selection of these data is presented in Fig. 2.

The intensity of the elastic peak forms the long time (*elastic*) structure factor $S_{el}(Q)$, showing the order that survives rather long times of about 0.1 ns. The temperature dependence of $S_{el}(Q)$, presented in Fig. 3, shows that the long-time interchain order decreases as usual with temperature.

The time of flight data, $S(Q, \omega)$, in Fig. 2 evidence a strong increase of the scattering intensity in the small energy exchange range ($\Delta E < 1.5 \text{ meV}$). This scattering is associated with correlations over characteristic times in the picosecond range and its existence is a general feature of dynamics in glass formers. We determined the structure factor associated with these dynamic correlations $S_{\text{inel}}(Q)$ by integrating $S(Q, \omega)$ between 0.04 and 1.1 meV, as shown in Fig. 3. The peak of $S_{\text{inel}}(Q)$ around 1.1 \AA indicates that contrary to the longer time correlations, the interchain order on the picosecond scale increases with increasing temperature, and it explains the anomalous increase of this order shown in Fig. 1. Thus we conclude that the surprising increase of the nanoscale order with increasing temperature in this polymer – even more surprisingly – is due to enhanced order on the picosecond time scale between much shorter times of atomic vibrations and the time limit $t > 0.1 \text{ ns}$, for which conventional macroscopic behaviour is observed. We believe that this radically new phenomenon of dynamically enhanced order with increasing temperature is an important clue to understand glassy systems.

*The main consequence of this finding is that the higher degree of order observed in the melt (as compared to the glassy state) has a **dynamic nature**, arising from the correlation of atomic motions over a time scale of order of the characteristic time of the fast dynamics (picosecond regime). While the static structure (with infinite lifetime) decays, the fast atomic motions are correlated.*

In conclusion, by using complementary neutron scattering techniques, we provided a novel interpretation for the concept of order in glass forming materials.

Acknowledgements

We should like to thank Dr. D.M. Toebbens for his support during the measurements at the E9 diffractometer.

[1] See e.g.: N. McCrum, B. Read, G. Williams, *Anelastic and Dielectric Effects in Polymeric Solids*; Wiley: London (1967)

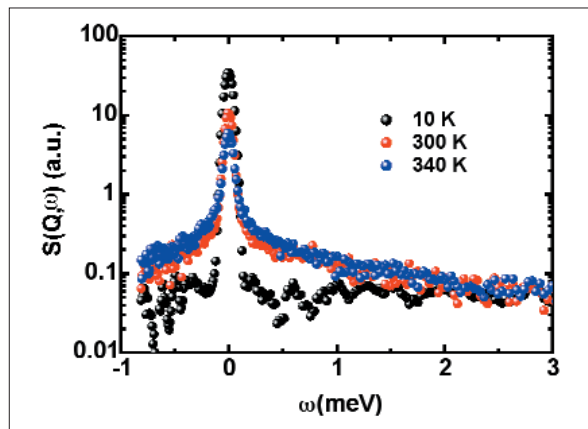


Fig. 2: Selected time of flight data of DaPP, $S(Q, \omega)$, collected at the NEAT spectrometer, at $Q_{\text{elastic}} = 1.6 \text{ \AA}^{-1}$

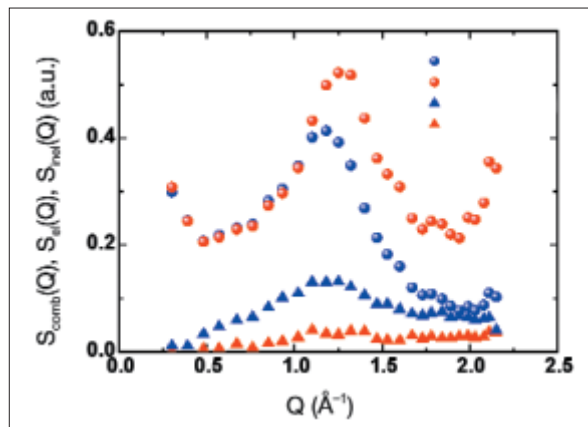


Fig. 3: Temperature dependence (red symbols for $T = 20 \text{ K}$, blue symbols for $T = 300 \text{ K}$) for the different structure factors defined in the text (see the text for details)

Search for scission neutrons using angular correlation method

E. Korobkina¹, R. Golub¹, T. Wilpert¹, G. Danilyan², A. Fedorov², I. Karpikhin², V. Krakhotin², V. Pavlov²,
 ■ 1 HMI, SF1 ■ 2 A.I. Alikhanov Institute for Theoretical and Experimental Physics, Moscow, Russia

More than 65 years ago Otto Hahn, Lise Meitner and Fritz Strassmann discovered the nuclear fission process. Nevertheless, today we still do not know very much about some of the fundamental aspects of fission. For example – we know that fission of the nucleus is accompanied by the emission of prompt neutrons (PFN). The angular distribution of such neutrons relative to the fission axis can be described at least by two components: most of them are elongated along the fission axis, while another part shows approximately a spherically symmetric distribution. It is evident that the former is evaporated by accelerated fission fragments because the elongation can be the result of kinematics only. But what is the nature of the second part? A spherically symmetric distribution means that the neutrons are evaporated by the nucleus before rupture of the neck at the scission point. So they were called *scission neutrons*.

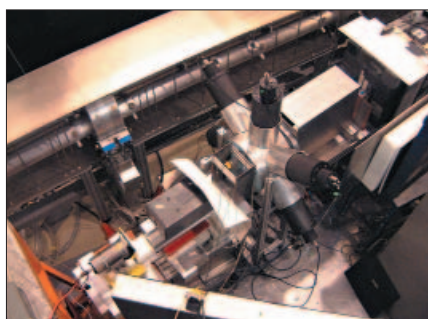


Fig. 1: A general view of the experiment on the cold neutron beam V13 during the adjustment of the set-up in 2003

Now we must mention that there is one exotic mode of fission, which is called *ternary fission*. This is the fission into two fragments accompanied by the emission of a charged light particle as p, d, t, ³He, ⁴He, ³He and so on. The angular and energy distribution of these particles shows that

they are emitted from the region between the two fragments. Most models of ternary fission describe it as evaporation from the neck at the scission point. But why does ternary fission not include neutrons? The evaporation of a neutron is easier than of a proton because for the former there is no Coulomb barrier. Is a scission neutron the neutral component of ternary fission? This is not easy to answer because in experiments it is practically impossible to distinguish between them and fragment neu-

trons due to the overlap of the energy-angular distributions. A lot of analysis has been performed to evaluate the probability of scission neutron evaporation. The estimates of the ratio of scission neutron to the total number of PFN vary from 1% to 35%! It is a result of arbitrary assumptions made in different analyses (see review in [1]). Thus it is high time to work out an alternative method to search for the scission neutrons.

It is well known that any angular correlation is a result of the interference of angular momenta. So because this is a quantum-mechanical effect, both, the magnitude and the sign of the correlation coefficients depend on the quantum numbers of the initial and final state as well as on the quantum characteristics of the outgoing particle. When the condition of the experiment does not allow us to choose a definite quantum state (initial or/and final), the observables will be the result of averaging over all N states involved in reaction. It means that any coefficient will be suppressed by a factor $1/N^{1/2}$. Concerning the fission process, it must be emphasized that the number of fragment's final states is an order of 10^8 . Therefore any angular correlation of particles emitted by fragments will vanish. In contrast, the number of initial and final states of the scission neutron should be rather small because they are evaporated by a cold, strongly deformed fissile nucleus. Thus a scission neutron can possess a non vanishing angular correlation with the spin of the compound nucleus. This is the main idea of our new approach to how to distinguish between scission and fragment neutrons.

It is well known that due to the weak interaction nuclear states do not possess a definite parity [2]. Therefore, there is always a P-odd term in the angular distribution of any particle emitted from an excited state of the nucleus. We decided to measure the P-odd asymmetry, i.e., a correlation between the momentum of scission neutrons, \mathbf{n}_{sc} , and the incident beam polarization, σ_{in} :

$$W \sim \{1 + A_{sc}(\sigma_{in}, \mathbf{n}_{sc})\}.$$

In reality we detect all prompt fission neutrons, because we cannot distinguish between them. Fragment neutrons imply the background that decreases the observable asymmetry. The magnitude of suppression depends on the angle relative to the fission axis. This angular dependence can be used to estimate the relative part of the scission neutrons.

The experiment is running on the polarized cold neutron beam V-13 with intensity $10^7 \text{ s}^{-1} \text{ cm}^{-2}$ (see Fig. 1). The layout of the experiment is shown in Fig. 2. Scintillation detectors detect both prompt fission neutrons and gammas. To distinguish between them we use a *time-of-flight* technique. Start comes from the fragment detectors in the fission chamber and stop comes from the neutron detector. On the TOF spectrum (Fig. 3) one can see both, gamma (narrow) and neutron (wide) peaks. The former are used to test systematic, because there is no P-odd asymmetry of γ -quanta emitted from fragments.

Our data taking during 2004 results in the following values of neutron and gamma asymmetry (both measured at 90° relative to fission axis)

$$A_n = (+2.7 \pm 0,8) \times 10^{-5}$$

$$A_\gamma = (-0.1 \pm 0,6) \times 10^{-5}$$

Thus we indeed have observed a pronounced effect for neutrons and no asymmetry of the gamma quanta.

Taking into account that the expected value of P-odd asymmetry of scission neutrons is of the order of 10^{-4} , our preliminary result means that the relative amount of scission neutrons is about 25% [3]. This is already the second angular correlation found for prompt neutrons [4]. It is extremely surprising and challenging for the theory of fission. Nevertheless, the present asymmetry value still has to be measured at different angles to allow more reliable evaluation. This is planned for 2005.

- [1] N. V. Kornilov, A. B. Kagalenko, F.-J. Hamsch, *Physics of Atomic Nuclei* **64**, 1373–1385 (2001); *ISINN-7*, Dubna, 241–248 (1999)
- [2] G. V. Danilyan, *Soviet Physics – Uspekhi* **23**, 323–330 (1980)
- [3] E. V. Brakhman, G. V. Danilyan, A. V. Fedorov, I. L. Karpikhin, V. A. Krakhotin, V. S. Pavlov, R. Golub, E. I. Korobkina, T. Wilpert, *JETP Lett.* **76**, 837 (2004)
- [4] G. Danilyan, *et al.*, *JETP Lett.* **76**, 697–699 (2002)

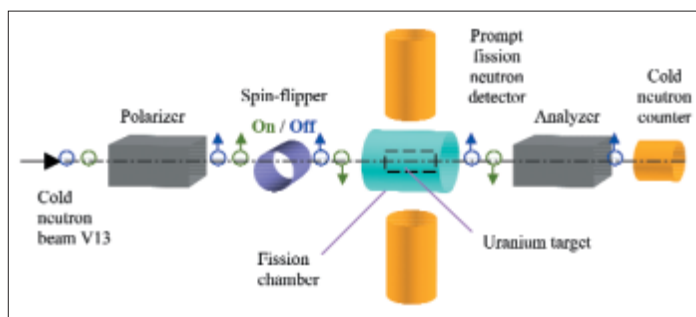


Fig. 2: Experimental layout. First cold neutrons are polarized vertically by a polarizer; then they pass through a spin-flipper, which reverses the polarization once per second. A large area uranium target inside the fission chamber is aligned along the beam. Fission fragments are detected by two sets of avalanche counters in the horizontal plain and prompt fission neutrons are detected by plastic scintillator detectors in the vertical plain relative to the beam axis. The analyzer and neutron detector behind the fission chamber are used to monitor both, neutron polarization and beam count rate.

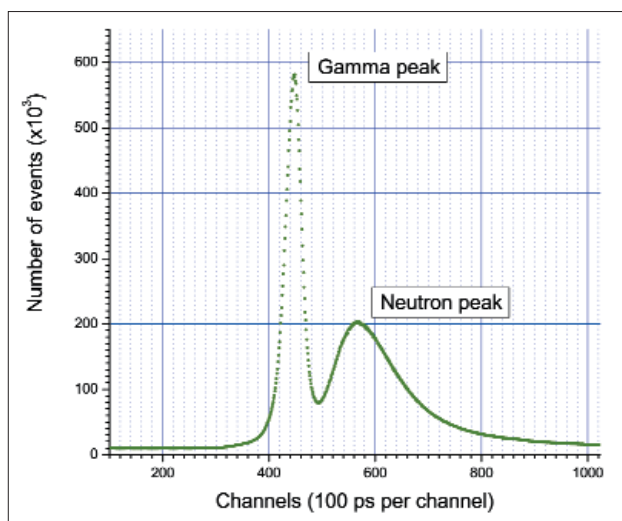


Fig. 3: Time-of-Flight spectrum of a neutron detector. The neutron detector does not only detect prompt fission neutrons but also the prompt fission gamma radiation. To distinguish between them, the difference in neutron and gamma-quantum velocities is used, i. e., a *time-of-flight* technique with a *start* from fragment and *stop* from a gamma or neutron. In the delay time spectrum one sees the narrow gamma-peak and the wide pike of prompt fission neutrons.

Corresponding author:

E. Korobkina
korobkina@hmi.de

Superconductivity? Just add water!

D. N. Argyriou¹, C. J. Milne¹, A. Chemseddine², N. Aliouane¹, J. Veira¹, S. Landsgesell¹, D. Alber³

■ 1 HMI, SF2 ■ 2 HMI, SE4 ■ 3 HMI, SF6

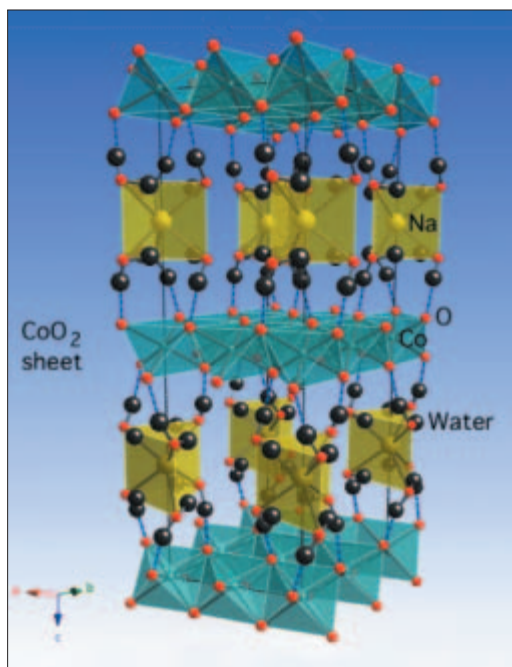


Fig. 1: The crystal structure of superconducting $\text{Na}_{0.3}\text{CoO}_2 \times 1.3\text{H}_2\text{O}$ determined using neutron powder diffraction at the Hahn-Meitner-Institut. [5] Our work found that Na is surrounded on average by six water molecules as shown in the figure forming triangular prisms with Na at the center and Oxygen (from the water) at the corners.

Superconductivity, the passage of electrical current with no resistance, is a unique phenomenon in physics exhibited by a relatively small number of materials at low temperature. Because of this unique property, superconducting materials can be used in a huge array of different applications from MRI scanners to particle accelerators. Researchers are constantly searching for new superconducting materials in the hope of increasing their T_c , the temperature below which they become superconducting. These searches sometimes yield surprising results. Recently Takada [1] from the National Materials Science Institute in Japan discovered that if he intercalates water between the CoO_2 and Na layers, in the oxide $\text{Na}_{0.3}\text{CoO}_2$ this material becomes superconducting.

At the Hahn-Meitner-Institut, we have examined the chemistry and structure of this new superconductor in great detail to understand how it becomes a superconductor. We hope that what we learn from this will help the search for better superconducting materials.

Electrons vs Holes

For an oxide material to become superconducting we first need to inject it with charge carriers, electrons or holes (lack of electrons), so an electrical current can pass through the material. Whether the charge carrier is an electron or hole is very important for the physics, as these two entities have different masses (the mass of the electron vs the mass of nothing!). The amount of charge carriers one can inject in to the material is called the electronic doping. These carriers are injected into the CoO_2 layer, the layer that is thought to conduct electricity.

A characteristic feature of the cuprate superconductors, materials with the highest known T_c (165 K), is the existence of an optimal electronic doping that gives a maximum superconducting transition temperature. This composition separates the underdoped and overdoped regimes in which T_c decreases from the optimal value. This behaviour is thought to be a universal characteristic of cuprate superconductors that arise from the fundamental origin of superconductivity for these oxides. The highest T_c is achieved when the CuO_2 sheets are doped with holes (about 0.15 to 0.3 holes for every Cu atom).

To test if this idea also holds for these new superconductors one needs to measure T_c as a function of the electronic doping. In these hydrate superconductors it was first thought that this could be done by varying the amount of Na between the CoO_2 sheets [2]. If one considers as a base line the amount of electrons for Co^{4+} (5 electrons), each Na atom will add 1 electron per Co-atom in addition to the 5 electrons of Co^{4+} (LS: t_{2g}^5). However, Takada found that the chemistry was not so simple, and Na alone does not control the number of charge carriers that are injected into the CoO_2 sheet [3]. He realized that along with water that is interlaced between Na and CoO_2 sheets (see Fig. 1), there are also H_3O molecules. A H_3O molecule looks like water in many ways, but it has one extra H-atom which is charged and therefore donates an additional electron. As a result the superconducting phase diagram had to be rethought completely.

At the Hahn-Meitner-Institut we synthesized a large number of samples and measured the valence of Co directly using chemistry [4]. What we found was very surprising and told us that these materials are indeed very similar to the cuprate superconductors. We found that superconductivity is achieved when holes are added to the CoO_2 layer, and not electrons as it was originally thought [2]. In fact if we use as base line Co^{3+} , that has 6 electrons in its outer core (LS: t_{2g}^6), each Na and H_3O together act to remove one electron from Co^{3+} , thus injecting a hole in the CoO_2 layers. There is some very complex chemistry that occurs between the Na and the water so that changing significantly the amount of Na between the CoO_2 sheets it affects significantly the amount of H_3O^+ that enters the material.

We find that optimum T_c is achieved over the cobalt valence range of 3.24–3.35, while T_c decreases for valence states >3.35 (see Fig. 2). This is in stark contrast to the previous measurements by Schaak et al. [2] in which it was assumed that Na alone sets the electronic doping. Our work, in contrast, demonstrated that these materials are hole doped with respect to Co^{3+} . Also the width of the region where superconductivity occurs looks to be very similar to the cuprate superconductors. This work helps us understand that superconductivity for all its novelty and interest may be a more common state in matter than we previously thought. The search continues to find better materials so we can harness the opportunity that they offer.

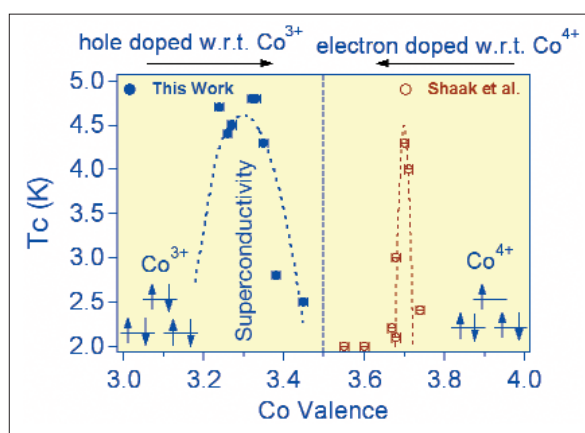


Fig. 2: The superconducting phase diagram of $\text{Na}_x\text{CoO}_2 \cdot y\text{H}_2\text{O}$, determined at the Hahn-Meitner-Institut

- [1] K. Takada, H. Sakurai, E. Takayama-Muramachi, F. Izumi, R. A. Dilanian, T. Sasaki, *Nature* **422**, 53 (2003)
- [2] R. E. Schaak, T. Klimczuk, M. L. Foo, R. J. Cava, *Nature* **424**, 527 (2003)
- [3] K. Takada, *et al.*, *J. Mater. Chem.* **14**, 1448 (2004)
- [4] C. J. Milne, D. N. Argyriou, A. Chemseddine, N. Aliouane, J. Veira, S. Landsgesell, D. Alber, *Phys. Rev. Lett.* **93**, 247007 (2004)
- [5] D. N. Argyriou *et al.* *Journal of Physics: Condensed Matter* (in press)

Corresponding author:

D. N. Argyriou
argyriou@hmi.de

Competition of two AF structures in UNiAl single crystal

K. Prokeš¹, E. Brück², V. Sechovský³

■ 1 HMI, SF2 ■ 2 Van der Waals-Zeeman Inst., University of Amsterdam, The Netherlands

■ 3 Dept. of Electronic Struct., Charles University, Prague, The Czech Republic

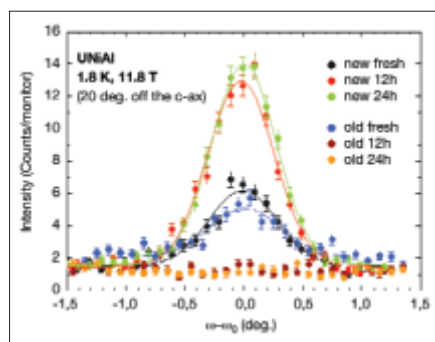


Fig. 1: Rocking curves through the new (1.173 0 0.5) and the old (1.1 1.1 0.5) magnetic reflections just after reaching 11.8 T (fresh) and after 12 and 24 hours

UNiAl forms in the hexagonal ZrNiAl type of structure and orders anti-ferromagnetically (AF) below $T_N=19.3$ K. Below T_N , new Bragg peaks due to magnetic order appear that are indexable considering a propagation vector $q_{old}=(0.1 \ 0.1 \ 0.5)$ of the AF structure. The magnetic-structure refinement points to two U moments (amplitude of $1.28 \mu_B$) in the UNiAl unit cell coupled together ferromagnetically

and the third one, uncoupled due to symmetry, which is much smaller ($0.8 \mu_B$) [1]. When a magnetic field $H||c$ is applied at temperatures lower than $\approx 0.5 T_N$, UNiAl undergoes a sharp MT at $\mu_0 H_c \approx 11.35$ T (4.2 K) [2] towards a high field ferromagnetic (HFF) phase. Neutron diffraction experiments in magnetic fields confirmed the HFF phase with a unified U moment $\mu_U \approx 0.9 \mu_B$. Some time ago, magnetic history dependent phenomena were revealed in UNiAl, which concern all the bulk properties [3]. Original neutron diffraction studies suggested that below 7 K after applica-

tion of a magnetic field higher than about $8 \div 9$ T the original AF structure disappears and after releasing the field a new AF structure characterized by $q_{new}=(0.173 \ 0 \ 0.5)$ appears [4]. The difference between the “old” and “new” AF structures is that the sine-wave modulation of U moments (having the same amplitude) is along the [110] in the former and [100] in the latter case.

In order to study stability and competition of the two phases in the experimental arrangement with a small vertical opening of the magnet capable to produce sufficient magnetic field we had to turn the crystal by $\sim 20^\circ$ around the [100] direction in order to reach two characteristic magnetic reflections – namely (1.1 1.1 0.5) and (1.173 0 0.5); the former will be called “old” and the latter “new”. The study was performed on the triple axis spectrometers E1 and V2 and double-axis diffractometer E4 installed at the Hahn-Meitner-Institut Berlin using the incident wavelengths of 2.4, 4.6 and 2.4 \AA , respectively. Since the c -axis of the crystal in our experiment is deflected from the field direction (vertical axis) by $\sim 20^\circ$ the critical field to a ferromagnetic state is crossed at 12.14 T. However, Fig. 1 shows that the new AF state is established even after being exposed for ~ 12 hours to only 11.8 T, which confirms that we do not need to cross the B_C .

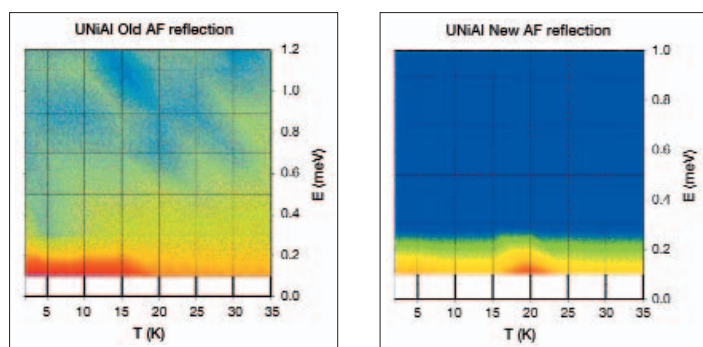


Fig. 2: Low-energy signal measured on V2 at the old (left: log scale) and new (right: linear scale) magnetic reflections at zero field upon cooling. Note significant signal around T_N in the case of the new reflection.

When decreasing the field to zero, intensities relax to their original values, however, much slower. No clearly defined excitations could be resolved up to 8 meV energy transfer in either of the phases. This is obviously due to the sine-wave modulation of U moments leading to a spread of the exchange energy. The response function in UNiAl consists of many contributions having small intensities and centered at different energy transfers.

In Fig. 3, we show the contour plots of the temperature dependencies of the quasielastic response function measured at the two characteristic reflections (old at the top) at various magnetic fields obtained on E1. As can be seen, the old AF structure remains stable in the whole temperature range in fields up to ~ 8 T. Above this field,

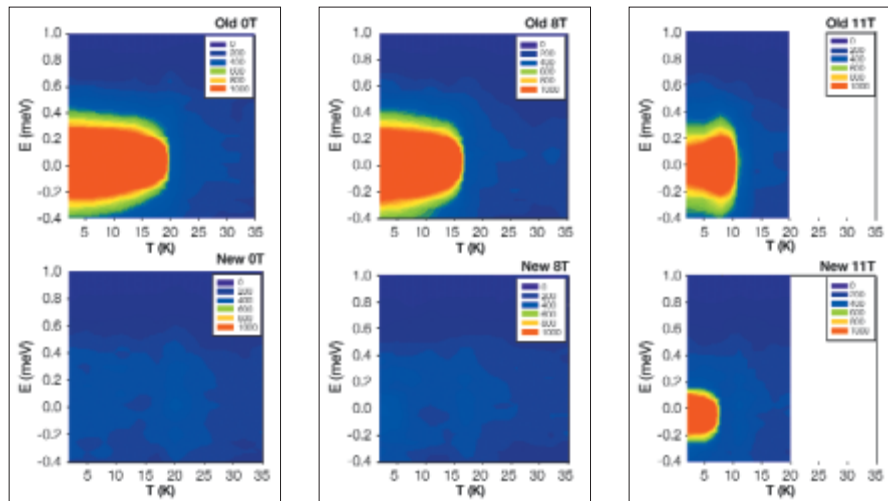


Fig. 3: Quasielastic signal measured on E1 at the old and new magnetic reflections at various applied fields (left – 0T, middle – 8T, right 11 T) upon cooling. Note significant signal around T_N (which decreases with field) and appearance of signal at lower temperatures in fields above 8 T at the new reflection (middle bottom).

the new AF structure begins to compete with the old one and above 11 T it becomes stable. Note the appearance of the “new” reflection at ~ 7 K upon the field of 11 T (about 4 K lower than the “old” reflection appears) and gradual disappearance of the “old” reflection at lower temperatures. This points to slow relaxation phenomena – due to thermal activation. Fact that the old reflection appears at higher temperature than the new one points to the existence of a second-order magnetic phase transition. Interestingly, a field of 11 T corresponds well with the field, above which the magnetic phase transition is of the first order type [2]. A significant intensity around T_N suggests that both AF structures compete even in zero-field around T_N . At the moment it is hard to reconcile the mechanism that is responsible for the change of the AF structure upon application of high magnetic field. One has to recognize that the AF coupling along the hexagonal axis (although in our experiments not parallel to the applied field, in previous experiments with $B//c$ axis the same phenomenon has been observed), the size of U magnetic moments and even the length of the sine-wave modulation within the basal plane remain in both AF structures unchanged. What is affected by the field is *in-plane* coupling direction that merely turns within the hexagonal basal plane and remains perpendicular to the field direction. In Fig. 4 we show the microscopic difference between the old AF structure and the new, established at high fields. In the original AF structure there are two kinds of zigzag chains, one, chain I, consisting only of U atoms, the other one, chain II, having the sequence U-Ni-U-Ni-. Moments in the latter chain are symmetrically not equivalent with those in the former chain. As the field is increased, all the moments become for some reason (a possible mechanism is mentioned below) equivalent and a new exchange path sets in. In the new high-field AF phase, all the

U moments are equivalent forming chain III with a sequence Ni-U-U-U-Ni-U-U-U-. Ab-initio calculations on isostructural compound UNiGa [5] (AF below 40 K) revealed a quite complicated topology of the Fermi surface with six-fold symmetry features in the basal plane that are alternated substantially upon application of magnetic field. At this point, we can only argue that a field driven modifications of the Fermi surface topology are responsible for this unique change of the AF structure in UNiAl. Theoretical ab-initio studies are necessary to elucidate this model.

- [1] K. Prokeš, F. Bourdarot, P. Bulet, P. Javorský, M. Olšovec, V. Sechovský, E. Brück, F.R. deBoer, A. A. Menovsky, Phys. Rev. B **58**, 2692 (1998)
- [2] V. Sechovský, L. Havela, in: *Handbook on Magnetic Materials*, ed. K.H.J. Buschow, (Amsterdam, North-Holland, 1998) Vol. 11, p. 1.
- [3] O. Syshchenko, K. Prokeš, E. Brück, V. Sechovský, Physica B: Condensed Matter, **312–313**, 879–881 (2002) and references therein
- [4] K. Prokeš, P. Javorský, A. Gukasov, E. Brück, V. Sechovský, Physica B: Condensed Matter, **312–313**, 872–874 (2002)
- [5] V.N. Antonov, A. Ya. Perlov, P.M. Oppeneer, A.N. Yaresko, S.V. Hallilov, Phys. Rev. Lett. **77**, 5253–5256 (1996)

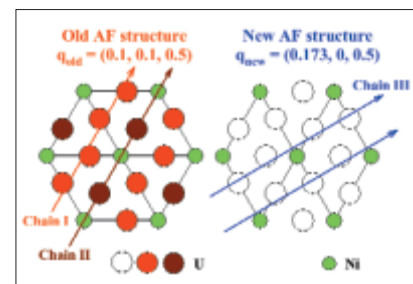


Fig. 4: Schematic representation of the “old” and “new” AF structures (one domain shown) of UNiAl showing different kinds of chains (shown by different shading) containing U ions

Corresponding author:

K. Prokeš
prokes@hmi.de

Metal foams

N. Babcsán^{1,2}, F. García-Moreno², B. Matijasevic², H. Helwig¹, A. Haibel¹, A. Rack¹, J. Banhart^{1,2}

■ 1 HMI, SF3 ■ 2 TU Berlin, Germany



Fig. 1: left: aluminium foam blown with air from a particle-stabilized melt and beer, right: zinc foam and bread roll, both foamed by internal gas creation (Photographs: Hahn-Meitner-Institut)

Introduction

Metal foams are challenging materials for both fundamental and applied research. They distinguish themselves from other materials by low density, high specific stiffness, and high-energy absorption capability. Therefore, they become increasingly popular for industrial applications. Like all other foams, metal foams are produced in the liquid state. Liquid metal foams, by definition, are collections of gas bubbles uniformly dispersed in a liquid metal separated by self-standing thin liquid films. Two methods for foaming metals, distinguished by the way the gas enters the melt, i.e. by the gas source, are used. Bubble creation can be *external* or *internal*. In the former case, gas bubbles are created by continuous gas injection. The foam accumulates at the surface of the melt and the result resembles a glass of draught beer. In the latter method, gas-releasing propellants – akin to the blowing agents of yeast used by bakers – are added to the melt or compacted powders (Fig. 1 and 2).

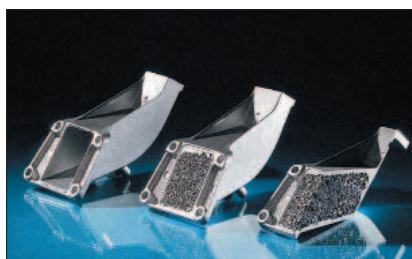


Fig. 2: Foamed part of aluminium dedicated for BMW engine mounting bracket (courtesy of HKB, Austria)

Several scientific challenges and industrial problems of metal foams give motivation for further research. From the scientific point of view, the evolution and the stabilisation of the liquids are in the focus, while industry is searching for process optimization and new metal foaming technology. Our group tries to

work in both the applied and the fundamental fields collaborating with scientists from Japan, Austria, USA and from spin-off companies.

In the following part, we detail the progress in understanding evolution, stability, 3D architecture and microstructure of metal foams. Only very recently, the issue of metal foam stabilisation was addressed and traced back to the presence of micro- or even nanometre-sized solid particles in the liquid metal [1]. The time has therefore come to understand liquid metal foams as an independent field of research and to look at these systems from the viewpoint of colloid chemistry.

Evolution of foams blown by using internal gas source

A compact microfocus X-ray source was used to monitor foam expansion kinetics while the temperature ramp and the TiH_2 blowing agent treatment were varied [2]. A new pressure furnace was built and used to carry out high pressure (<10 bar) and low pressure (>0.001 bar) experiments in oxidizing or inert atmospheres. A strong influence of the gas pressure on the foaming behaviour was found (Fig. 3). Under low pressures, high coalescence, instabilities and rising big bubbles characterise the foaming. Under high pressures, besides a reduced expansion, an extremely small average cell size and high homogeneity were observed. Release from high pressure to normal pressure led to an increased expansion. Also reversible expansion and compression after several pressure cycles were found with a flexible cell wall structure. An additional expansion with high coalescence followed each cycle increasing the maximal expansion from $F/F_0 \sim 1.5$ at 8 bar to $F/F_0 \sim 4$ at 1 bar.

MS, TGA and XRD experiments showed that the decomposition of as-received TiH_2 powder in argon occurs in two stages [3]. Heating as-received TiH_2 at 10 K/min in argon leads to hydrogen release at 400°C. Heat treatment at 480°C for 180 min eliminates the first decomposition stage completely and increases the temperature at which gas evolution occurs. Oxide layers around the cores of the titanium-hydride particles formed during annealing in air act as very effective diffusion barriers. XRD and TEM experiments showed the formation of TiH_2 and Ti_3O during

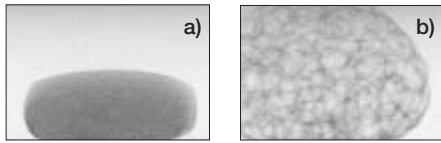


Fig. 3: X-ray radioscapy images of **a)** Al99.7+0.5 wt% TiH₂ foamed under 8 bar in air, **b)** additional expansion of **a)** after release from 8 bar to 1 bar with -0.2 bar/s

heat treatment. We have shown that results from different methods can be combined to form a more complete picture of decomposition of TiH₂ and that various methods provide complementary information.

Evolution of foams blown by external gas injection

External foam evolution strongly depends on the foaming gas being used. The use of an oxidizing gas, e. g. air, results in a thick (100 nm) oxide skin on the cell wall surfaces acting like a rigid stabilizing layer. The role of oxidation in liquid metal foams is revealed by ex-situ and in-situ analysis [4]. A new X-ray transparent foaming furnace was constructed adapting Metcomb technology. The furnace was also used for technology development with our industrial partner. In-situ experiments were performed using microfocus X-ray source at our laboratory at TU Berlin. When blowing Duralcan type metal matrix composites, the drainage and the coalescence rate were quantitatively monitored. Significant drainage was found within the first 20s of foam decay for argon-blown foam. In air-blown foams, drainage was hardly detectable. Isothermal holding leads to coarsening and a slight degradation of uniformity in argon-blown foams (Fig. 4) while air-blown foams remain almost unchanged even after 100 min. During solidification foams shrink significantly in both cases.

3D architecture and microstructure

Synchrotron tomography of aluminium and zinc foams has been carried out at BESSY and evaluated using 3D image analysis. The correlation between the blowing agent's particle position and the pores as well as the critical lamella thickness at different foaming stages were investigated. We obtained various correlations for different alloys, which indicates that the pore formation mechanism depends on the physical properties of the alloy to be foamed. The critical lamella thickness is in the same order of magnitude (20–30 μm) for both aluminium and zinc alloys [5].

Pore-particle correlations in SiC-particle stabilized internal foams were investigated. For the first

time, tomographic measurements of liquid metallic foams were performed. The results of the measurements clarified the rearrangement process of SiC particles during foaming. It could be shown that the accumulation process of the SiC particles on the pore surfaces takes place prevailing in the liquid state due to their partially wetting property. However, the process also continues during the solidification. It seems that due to the solidification front the particles were additionally pushed on the pore surfaces [6].

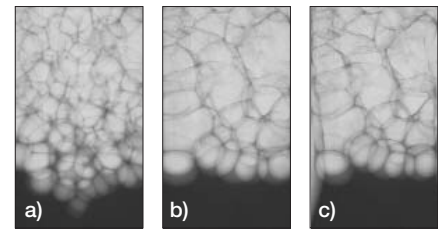


Fig. 4: X-ray radioscapy images of the evolution of argon-blown foam produced by gas injection. **a)** just after foam formation, **b)** at the end of isothermal holding (5 min), **c)** after solidification. Sample widths are 40mm at the bottom.

Future goals

- X-ray tomography with cone beam
- Comparison of foaming behaviour of tixocasted, hot compacted and hot extruded precursor metal powders
- Metallography investigation on single cell walls
- Surface tension measurement of liquid-metal colloids
- Fast radioscapy monitoring coalescence of single liquid-metal films

- [1] J. Banhart, *Manufacturing Routes for Metallic Foams*, Journal of Metals, **52**, 22–27 (2000)
- [2] F. Garcia-Moreno, M. Fromme, J. Banhart, *Real time X-ray radioscapy on metallic foams using a compact micro-focus source*, Adv. Eng. Mat., **6**, 416–420 (2004)
- [3] B. Matijasevic, S. Fiechter, I. Zizak, O. Görke, N. Wanderka, P. Schubert-Bischoff, J. Banhart, *Decomposition behaviour of as-received and oxidised TiH₂ powder*, in: Proc. PM2004 World Congress, Ed.: H. Danninger, R. Ratzl, EPMA, Vol. 4, pp. 149–155
- [4] N. Babcsán, D. Leitmeier, H.-P. Degischer, J. Banhart, *The role of oxidation in blowing particle-stabilised aluminium foams*, Adv. Eng. Mat., **6**, 421–428 (2004)
- [5] A. Rack, A. Haibel, A. Bütow, B. Matijasevic, J. Banhart, *Characterization of metal foams with synchrotron-tomography and 3d image analysis*, 16th World Conference on Non-destructive Testing, Montreal, 30.08.–03.09.2004
- [6] A. Haibel, A. Bütow, A. Rack, J. Banhart, *Quantitative analysis of pore-particle correlations in metallic foams*, 16th World Conference on Non-destructive Testing, Montreal, 30.08.–03.09.2004

Corresponding author:

N. Babcsán
babcsan@hmi.de

Magnetic anisotropy of Ni changed by extreme lattice expansion

Y. Manzhur¹, P. Imielski², K. Potzger¹, W.D. Brewer², M. Dietrich³, M.J. Prandolini^{1,2}, H.H. Bertschat¹

■ 1 HMI, SF4 ■ 2 Institut für Experimentalphysik (WE1), Freie Universität Berlin, Germany ■ 3 Technische Physik, Universität des Saarlandes, Saarbrücken, Germany and The ISOLDE-Collaboration, CERN, Genève, Switzerland

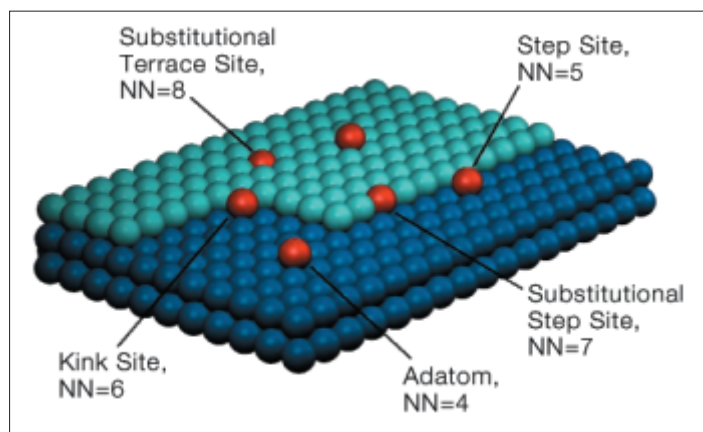


Fig. 1: Idealised surface of a single crystal with (001) orientation, the two shades of blue represent a surface step, radioactive probes are shown in red. All possible regular lattice sites for the impurity atoms as local probes are indicated. The probe atoms can be differentiated by the number of nearest Ni neighbours (NN).

One important new property afforded by ultrathin 2-dimensional magnetic films is perpendicular magnetic anisotropy (PMA). Presently, almost all magnetic recording of digital data uses conventional longitudinal (in-plane) magnetic materials. One method in order to achieve ultrahigh density magnetic recording (in the Tbit/inch² range) is the use of a medium which is magnetized perpendicular to the plane. The aim of this study is to investigate the structure and magnetic anisotropy of ultrathin Ni films, with a bulk lattice parameter of 3.52 Å, grown on Pd(001), with a considerably larger bulk lattice parameter of 3.89 Å. The experiments were conducted using perturbed angular correlation (PAC) spectroscopy in the ultra-high-vacuum (UHV) chamber ASPIC (Apparatus for Surface Physics and Interfaces at CERN).

Ultrathin films of Ni grown on non-magnetic substrates generally have in-plane surface anisotropy [1]. However, the bulk magnetostriction constant λ_{001} for Ni is negative compared to positive values found for Co or Fe. Thus, per-

pendicular magnetism would be possible for ultrathin Ni(001) films, if it would be possible to apply a large enough compressive stress to the film resulting in a negative strain in the [001] direction. This can be achieved *artificially* by growing ultrathin Ni films on non-magnetic substrates with a larger lattice constant and assuming coherent pseudo-morphological growth, as was demonstrated by growing ultrathin Ni films grown on Cu(001) where, however, the lattice mismatch is only 2.5% [2]. In this system, below a critical thickness $d^* = 7$ monolayers (MLs), the ultrathin Ni films were found to be in-plane, where the (in-plane) surface anisotropy dominates for small d , above this critical thickness, the magnetisation was found to be dominated by the magnetoelastic term and therefore is perpendicularly magnetised. Ni grown on Pd(001) is known to grow also pseudo-morphologically, with a lattice expansion of 10.4% up to 6 MLs [3], thus we expect that with greater lattice expansion, the critical thickness d^* at which Ni comes out of the plane would be reduced.

The magnetic alignment of the ultrathin Ni film on Pd(001) was measured with radioactive ^{111m}Cd probe atoms, sitting on the (001) surface, called an “adatom” with 4 next nearest Ni neighbours (NN), see Fig. 1, since the induced magnetism in the Cd atom is expected to be collinear to its next nearest Ni neighbours [4]. All other possible surface sites of a (001) surface are also shown in Fig. 1, the magnetic response of Cd probes sitting at these other sites were measured by previous studies [4].

Radioactive ^{111m}Cd probe atoms are provided by the on-line isotope separator ISOLDE at CERN, see Fig. 2. They are produced by bombarding a liquid Sn target with 1.2 GeV protons. Following mass separation in a magnetic field, they are transferred by a UHV beam-line and are implanted in a catcher-foil in the chamber, ASPIC. The soft-landing of these radioactive probes onto the sample occurs through a two stage resistive heating process.

The sample was prepared by molecular beam epitaxy (MBE) growing 2 atomic monolayers (ML) of Ni on Pd(001) at room temperature. Structure studies showed a coherent pseudomorphological Ni growth, with Ni having an out-of-plane tetragonal distortion, i.e., +10.4% expanded in the plane, and according to a simple linear elastic model, compressed by -13.3% in the out-of-plane [001] direction, as shown in Fig.3. Thereafter, the sample was cooled to 40K and a small amount of radioactive ^{111m}Cd probe atoms were soft-landed onto the surface, and a PAC spectrum was taken of the sample.

At a sample temperature of 40K, there is no diffusion of the Cd atoms across the surface and only one dominant site was found, i.e., adatoms with 4 next nearest Ni neighbours (NN), see Fig. 1. The probe nuclei experienced magnetic hyperfine fields (B_{HF}), resulting in discrete PAC frequencies. The magnitude of the B_{HF} was found to be 30% smaller than for an adatom on a pure Ni surface (7 Tesla) in accordance with theoretical predications. However, important for this measurement, the angle of the magnetic hyperfine field was found to be canted 40° out of the plane. Thus there is a significant change in the magnetic anisotropy for ultrathin Ni films with extreme lattice expansion.

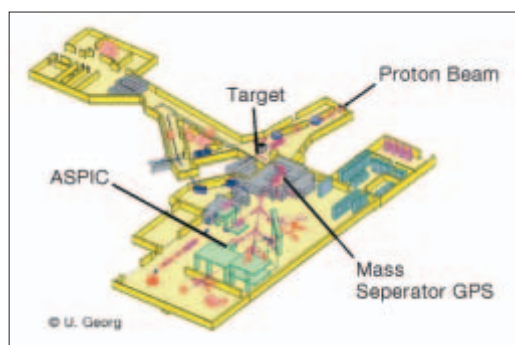


Fig.2: The on-line mass separator ISOLDE at CERN. The ultra-high vacuum (UHV) chamber ASPIC (Apparatus for Surface Physics and Interfaces at CERN) is located in the center of the experimental hall. It is connected to the mass separator by a UHV beam line. (Courtesy of U. Georg, ISOLDE)

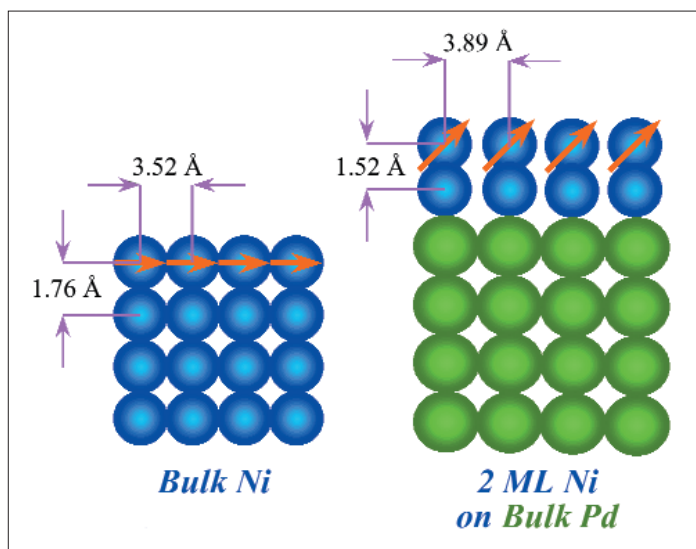


Fig.3: Lattice parameters are shown for a bulk Ni single crystal surface (blue), the Ni surface magnetisation is in the plane, shown by the red arrows (left). However, 2 MLs Ni grown on Pd(001) is lattice expanded in the plane and compressed in the out-of-plane direction, the magnetisation was measured to be canted out of the plane (right).

Since the surface anisotropy scales as $1/d$, 2 MLs of Ni could be expected to be dominated by the in-plane surface anisotropy as was found for Ni on Cu(001), however, Ni, with a lattice expansion of 10.4% on Pd, would have a greatly enhanced magnetoelastic term causing an out-of-plane magnetisation. An estimate for this energy is 1470 kJ/m, which is about 4 times greater than measured for Ni grown on Cu [2]. As a result, this anisotropy dominates, causing a canting even at 2 ML of Ni, as shown in Fig.3.

- [1] W. J. M. de Jonge, P. J. H. Bloemen, F. J. A. den Broeden, in *Ultrathin Magnetic Structures 1*, ed. J. A. C. Bland and B. Heinrich (Springer, Berlin, 1994) Chap 2.3.
- [2] B. Schulz, K. Baberschke, *Phys. Rev. B* **50**, 13467 (1994)
- [3] G. A. Rizzi, M. Petukhov, M. Sambri, G. Granozzi, *Surf. Sci.* **522**, 1 (2003)
- [4] K. Potzger A. Weber, H. H. Bertschat, W.-D. Zeitz, M. Dietrich, *Phys. Rev. Lett.* **88**, 247201 (2002)

Texture modification in nanocrystalline materials using swift heavy ions

I. Zizak¹, N. Darowski¹, G. Schumacher¹, S. Klaumünzer¹, W. Assmann², J. Gerlach³

■ 1 HMI, SF4 ■ 2 Ludwig-Maximilians-University Munich, Germany ■ 3 Leibniz-Institute for Surface Modification, Leipzig, Germany

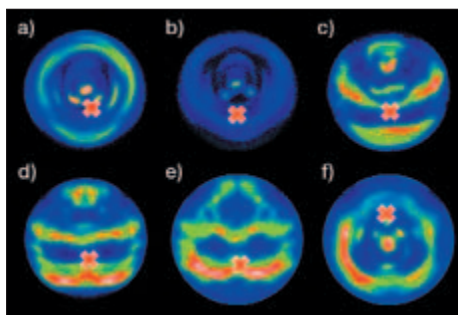


Fig. 1: Orientation distribution (texture) of the (101) planes in α -Ti layer after irradiation with different fluences.

a–e) In unirradiated sample the pattern is symmetrical around the normal to the sample surface. During irradiation with 350 MeV ions with different fluences we observe two changes: (I) the pattern moves upwards, (II) the ring structure disappears. The direction of the ion beam is marked with the red 'X'. The applied fluences are **a)** 1×10^{14} , **b)** 3×10^{14} , **c)** 7×10^{14} , **d)** 12×10^{14} , and **e)** 18×10^{14} ions/cm². **f)** If we take the sample irradiated with 7×10^{14} ions/cm² (**d**) and irradiate it with the same fluence in the opposite direction, the ring structure moves back. This means that the original texture was restored.

Introduction

In order to optimize the surface properties of materials for different applications without changing their bulk properties, one often coats them with thin layers of other materials. Physical vapour deposition (PVD) is a standard method used to produce thin polycrystalline layers. The size and the orientation of the grains created in this process depend on many process parameters, such as the deposition rate or the substrate temperature. When materials are deposited in micrometer thick layers, the grains have often sizes of 10–100 nm. Usually, the grains are not randomly oriented. Since different

lattice planes have different surface energies, during growth, the energetically favoured lattice plane is selected to be parallel to the surface. When there are no reasons for in-plane alignment, the orientation distribution of lattice-plane normals, denoted as texture, is symmetrical around the surface normal (fibre texture).

The material properties relevant for applications are strongly influenced by the layer texture. Mechanical properties, like wearing, depend on the packing density of the plane parallel to the surface as different lattice planes have different packing densities. Since the work needed to emit an electron depends on the surface properties, the electrical and, specially, the electro-optical properties are influenced as well.

The lattice plane preferred during the deposition need not be the best choice for applications. In the last few years, large effort was made to influence the orientation of the grains in deposited layers. One of the most promising methods is the ion beam assisted deposition (IBAD), where layers are irradiated with low-energy ions during deposition. The direction of the ion beam introduces a second preferred axis in the energy of the deposited layer leading to a crystallite orientation-distribution different from the unirradiated case.

Recently, we measured a change in orientation of the grains in nanocrystalline vapour-deposited Titanium (Ti) layers after irradiation with high-energy heavy ions. Swift heavy ions deposit their energy in solids mainly through electronic interaction. Since collisions with solid nuclei are unlikely at high energies, ions travel through the solid on straight paths. The energy deposited by the ion is concentrated in a volume a few nanometers around the ion path.

Experiment

In our experiment, polycrystalline layers were irradiated with 350 MeV gold ions with different fluences of up to 10^{15} ions/cm². We studied systematically titanium and titanium nitride, varying the layer thickness, grain size, and crystal structure of the sample. The titanium crystal structures

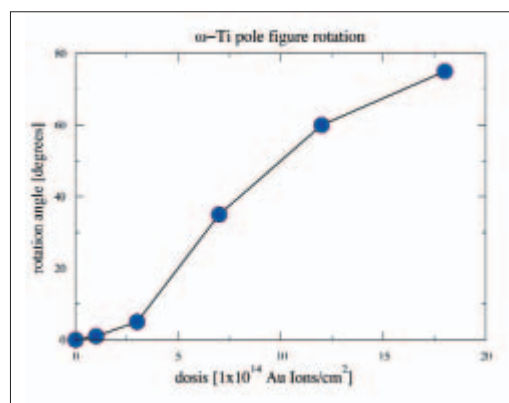


Fig. 2: Dependence of the angle of the grain rotation on the fluence

studied were in the hcp phase, which is stable under normal conditions (α -Ti), and in the complex hexagonal high-pressure phase, which is also created during irradiation (ω -Ti). TiN has the bcc crystalline structure, which is the same as the structure of rock salt.

Since a very high flux of high-energy ions was needed, the samples were irradiated at the Hahn-Meitner-Institut ion accelerator ISL. Different directions of the impinging ion beam were used.

The textures were determined at Hahn-Meitner-Institut's 6-circle diffractometer at the KMC2 bending magnet beamline at the Berlin synchrotron light facility BESSY. A combination of an area-sensitive detector and an intense synchrotron beam allowed for a very fast acquisition of the complete orientation distribution in the sample.

Results

In our experiment, layers with different compositions showed apparently different kinds of behaviour. In coarse-grained materials, no changes in the orientation distribution were observed. In different nanocrystalline materials, the orientation changed in different ways. In α -Ti, the rotational symmetry around the surface normal disappeared, and the grains aligned with one preferred axis towards the ion beam [1]; in ω -Ti the texture continuously rotated away from the ion beam. In TiN layers both effects were observed simultaneously.

Although the correlation between the crystalline axes and the impinging ion beam direction (as in α -Ti) might point at the interaction between crystalline grains and the ions, it is hard to imagine that the force, which rotates the grains by 70° with an almost constant rate, depends on the crystal symmetry. A possible explanation might be the interaction between the ion beam and isotropic material in the sample. In poly-crystalline materials, the grain boundary, which is supposed to be amorphous, is a few nanometres thick. If the grains are of the size of 10–100 nm, a large part of the material is in the grain boundaries, i. e. amorphous.

Indeed, there is a well-known effect, referred to as 'ion hammering' [2, 3], which describes anisotropic dilation of amorphous materials during ion irradiation. Due to the cylindrical shape of the volume where the energy is deposited, the material is plastically lengthened in the direction normal to the ion path and shortened in the direction parallel to it. When the amorphous layer fixed on the substrate is bombarded with swift heavy ions from a direction other than normal, the dilatation is transformed into shearing of the layer away from the direction of the incoming beam.

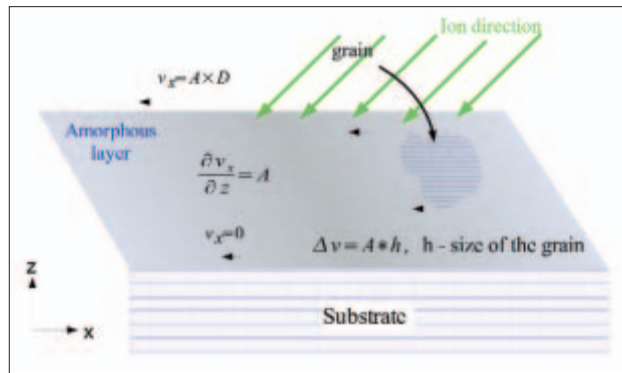


Fig. 3: Simple model for the grain rotation in amorphous matrix. Due to the geometry of the ion track, the amorphous layer is plastically sheared. A crystalline grain built into this matrix would have to rotate.

Since the grain boundary is interconnected through the whole material, we expected the nanocrystalline layer to behave like an amorphous one with crystalline grains embedded into it. As a simple model we can assume that the grain size is small compared to the distance between grains. The shearing of the amorphous layer would then produce a rotational moment on grains, and they would rotate away from the ion beam direction, as it was measured. In real nanocrystalline materials, the grains are still much larger than the grain boundary thickness, and there is an interaction between the grains. This is the reason why in some materials (e.g. α -Ti) the rotation around the surface normal takes place. Grains tend to behave like in our model, but since they are too close to each other, they jam and are not able to rotate further. They can unhook only if they rotate in other directions until the contact surfaces are parallel. Due to the energy balance, the surfaces of small grains are mostly low indexed planes, so the aligning of surfaces in grains implies also the aligning of the crystalline axes. In our measurements, this aligning is seen as breaking of the fibre texture. The actual rate of the alignment and rotation depends on the form and size of the grains.

- [1] I. Zizak, N. Darowski, G. Schumacher, S. Klau-münzer, W. Assmann, J. Gerlach, *Modification of the Ti Texture using swift heavy ions*, Hahn-Meitner-Institut Annual Report 2003
- [2] S. Klau-münzer, *Plastic flow of amorphous materials induced by swift heavy ions*, Mater. Sci. For. **97–99**, 623 (1992)
- [3] H. Trinkaus, A.I. Ryazanov, *Viscoelastic model for the plastic flow of amorphous solids under energetic ion bombardment*, J. Nucl. Mater. **246**, 244 (1997)

Corresponding author:

I. Zizak
zizak@hmi.de

Electronic energy-density effects in Auger angular distributions

G. Schiwietz¹, F. Staufienbiel¹, M. Roth¹, K. Czernski¹, P.L. Grande²

■ 1 HMI, SF4 ■ 2 Instituto de Física, Universidade Federal do Rio Grande do Sul, Porto Alegre, Brazil

In this work, we report on a new effect related to the extremely dense energy deposition of heavy ions at velocities around 10% the speed of light. In contrast to individual photons or electrons, swift heavy ions can transfer energies of several hundred eV per target atom into the electronic system of the target [1]. In fact the power deposition by a single highly charged ion is comparable to a focused multiphoton pulse of the future free electron x-ray laser XFEL that will be installed at DESY/Hamburg.

As has been shown in previous papers [1], complete ionization of all light atoms along the ion track as well as electron temperatures of about 100 000 K result from the penetration of an individual ion. Thus, locally there is extremely strong excitation accompanied by the breaking of all bonds inside a nanometer radius around the long and straight ion path. Subsequently the electronic motion is coupled to the atomic degrees of freedom (see Fig. 1) and materials modification via high-temperature or high-pressure phases may result.

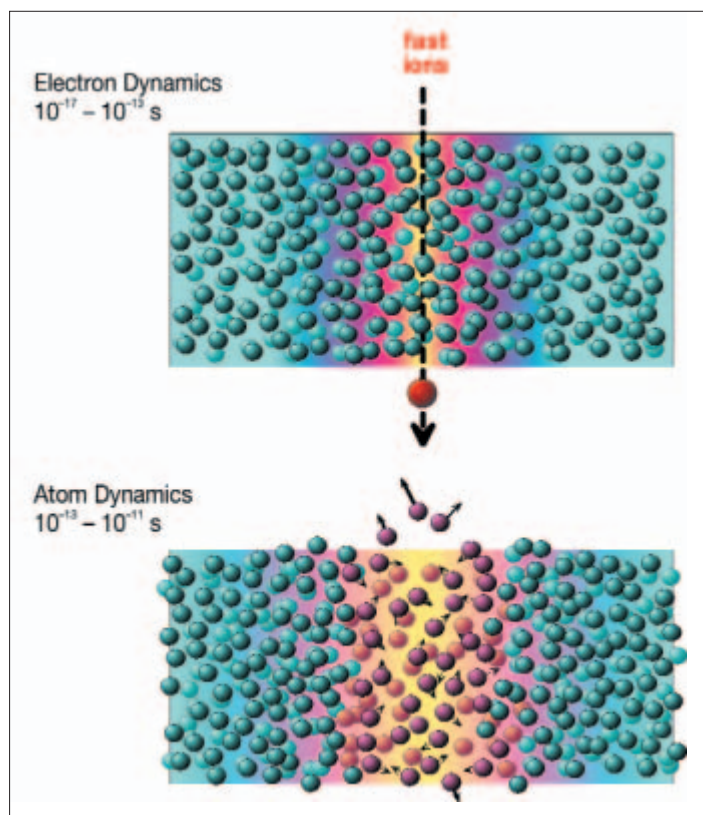


Fig. 1: Time evolution of an ion track after the penetration of a swift heavy ion (red ball with arrow). First the electronic system is heated up (color coding in the upper drawing) and afterwards the energy is transferred to the atomic system (lower drawing).

Most of the qualitative and quantitative results on electronic short time energy-density effects in ion tracks are deduced from high-resolution Auger-electron spectra corresponding to Auger-decay times of 1–10 fs. Under specific conditions inner-shell vacancies decay via (one-electron) x-ray transitions. In most cases, however, the production of Auger electrons (via two-electron transitions) is more likely. Their peak energy contains information on the ionization degree and on collective electrostatic potentials [2]. Their peak width may contain information about the populated density of states in the valence/conduction bands [3]. If a local thermal equilibrium is reached before the Auger decay, it is even possible to extract electron temperatures from the peak width. The high electron temperatures should also have an influence on the angular distribution of emitted Auger electrons, since the electron transport to the surface should be affected. The only setup at any high-energy accelerator that is sophisticated enough for such a study is the one installed at ISL (devices 1, 4, 5, and 7 in Fig. 2 are needed for this purpose).

Here we present the first angular Auger-electron distribution induced by swift heavy ions. Experiments have been performed with 592 MeV Au^{48+} ions at normal incidence on atomically clean beryllium (Be) and aluminum (Al) surfaces. For Be the so-called K^nVV Auger decay and for Al the L^nVV Auger yield as function of the emission angle has been investigated. In the latter case, a vacancy in an n -fold ionized L shell is filled by one valence electron

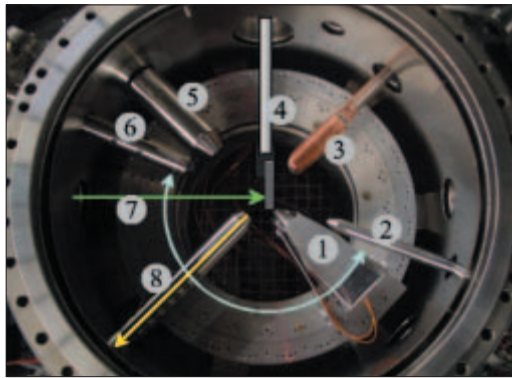


Fig. 2: Top view of the ultra-high vacuum setup with double magnetic shielding.

1) Hahn-Meitner-Institut made rotating (light blue arrows) electrostatic electron spectrometer, **2)** UV source, **3)** x-ray source, **4)** target manipulator, **5)** electron gun, **6)** low-energy Ar sputter gun, **7)** heavy-ion beam from the ISL cyclotron (green arrow), **8)** retractable (yellow arrow) secondary-ion mass-spectrometer

(**V**) and another valence electron (**V**) is being ejected. Conservation of the total electronic energy determines the Auger-electron energy. The corresponding L^iVV Auger-intensities have been measured for $n=1, 2$, and 3 . It is emphasized that such different Auger-decay channels are related to different decay times and reflect specific snapshots of the time evolution of ion tracks in solids [1]. The intensity ratios $R_2 = I(L^2VV)/I(L^1VV)$ and $R_3 = I(L^3VV)/I(L^1VV)$ (displayed as red and blue symbols in Fig. 3) will thus be sensitive to the time evolution of the ion track. Experimental uncertainties, electron diffraction or refraction effects are canceled to a large extent when calculating ratios. Previous investigations [4] have revealed cosine-like angular distributions, very similar for various targets and different types of transition. Using this information, the ratios R_2 and R_3 are expected to be constant to within a few percent.

A closer look at Fig. 3 shows that the ratios are not constant at all, with a significant minimum at ejection angles around 180° with respect to the initial beam direction (we have also observed a similar behavior for the Be target). The above discussion points to a time-dependent effect. In fact, the electron temperatures increase from about 20 000 K for L^1VV to about 50 000 K for L^3VV transitions mainly due to the mean Auger decay time which is reduced from 1.5×10^{-14} s for L^1VV to 0.5×10^{-14} s for L^3VV . Thus, the ratio R_3 is related to very high electron temperatures (50 000 K) as is estimated from the shape of the Auger line (see refs. [3]).

Furthermore, emitted electrons at angles close to 180° are moving for an extended period of time along the hot ion track. Hence, the pronounced minimum in Fig. 3 for exactly this case points to a preferential absorption of Auger electrons inside a hot electron gas. Such an effect has never been observed before. It is expected to have an influence on laser-induced plasmas as well, but it is easier to investigate this effect with spatially confined energy depositions as they are typical for ion-solid interactions.

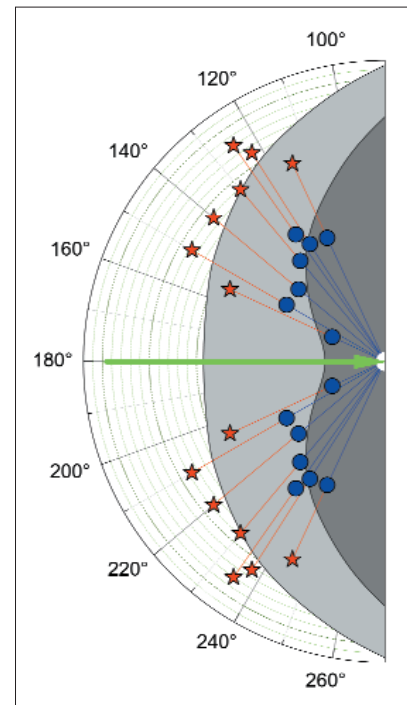


Fig. 3: Angular distribution of Auger-intensity ratios (in polar coordinates) for L^2VV to L^1VV (red asterisks) as well as for L^3VV to L^1VV (blue circles) line intensities from atomically clean Al surfaces. The green arrow indicates the incident direction of the 592 MeV Au^{48+} projectile ions.

- [1] G. Schiwietz, M. Roth, K. Czerski, F. Staufenbiel, P.L. Grande, *Femtosecond Dynamics – Snapshots of the Early Ion-Track Evolution*, Nucl. Instr. Meth. B **225**, 4–26 (2004)
- [2] G. Schiwietz, P.L. Grande, B. Skogvall, J. P. Biersack, R. Köhrbrück, K. Sommer, A. Schmoldt, P. Goppelt, I. Kádár, S. Ricz, U. Stettner, *Influence of Nuclear Track Potentials in Insulators on the Emission of Target Auger Electrons*, Phys. Rev. Lett. **69**, 628–631 (1992); G. Xiao, G. Schiwietz, P.L. Grande, N. Stolterfoht, A. Schmoldt, M. Grether, R. Köhrbrück, A. Spieler, U. Stettner, *Indications of Nuclear-Track-Guided Electrons Induced by Fast Heavy Ions in Insulators*, Phys. Rev. Lett. **79**, 1821–1824 (1997)
- [3] G. Schiwietz, G. Xiao, P.L. Grande, E. Luderer, R. Pazirandeh, U. Stettner, *Determination of the electron temperature in the thermal spike of amorphous carbon*, Europhys. Lett. **47**, 384–390 (1999); F. Staufenbiel, G. Schiwietz, K. Czerski, M. Roth, and P.L. Grande, *Electronic energy-density effects in ion tracks of metals*, Nucl. Instr. Meth. B (in print)
- [4] W.S.M. Werner, H. Tratnik, J. Brenner, H. Störi, *Surface Science* **495**, 107–119 (2001)

Corresponding author:

G. Schiwietz
schiwietz@hmi.de

Melting of orientational order of colloidal molecular crystals on a triangular lattice

A. Šarlah, T. Franosch, E. Frey

■ HMI, SF5

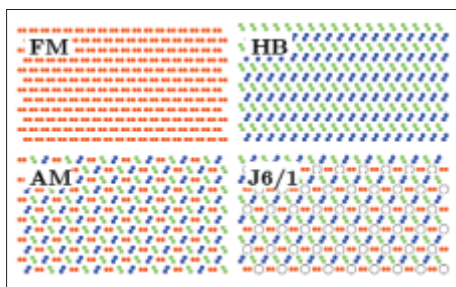


Fig. 1: Schematic representation of ordered ground states of the colloidal dimer Hamiltonian. The orientations of dimers are colour-coded. The energy of the J6/1 structure is degenerate with respect to the dimer orientation on the sites denoted by circles.

Soft condensed matter and, in particular, systems of colloidal particles can serve as versatile model systems to study phenomena of condensed matter physics. The main advantage of colloidal systems lies in the fact that the characteristic time- and length-scales allow monitoring individual particles by widely accessible methods, such as light scattering or video microscopy. Lately, research in the field of colloids has focused on two-dimensional (2D) systems, especially, on 2D colloidal systems subject to 2D periodic potentials. In experiments, the periodic patterns are mostly produced by light sources: either by arrays of laser traps or by an interference pattern of coherent laser beams. These systems are ideal to mimic the adsorption of atoms or molecules on atomic surfaces, vortices in superconductors with periodic pinning arrays, and other related phenomena studied extensively in condensed matter physics.

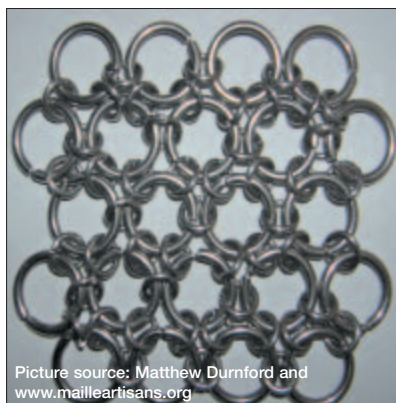


Fig. 2: The Japanese 6 in 1 chainmaille. Note the resemblance with the J6/1 structure of Fig. 1.

Our theoretical study has been motivated by a recent work of Brunner and Bechinger [1] who have studied the ordering and melting phenomena of 2D colloidal systems on a triangular lattice. The lattice was produced by the interference of three coherent laser beams, which allowed for a continuous variation of both the lattice constant and the strength of the laser potential. Adjusting the lattice constant and density of colloidal particles makes it possible

to realize incommensurate and commensurate situations. For now, the experimental and theoretical/computational studies [2, 3] are restricted to commensurate cases, where the number of colloidal particles is an integer multiple of the number of potential minima.

In the experiment [1], the number of colloidal particles per potential minimum was adjusted to three and the phase behaviour on increasing the strength of the external potential has been investigated. The researchers found that even at rather low light intensities the colloids tend to localize in groups of three particles at the potential minima. Upon increasing the potential strength, the number of defects, i. e., groups of two or four particles per lattice site, is observed to decrease rapidly. They become completely unobservable already for moderate intensities. Then the groups of particles on each site form nearly equilateral triangles and can be regarded as composite objects referred to as trimers. The remaining energy excitations are the orientation of the trimers with respect to the lattice direction. Due to the interaction of the trimers, long-range orientational order can be expected for sufficiently strong coupling. This can indeed be observed once the defect-free regime takes over. Interestingly, the same authors have also observed a loss of orientational long-range order at even higher laser intensities, which was interpreted as re-entrant melting.

In our study, we have derived analytically phase diagrams for commensurate systems of dimers and trimers on triangular lattices in high external fields. There, one can assume that the translational order is fully determined by the underlying lattice and the only degrees of freedom correspond to the orientations of defect-free composite objects. The analytical study has been supplemented by Monte Carlo simulations.

Our key idea is to reduce the problem to the low energy degrees of freedom by considering composite objects as being rigid. This can be done because of the separation of energy scales, i. e., the binding energy of an isolated composite object (the sum of the internal colloid-

colloid potential energy and the compression due to the external laser potential) is orders of magnitude above the thermal energy. The symmetry of the lattice and the number of constituent particles account for the shape of the composite object and its size is such that it minimizes the binding energy. The nearest-neighbour interaction lifts the otherwise degenerate orientational states, the characteristic energy scale being the thermal one. Since the colloid-colloid repulsion is typically strongly screened, the interaction between the next-nearest-neighbour composite objects can be neglected. The rising laser intensity squeezes the constituents of composite objects closer together, thus reducing the nearest-neighbour interaction. This is the mechanism driving the orientational melting at high laser intensities.

Since the triangular lattice is induced by the interference of three laser beams, the lattice sites exhibit a six-fold symmetry. This symmetry yields an effective potential, which has three minima corresponding to equivalent ground states for an isolated symmetric dimer and two for an isolated symmetric trimer. If short-time orientational fluctuations close to the potential minima are considered to be already averaged out, one is left with only a discrete set of gross orientations. Then the problem reduces to the statistical mechanics problem of a system with a finite number of discrete *spin* states at each lattice site. The characteristics of the system are hidden in the effective pair-wise interactions between *spins* in different relative orientational states.

An isolated trimer on a triangular lattice has two discrete orientational states and a pair of trimers can be in one of four configurational states, two of which are equivalent. The resulting two energy differences imply a generalization of the Ising system. However, due to the symmetry of the lattice, the problem reduces to the pure 2D Ising model, which has been solved analytically long ago. Considering this solution and determining the effective interaction energies in the sense explained above, we have determined the critical laser intensity, above which the orientational order melts. The results are in accordance with the experimental observations. It should be noted that our model has no fit parameters.

The case of dimers on a triangular lattice is much richer. A single dimer has three discrete states and a pair of dimers nine configurational states, which fall into one of four different classes. This implies a Hamiltonian with three relevant energy scales. Again, the interplay of

the symmetry of lattice and orientations of dimer states reduces the number of parameters by one, leading to a generalized 3-state Potts model. This model has four different ordered phases: ferromagnetic (FM), antiferromagnetic (AM), herringbone (HB), and Japanese 6 in 1 (J6/1), see Fig. 1. We have borrowed the name for the latter from the weaving patterns for chainmailles, see Fig. 2, worn by samurai in the 14th century. The first two ordered phases occur also in the case of a pure Potts model, though, in a certain parameter range the FM to P (paramagnetic) transition is discontinuous because it is driven by the non-Potts term. The HB structure is the one most relevant for colloidal systems. However, it is not restricted to colloidal systems. In the 1980's, a similar structure has been identified as the ground state of N₂ molecules adsorbed on graphite [4]. The theoretical description within a continuous anisotropic planar rotor model yielded critical behaviour comparable to the one obtained with our discrete analogue. At that time there was also some experimental evidence for structures having similar symmetry as our J6/1 structure. The complete phase diagram of the colloidal dimer Hamiltonian is presented in Fig. 3.

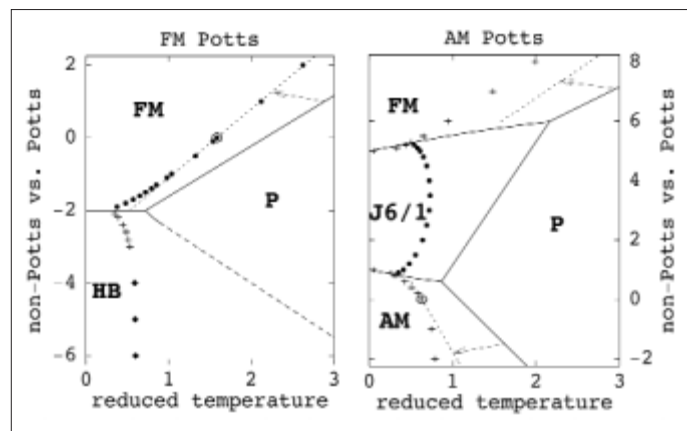


Fig. 3: Phase diagram for the dimers on a triangular lattice. The areas corresponding to structures with different symmetries (denoted by their respective names) are separated by phase boundaries obtained either within the MF description (lines) or Monte Carlo simulations (symbols).

- [1] M. Brunner, C. Bechinger, Phys. Rev. Lett. **88**, 248302 (2002)
- [2] C. Reichhardt, C.J. Olson, Phys. Rev. Lett. **88**, 248301 (2002)
- [3] A. Šarlah, T. Franosch, E. Frey, submitted to Phys. Rev. Lett. (2005)
- [4] O.G. Mouritsen, A.J. Berlinsky, Phys. Rev. Lett. **48**, 181 (1982)

Corresponding author:

A. Šarlah
andreja.sarlah@mf.uni-lj.si

Force transduction in stiff polymers

O. Hallatschek, E. Frey, K. Kroy

■ HMI, SF5

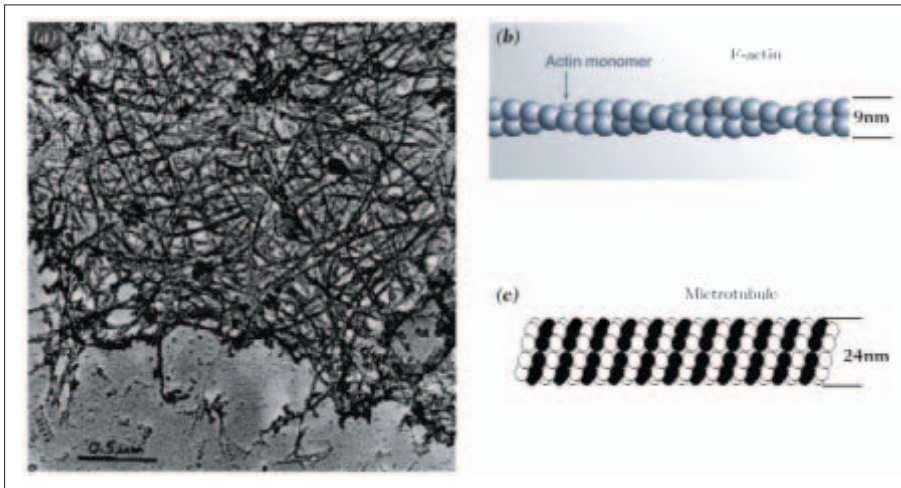


Fig. 1: In vitro networks of purified F-actin, such as the one shown in the electron micrograph **a)**, serve as model systems for studying the mechanical properties of the cytoskeleton. The cytoskeleton is a dense network mainly consisting of F-actin **b)** and microtubules **c)**. [Part **a)** courtesy of Erich Sackmann; part **b)** adapted from Ref [1]; part **c)** courtesy of Erwin Frey]

This work is motivated by the intriguing properties of a special class of biopolymers, which can be found in eukaryotic cells. It is by now well established through numerous experiments in vitro and in vivo that the extraordinary mechanical and dynamical properties of cells are to a large extent determined by a three-dimensional assembly of protein fibers, the cytoskeleton. Its structural elements are a number of relatively stiff biopolymers (actin filaments, microtubules and intermediate filaments) and proteins that crosslink them to form bundles or networks (see Fig. 1a) for a F-actin network). Microscopically, these biopolymers are linear assemblies of globular subunits. For example, actin is a twisted double-strand of beaded subunits, the globular actin, which is illustrated in Fig. 1b). It is a common feature of all cytoskeletal filaments that the molecular architecture provides them with a nearly *inextensible* backbone and a high *bending rigidity*. This is particularly evident for microtubules, which are hollow cylinders typically formed by thirteen tubulin protofilaments assembled in parallel, see Fig. 1c). As a consequence, microtubules have an enormous bending stiffness comparable to carbon nanotubes.

For the analysis of the mechanical response of biological tissues to external forces it is crucial to understand how forces (statically and dynamically) percolate through the interior of a single cell. To tackle this problem, the complexity of the cell interior may be reduced to the cytoskeleton (immersed in a viscous liquid), which is, due to its stiffness, the cell component most efficient in transmitting forces. This idealized model system exhibits complex rheological properties that can be studied in vitro. It has therefore gained considerable attention during the last decade among physicists interested in soft matter and biology.

We studied theoretically the problem of mechanical force transduction along single stiff polymers [2] – the links of a cytoskeletal network. This question arises, for example, when a stiff polymer is pulled longitudinally at the ends, see Fig. 2. In the case of an inextensible rigid rod the whole rod would be set into motion instantaneously. A thermally excited polymer, instead, will generally exhibit self-affine contour undulations and the tension has to pull these undulations (against the longitudinal friction) in order to set (a part of) the polymer into motion – just as is the case for a wiggled thread that is suddenly pulled at both ends. This stretching of the polymer occurs within a finite region close to the boundary where the force is applied.

The size $l_H(t)$ of this region increases with time until it eventually spans the entire polymer. As long as this boundary layer does not extend over the whole filament the other end will not be affected. The growth laws for the boundary layer determine how fast mechanical signals propagate through the filament.

Previous theoretical studies are mainly semi-phenomenological and give a rather incoherent picture. Markedly different growth laws have been predicted for weak [3–5] and strong [4, 6] forces, respectively. The precise meaning of “strong” and “weak” and the validity of the various assumptions in [4, 6] are not immediately obvious, such that many questions are left unanswered.

We have for the first time developed from first principles description [2, 7] of non equilibrium propagation and relaxation of the tension in stiff polymers. This theory not only recovers all cases (correctly) studied in the literature so far and identifies the range of their validity (see Fig.3). It also allows us to systematically extend these previous results and to derive the longitudinal nonlinear response to various external perturbations (such as mechanical excitations, hydrodynamic flows, electrical fields, temperature quenches etc.) that can be represented as sudden changes of ambient/boundary conditions. Due to their biological implications, we expect our results to be tested in future experiments.

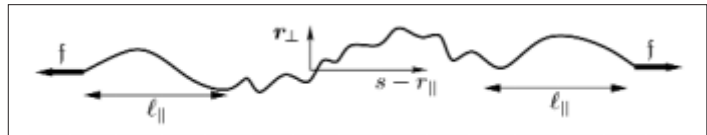


Fig. 2: Schematic illustration of a scenario involving tension propagation: In response to an external force f , the thermally undulated contour is straightened within boundary layers of growing width $l_{||}(t)$.

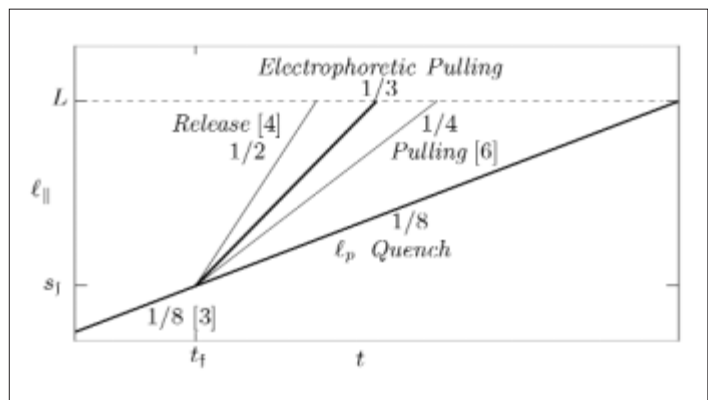


Fig. 3: Double-logarithmic sketch of the tension propagation laws $l_{||}(t) \propto t^z$. At a force dependent time t_f they cross over from a universal short-time regime to (problem-specific) tension-dominated intermediate regimes. The propagation ends when the tension has spread over the whole filament, $l_{||}(t) \approx L$.

- [1] R. Götte, K. Kroy, E. Frey, M. Bärmann, E. Sackmann, *Macromolecules*, 29:30, (1996)
- [2] O. Hallatschek, E. Frey, K. Kroy; *Phys. Rev. Lett.* **94**, 77804 (2005)
- [3] R. Everaers *et al.*, *Phys. Rev. Lett.* **82**, 3717 (1999)
- [4] F. Brochard-Wyart, A. Buguin, P. G. de Gennes, *Europhys. Lett.* **47**, 171 (1999)
- [5] V. Shankar, M. Pasquali, D. C. Morse, *J. Rheol.* **46**, 1111 (2002)
- [6] U. Seifert, W. Wintz, P. Nelson, *Phys. Rev. Lett.* **77**, 5389 (1996)
- [7] O. Hallatschek, E. Frey, K. Kroy, *Phys. Rev. E* **70**, 031802 (2004)

Synchrotron light helps to elucidate the role of metalloproteins in health and disease

M. Kühbacher, A. Kyriakopoulos, D. Behne

■ HMI, SF6

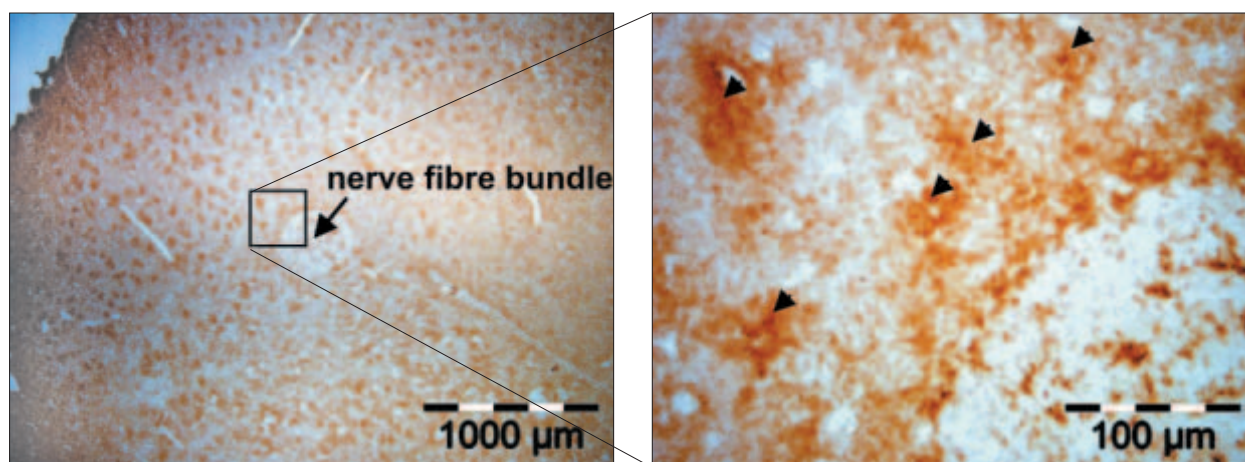


Fig. 1: Immunolabeling of the prion protein in a BSE-infected hamster brain section. The metal load of the aggregations of this metalloprotein (arrows) can be investigated by SRXRF.

Most of the metals and metalloids present in the mammalian organisms are bound to proteins. These metalloproteins play a central role as structural or catalytic components, and their identification and the elucidation of their distribution and biological functions are therefore of great interest in various fields of the life sciences. Synchrotron radiation X-ray fluorescence analysis (SRXRF) allows the determination of the metal distribution in cryosections of tissues while synchrotron radiation-based Fourier transform infrared (SRFTIR) spectromicroscopy may provide information on the chemical composition of the sections of interest. These methods can therefore be used as valuable tools in studies on the role of metalloproteins in health and disease. Their application in this field of research is subject of our work at the IRIS Beamline at BESSY and the SRXRF beamline of HASYLAB. In both cases the use of synchrotron radiation offers the high spatial resolution necessary in the investigation of thin tissue sections.

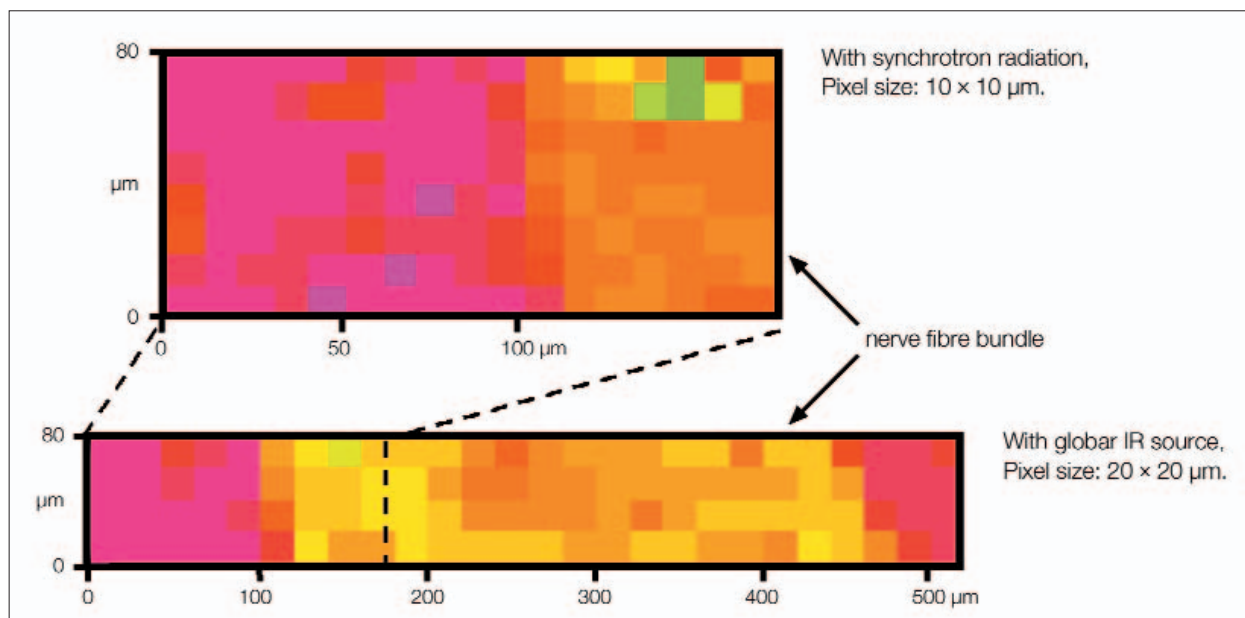


Fig. 2: Colour-coded lipid-to-protein ratio determined by SRFTIR-spectro-microscopy in a hamster brain section with a lipid-rich nerve fibre bundle as shown in Fig. 1. The example illustrates the higher spatial resolution achieved by synchrotron as compared with that obtained by a global IR source.

There is evidence that metals and metalloids such as copper, manganese, zinc and selenium are involved in the etiology of Transmissible Spongiform Encephalopathies (TSEs). TSEs such as Scrapie in sheep, Bovine Spongiform Encephalopathy (BSE) in cattle, or Creutzfeldt-Jakob disease in man are infectious neurodegenerative disorders of the central nervous system. TSEs are associated with the conformational change and the aggregation of a specific protein. This *prion protein*, found in nerve and glial cells throughout the brain, was shown to bind copper, zinc, and manganese, and changes in the binding of these metals may play a role in the pathogenesis of TSEs. Our studies on the role of metalloproteins in these diseases therefore include investigations of changes in the elemental distribution in the brain carried out by SRXRF as well as the measurement of structural changes of specific proteins by means of SRFTIR-spectro-microscopy at the IRIS-Beamline at BESSY.

The localization of metal-containing proteins in histological tissue sections was achieved at the SRXRF beamline of HASYLAB by means of a capillary optical device focusing the X-ray beam with a spatial resolution of $15\ \mu\text{m}$. Brain samples were obtained from hamsters which had been infected with different TSE strains. The tissue samples were provided by M. Beekes and A. Thomzig from the Robert-Koch-Institut, Berlin. The measurements included the determination of the distribution of phosphorus, sulfur, chlorine, potassium, calcium, iron, copper and zinc and the immuno-histochemical detection of the prion protein. The most important finding so far was the detection of unusual copper hot-spots with a mean diameter of about $30\ \mu\text{m}$ which were found in the brain sections of all hamsters infected with TSE.

Corresponding author:
M. Kühbacher
kuehbacher@hmi.de

25 years of the magnetic spectrometer Q3D

H. G. Bohlen, W. von Oertzen

■ HMI, SF7

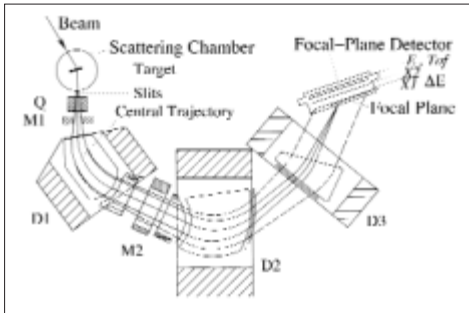


Fig. 1: Magnetic Spectrometer Q3D

Magnetic spectrometers for the measurement of high resolution energy spectra of charged particles are among the most powerful instruments in nuclear physics and other fields of heavy ion research. Q3D spectrometers consisting of a quadrupole Q, three dipoles (D1–D3) and other magnetic multipole elements (M1, M2) (see Fig. 1) combine a large solid angle with the best resolution in the range down to $\delta E/E \approx 2 \times 10^{-4}$. The spectrometer Q3D at the ISL accelerator facility of the Hahn-Meitner-Institut has now been in operation for 25 years. In combination with the high quality ion beams from the ISL cyclotron and with modern detector technology in the focal plane including advanced data acquisition systems, it offers unique possibilities for reaction studies in the energy range of 5–30 MeV/u. In the past years 19 Diploma and 15 PhD theses (100 publications) have been accomplished at this instrument [1].

We give here a short description of the spectrometer and an overview of the main physics subjects in this period. The layout of the magnetic elements is depicted in Fig. 1. The quadrupole Q produces a vertical cross at M2 in order to increase the vertical angular acceptance ($\pm 3^\circ$). All the focusing in the horizontal plane is achieved by the boundaries of the dipoles. The kinematical momentum variation within the horizontal angular acceptance of $\pm 3^\circ$ is corrected by the multipole M2 using the variable quadrupole component. The detector system in the focal plane allows measuring the position of ions (needed for the momentum analysis of the reaction products), their energy loss, their rest energy and the flight-time, which depends on the path through the spectrometer. The latter dependence also allows one to determine the scattering angle for identified isotopes with a resolution of 0.3° . For example, in the rainbow scattering of $^{16}\text{O} + ^{16}\text{O}$ (Fig.3) pieces of angular distributions with a width of 10° in the centre of mass were measured with this resolution. In other cases,

the difference in the angular variation of kinematical lines observed for different target masses can be used to separate reactions on contaminants in the target (typically ^{12}C and ^{16}O). The examples given below show the potential for experiments with heavy ions.

Measurement of spin alignment using the Doppler-Effect in particle spectra

An example of the high resolution capability of the spectrometer is the measurement of the energy shifts $\Delta E = \pm(v/c) \times E_\gamma$ of reaction products with γ -decay in flight (v speed of the ion, E_γ decay energy). The angular distribution of the γ -rays, which depends on the spin alignment and

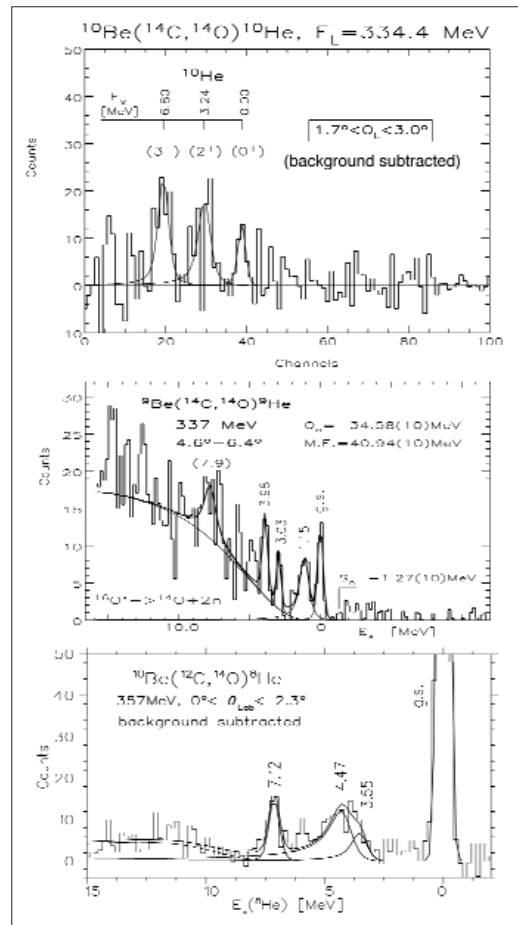


Fig. 2: Spectra of the extremely neutron-rich helium isotopes ^{10}He (upper panel), ^9He (centre panel) and ^8He (lower panel)

on the multi-polarity of the γ -transition, is reflected in a specific shape of the broadened energy distribution. The latter is used to deduce the spin alignment, which is a very important parameter in the understanding of nuclear reactions [2].

Measurements of ground state masses and energy spectra of very exotic nuclei

The Q3D spectrometer allows the measurement of reaction products in multi-nucleon transfer reactions with very small cross sections. In addition it is possible, with a corresponding calibration, to determine the mass of exotic nuclei and their excited states, which may be particle-stable or unstable. Also the measured decay width can be analyzed, which allows to deduce spectroscopic information on the orbital angular momentum and the spin of the states. An example of these studies is the determination of the level structure of the helium isotopes ^8He , ^9He and ^{10}He as shown in Fig. 2. The mass of ^{10}He , which has the largest neutron-to-proton ratio of all known nuclei, was determined [3] and several excited states of the three isotopes have been measured [3, 4]. The ^{10}He ground state resonance has a measured width of only 0.3(2) MeV. This can be understood from the fact that a direct decay of $^{10}\text{He} \rightarrow (n + ^9\text{He})$ is not possible, and the three particle channel $(n + n + ^8\text{He})$ with a much more restricted phase space is the only direct decay mode. Similarly, the energy levels of the highly exotic isotopes ^{10}Li and ^{11}Li have been measured [4]. For both nuclei, ^{11}Li and ^{10}He , the binding is achieved by a special quantum mechanical structure of the three body systems $(n + n + ^9\text{Li})$ and $(n + n + ^8\text{He})$. The wave functions of the neutrons have a very large extension beyond the range of nuclear forces, a phenomenon referred to as "Halo"-structure. Another highly appreciated subject, which has been the domain of Q3D experiments, is the establishment of covalently bound nuclear two- and three-centre systems. These are nuclear dimers in Be-isotopes and nuclear polymers as linear chains in excited states of ^{13}C and ^{14}C nuclei [5]. Examples of these unique results are given in the next contribution.

Nuclear rainbow scattering

The enhancement of cross sections at large scattering angles, which can occur for refractive scattering due to the *rainbow effect*, has been demonstrated for the first time for heavy ions with measurements at the Q3D spectrometer of the Hahn-Meitner-Institut [6]. The rainbow scattering produces an intensity maximum at the *rainbow angle*. The structure is described by Airy-functions. After the discovery [6] of this effect in the $^{16}\text{O} + ^{16}\text{O}$ system at an incident ener-

gy of $E_L = 350$ MeV, the group at the Hahn-Meitner-Institut has pursued a programme to measure the energy systematics [7] (the highest energies at the spectrometer SPEG at GANIL). Figure 3 shows the evolution of the refractive rainbow structure as function of energy, here expressed by the de-Broglie wavelength of the ^{16}O particles. The effect can be expressed by a refractive index, which is determined by the strongly attractive nucleus-nucleus potential.

Energy loss of ions in extremely thin layers

The energy loss of ions in matter is well understood in charge-state equilibrium conditions, i. e. in thick materials. However, for high resolution elastic recoil detection analysis (ERDA), where thicknesses range down to a few nanometres, the analysis relies on calculations of the energy loss of the incoming ion. With the method developed at the Hahn-Meitner Institute [8] the whole matrix of values for energy losses in very thin carbon foils in dependence on both the incoming and the outgoing charge states has been obtained for ^{18}O , ^{22}Ne and ^{40}Ar ions [8]. These values will also serve to calibrate the calculations of energy losses of ions penetrating hot and dense plasmas.

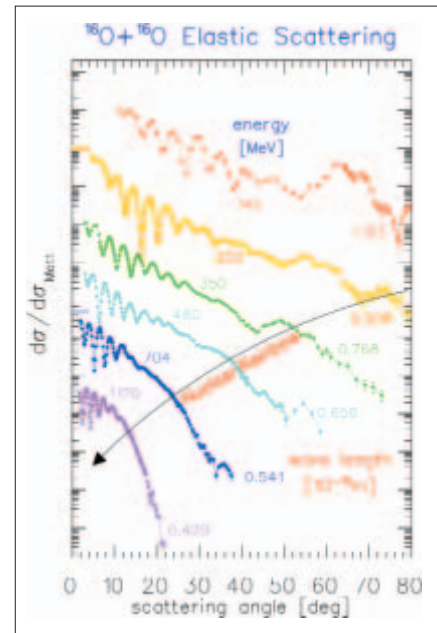


Fig. 3: Data of elastic scattering of $^{16}\text{O} + ^{16}\text{O}$ at different incident energies as indicated at the data. The effect of nuclear rainbow scattering is observed at large scattering angles.

- [1] <http://www.hmi.de/bereiche/SF/SF7/q3d.html>
- [2] H. G. Bohlen, *et al.*, Z. Phys. A **285**, 371 (1978)
- [3] A. N. Ostrowski, *et al.*, Phys. Lett. B **338**, 13 (1994)
- [4] H. G. Bohlen, *et al.*, Nucl. Phys A **583**, 775 (1995)
- [5] W. von Oertzen, *et al.*, Eur. Phys. J. A **21**, 193 (2004)
- [6] E. Stiliaris, *et al.*, Phys. Lett. B **223**, 291 (1989)
- [7] D. T. Khoa, *et al.*, Nucl. Phys. A **672**, 387 (2000)
- [8] A. Blazevic, *et al.*, NIM B **190**, 64 (2002)

Corresponding author:

H. G. Bohlen
bohlen@hmi.de

Chain states in ^{13}C and ^{14}C , nuclear polymers

W. von Oertzen, H. G. Bohlen

■ HMI, SF7

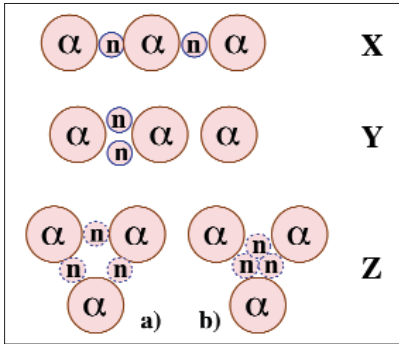


Fig. 1: Molecular configurations in ^{14}C : three α -particles with valence neutrons. Linear chains with different sharing of the neutrons: **X)** the symmetric configuration; **Y)** intrinsically reflection-asymmetric. Oblate shapes (**Z)** with two ways of sharing the valence particles.

Recent studies [1–2] of excited states in light nuclei show that the binding between clusters due to the exchange of valence neutrons results in covalently bound molecules. We have studied the cluster structure of beryllium isotopes ^9Be – ^{12}Be and more recently we have identified the molecular cluster structure of excited states in ^{13}C and ^{14}C . Inspecting the available data compilations and using the selectivity of various multi-nucleon transfer reactions, we apply the concept of *complete spectroscopy* and identify the states with single particle structure, and those states with clustering, the latter are expected to form rotational bands. These cluster states in ^{13}C and ^{14}C consist of three α -particles and are stabilised by the covalent valence neutrons. Chain states with very large deformation (hyper-deformation) are identified. Due to their intrinsically reflection asymmetric shapes the rotational bands are observed as parity (inversion) doublets, as described by Herzberg [4] for atomic molecules. After a detailed study of dimers, the covalently bound states of two α -particles [1–3] in the beryllium isotopes, the covalent bond between three α -particles can be modelled with the Hueckel-method for three centres as described for ^{13}C in ref. [5]. In the nuclear case the three centre system can have different geometrical arrangements. In ^{14}C for example the different cluster configurations to be expected are:

- a) Linear reflection-symmetric chains corresponding to a configuration with the valence particles equally distributed among the three basis centres (α -n- α -n- α), labelled as the *X-configuration* in Fig.1. For the valence particles of the lowest chain state, the $K=3/2$ band with orbitals build from the π -bonds between two α -particles, the density distri-

butions will be concentrated outside the symmetry axis. The most stable isomeric nuclear three centre molecule is expected to be observed in ^{16}C , with the linear structure chain (α -2n- α -2n- α), the study of such states is the aim of our future investigations.

- b) Linear intrinsically reflection *asymmetric* configurations corresponding to the structure α -2n- α - α with the two valence neutrons in the covalent π -bond between two centres. In this case with a α -2n- α substructure as in ^{10}Be (g.s.), which has a large pairing energy, we obtain the *Y-configuration* in Fig.1. Therefore close to the threshold for ($^{10}\text{Be} + \alpha$) at 12.012 MeV we expect two rotational bands as parity inversion doublet [6] of this structure.
- c) The oblate configurations will be represented by a triangular structure (also shown in Fig.1) as discussed in refs. [5, 6]. In this case the π -bonds would penetrate the α -particles and it is expected that the σ -bonds dominate.

In the approach of complete spectroscopy applied to ^{13}C we had previously singled out those states for which strong evidence for α -cluster structure is available [5]. These states are shown in a diagram in Fig.2, and the states can be grouped into two rotational bands with $K=3/2$, a parity doublet as expected for an asymmetric linear chain, the bands start close to the ($^9\text{Be} + \alpha$)-threshold.

Rotat. bands, K^π	$\hbar^2/2\theta$ (keV)	Configuration
^{13}C , $3/2^-_2, 3/2^+_3$	190	chain {5}
^{14}C , $0^+_2, 3^-_2$	230, 280	oblate {6}
^{14}C , $0^+_3, 1^-_2$	120, 130	chain {6}

Table 1: Properties of the rotational bands of ^{13}C and ^{14}C with 3α -chain or triangle (oblate) configurations. The bands are characterized by the spin-parity K^π of the band head. Moments of inertia are given as $\hbar^2/2\theta$.

Oblate and prolate chain states in ^{14}C

We have recently successfully identified the chain states in ^{14}C as the next important step in the establishment of the structure of nuclear polymers [6]. In order to identify the cluster states in ^{14}C , using the concept of *complete spectroscopy* as in the case of ^{13}C [5], we have first identified the single particle and two-neutron-configurations in ^{14}C .

The structure of the remaining states with cluster configuration is characterized by their different population through the selectivity in many different multi-nucleon transfer reactions studied with 3D-Spectrometers. In some of these reactions states with multi-particle multi-hole configurations, involving in particular also proton excitations, become dominant. The states, which are identified as cluster states are strongly deformed, they form rotational bands with extreme deformations. Some of these states, as mentioned before, will have intrinsically reflection-asymmetric shapes. The parity projection produces in this case two bands and these are grouped into parity doublets with band-heads below the energies of the relevant thresholds corresponding to asymptotically asymmetric fragmentations.

We summarize the result for the strongly deformed cluster bands in $^{13-14}\text{C}$ in Fig. 3, by plotting the excitation energies of the states as function of $J(J+1)$, where J is the angular momentum. We notice that the slope parameter $\hbar^2/2\theta$ for the prolate ^{14}C chain states are smaller (due to larger moments of inertia) than for ^{13}C .

From these data on the rotational bands we can derive moments of inertia θ , expressed by the volume of $\hbar^2/2\theta$ listed in Table 1, and we can compare these values with those obtained for strongly deformed cluster bands in other light systems. From this result we can deduce, that the bands identified as chain states in the carbon isotopes are indeed cases of linear chain states.

Work in part supported by the German Federal Ministry of Education and Research under contract Nr. 06-OB-900.

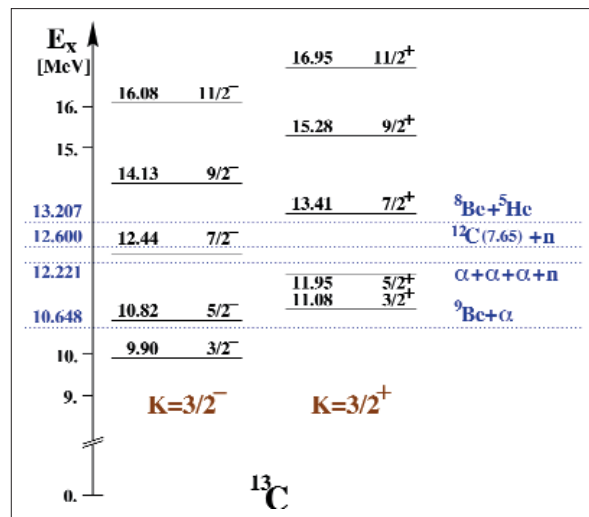


Fig. 2: Energy levels of ^{13}C grouped into rotational bands (parity doublets), the K -quantum numbers is indicated. The threshold energies for structure components related to the asymptotic cluster-structure of states are shown (from ref. [5]).

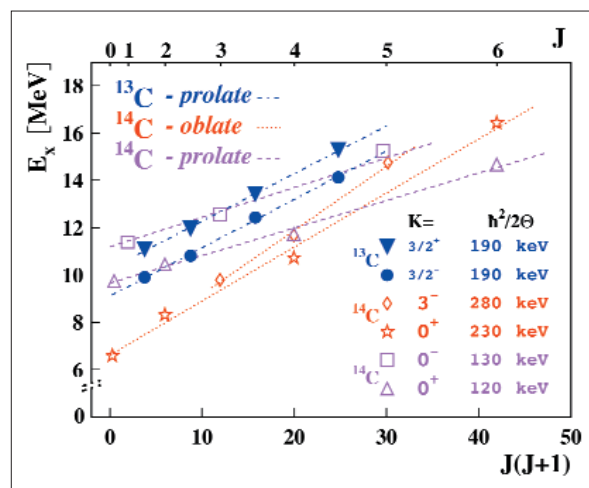


Fig. 3: Summary of strongly deformed cluster bands in $^{13-14}\text{C}$. Excitation energies are shown as function of $J(J+1)$, K -quantum numbers of the different bands are indicated. The moments of inertia expressed as $(\hbar^2/2\theta)$ indicate that the states are extremely deformed ("hyperdeformation").

1. W. von Oertzen, Prog. Theor. Physics (Japan), Suppl. No **146**, 169 (2002)
2. H. G. Bohlen *et al.*, Prog. Part. Nucl. Phys. **42**, 17 (1999)
3. W. von Oertzen, H. G. Bohlen, C. R. Physique **4**, 465 (2003)

4. G. Herzberg, *Spectra of Diatomic Molecules*, van Nostrand, Inc., Princeton (1964)
5. M. Milin, W. von Oertzen, Eur. Phys. J. A **14**, 295 (2002)
6. W. von Oertzen, H. G. Bohlen, M. Milin *et al.*, Eur. Phys. J. A **21**, 193 (2004)

Corresponding author:

W. von Oertzen
oertzen@hmi.de



Surface analysis in ultra-high vacuum

A person wearing a white lab coat is shown from the chest up, holding a long, thin metal rod. The rod is inserted into a piece of scientific equipment on the left side of the frame. The person's hands are positioned to adjust or manipulate the equipment. The background is a bright, slightly blurred white surface, possibly a cleanroom or laboratory setting. The overall scene suggests a technical or scientific environment.

Scientific highlights Solar Energy Research 2004

SE1, Silicon Photovoltaics	78
SE2, Heterogeneous Material Systems	84
SE3, Technology	90
SE4, Dynamics of Interfacial Reactions	96
SE5, Solar Energetics	102
SE6, Electronic Structure of Semiconductor Interfaces	108

Laser-induced self-organization in Si-Ge alloys

M. Weizman, N. H. Nickel, I. Sieber

■ HMI, SE1

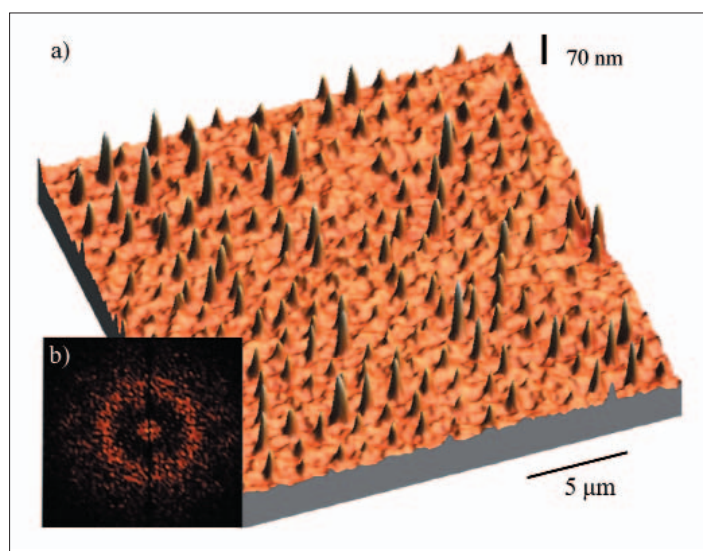


Fig. 1: Surface morphology of laser crystallized poly-SiGe
a) Atomic force microscopy (AFM) micrograph
b) Power spectrum of a two-dimensional Fourier analysis of the sample surface

In nature spatial self-organization is a wide spread phenomenon that leads to stunning patterns and structures that can be observed for example in snow flakes and ripples on the beach and sand dunes. Previously, scientists have succeeded to achieve controlled self-organization on much shorter length scales to create novel one- and two-dimensional structures for a new generation of opto-electronic devices. Numerous methods such as solution growth [1, 2], laser-assisted catalytic growth [3], dc sputtering [4], and molecular beam epitaxy [5, 6] have been developed to fabricate self-organized structures. However, all fabrication methods hitherto used are time consuming and require rather high temperatures.

We discovered a laser-induced self-organization of germanium rich dots in silicon-germanium alloys on an ultra short time scale of 100 ns. In addition, the employed method is a low-temperature process where the substrate is held at room temperature.

The silicon-germanium (SiGe) alloys were prepared by the following procedure. At first hydrogenated amorphous silicon-germanium (a-SiGe:H) layers were deposited on quartz substrates by glow-discharge decomposition of silane and germane gas mixtures. Then, the specimens were crystallized employing a XeCl excimer laser operating at a wavelength of 308 nm with a pulse width of about 20 ns. Complete melting and solidification of the samples occurs within about 100 ns. The crystallization experiments were performed at room temperature and in vacuum. The energy distribution of the laser beam was homogenized over an area of $6 \times 6 \text{ mm}^2$ using a fly's eye homogenizer. Since the a-SiGe:H thin-films contained a hydrogen concentration of up to 13 at.% a step-by-step crystallization technique was applied to avoid ablation of the a-SiGe:H layers. Figure 1a shows an atomic force microscopy (AFM) scan of a poly-Si_{0.55}Ge_{0.45} sample that was crystallized with a final laser fluence of $E_L = 650 \text{ mJ/cm}^2$. While the surface of the amorphous SiGe alloy was smooth the AFM micrograph reveals a quite unusual surface structure of the laser-crystallized specimen. The entire surface is covered with small spikes of a height between 50 and 120 nm. These spikes are not limited to a specific area of the crystallized specimen but occur over the entire surface of the poly-SiGe thin film. The surface micrograph indicates that the distance between spikes is unique. This was verified by applying a two-dimensional Fourier analysis to the AFM micrograph. The resulting power spectrum for the poly-SiGe sample is shown in Fig. 1b. In the reciprocal space a circle with a diameter of $\approx 1.7 \mu\text{m}^{-1}$ is obtained that corresponds to a mean distance, d , between spikes of about 1.2 μm .

The composition of the laser crystallized alloys was investigated using energy dispersive X-rays (EDX). The relative Si and Ge signals were calibrated with a single crystal SiGe standard of known composition. Special care was taken to avoid contributions to the silicon signal from the quartz substrate. The amorphous starting material contained a homogeneous Ge concentration of 33%. Laser crystallization caused a significant change of the composition of the polycrystalline specimens. Figure 2a shows an SEM micrograph of the surface of a laser crystallized poly-SiGe sample that was analyzed along the indicated red line using EDX. The white spots represent the laser-induced spikes. The measured Ge content is plotted in Fig. 3b. Surprisingly, the Ge concentration exhibits a sinusoidal variation along the indicated line and varies significantly from the initial 33% of the amorphous starting material. The highest Ge concentration of $\approx 47\%$ is observed at the spikes (white areas in Fig. 3a). In between the self-organized spikes the Ge concentration decreases to values as low as 27%. This result clearly demonstrates that excimer laser crystallization causes a significant lateral variation of the alloy composition.

The governing mechanism of ultra fast self-organization of SiGe alloys is related to the heating and cooling rates and the presence of germanium. Alloying silicon with germanium has a significant impact on the melting point of the alloy. With increasing Ge content the melting point decreases from 1414°C for pure silicon to 940°C for pure germanium. Melting and solidification during excimer laser crystallization occurs far from thermodynamic equilibrium. In fact, the heating and cooling rates are on the order of 10^{10} K/s. When the entire thin film is melted the liquid SiGe becomes super cooled and subsequently homogeneous nucleation sets in. For pure silicon films with a thickness of 40 nm a nucleation temperature as low as 1130°C was reported [7]. At this time the composition of the SiGe alloy changes abruptly over the entire liquefied area and regions with a lower Ge content than the amorphous starting material and spikes with a high Ge content form. Because of the high cooling rate Ge diffusion into the Ge-depleted regions does not occur.

The self-organization of the spikes occurs because of volume changes of the silicon-germanium alloy during solidification. After nucleation lateral grain growth occurs and the Ge-rich spikes are the last to freeze. Since the liquid material has a higher density than the solid

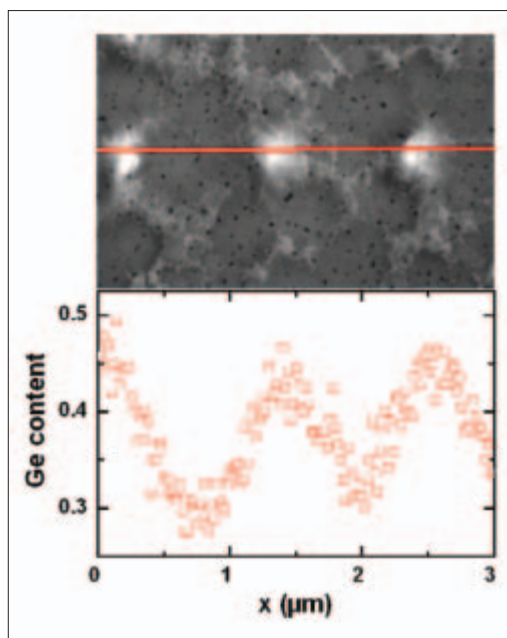


Fig. 2: EDX line scan. **a)** Surface micrograph of laser crystallized poly-SiGe. The composition of the laser crystallized SiGe alloy was measured along the indicated red line. **b)** Germanium concentration along the line indicated in **a)**

alloy the growing grains fill a larger volume than the melt they consume. Eventually when the space between grains becomes small the remaining liquid extends above the surrounding layer forming the observed Ge-rich spikes.

- [1] J. D. Holmes, K. P. Johnston, R. C. Doty, B. A. Korgel, *Science* **287**, 1471 (2000)
- [2] Z. Tang, N. A. Kotov, M. Giersig, *Science* **297**, 237 (2002)
- [3] A. M. Morales, C. M. Lieber, *Science* **279**, 208 (1988)
- [4] Y. Zhu, G. S. Cheng, L. D. Zhang, *J. Mat. Science Lett.* **17**, 1897 (1998)
- [5] J. A. Floro, E. Chason, M. B. Sinclair, L. B. Freund, G. A. Lucadamo, *Appl. Phys. Lett.* **73**, 951 (1998)
- [6] C. Teichert, M. G. Lagally, L. J. Peticolas, J. C. Bean, J. Tersoff, *Phys. Rev. B* **53**, 16334 (1996)
- [7] C. P. Grigoropoulos, S.-J. Moon, M.-H. Lee, in *Laser crystallization of silicon*, Ed. N. H. Nickel, (Elsevier – Academic Press, San Diego, 2003), Vol. 75, Chp. 2

Corresponding author:
M. Weizman
weizman@hmi.de

Numerical simulation of thin-film heterojunction solar cells: open-source program AFORS-HET, version 1.2

R. Stangl¹, M. Kriegel¹, A. Froitzheim³, K. v. Maydell¹, S. Kirste¹, L. Korte¹, T. Brammer⁴, H. Stiebig², M. Schmidt¹
 ■ 1 HMI, SE1 ■ 2 Photovoltaik-Institut, Forschungszentrum Jülich, Germany ■ 3 present address: Shell-Solar GmbH, München, Germany ■ 4 present address: Q-Cells AG, Thalheim, Germany
 general contact: AFORS-HET@hmi.de

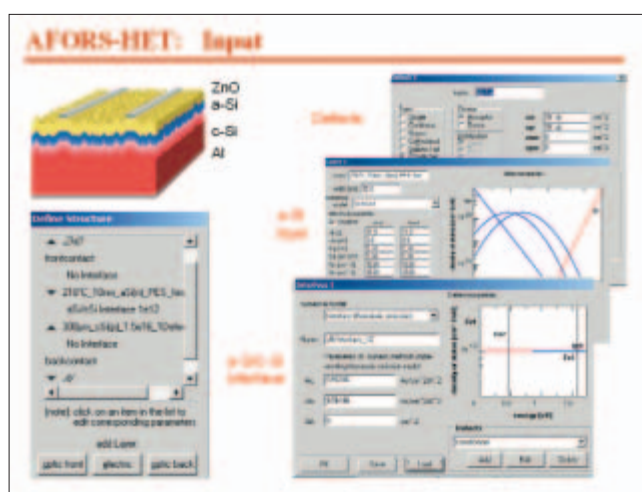


Fig. 1: Screenshots of typical AFORS-HET input: Simulation of TCO/a-Si:H(n)/c-Si(p)/Al heterojunction solar cells. (left) layer sequence, (right) density of states of the a-Si:H(n) layer and of the a-Si:H(n)/c-Si(p) interface

We developed a numerical computer simulation program, AFORS-HET, suitable for modelling thin film heterojunction solar cells and the observable of various characterization techniques. It is distributed free of charge via the web site: www.hmi.de/bereiche/SE/SE1/projects/aSiSi/AFORS-HET

In order to investigate thin film heterojunction solar cells, a variety of different experimental methods are used, ranging from standard solar cell characterization techniques, like current-voltage (I-V) or quantum efficiency (EQE, IQE) to more advanced characterization techniques, like surface photovoltage (SPV), photo- or electroluminescence (PL, EL), capacitance-voltage (C-V), capacitance-temperature (C-T), impedance (IMP), intensity modulated photocurrent spectroscopy (IMPS) or electrically detected magnetic resonance (EDMR). In order to support the interpretation of such measurements, a numerical simulation

tool, **AFORS-HET**, (automat for simulation of hetero-structures) has been designed. AFORS-HET not only simulates (thin film) heterojunction solar cells, but also the observable of the corresponding characterization techniques. A user-friendly graphical interface allows the visualization, storage and comparison of all simulation data. Furthermore, arbitrary parameter variations and parameter fits to measurements can be performed.

An arbitrary sequence of semiconducting layers can be modelled, specifying the layer and, if needed, interface properties, i.e., the defect distribution of states (DOS). Using Shockley-Read-Hall recombination statistics, the one-dimensional semiconductor equations are solved for thermal equilibrium, various steady-state conditions and for small additional sinusoidal modulations. Additional or modified characterization techniques as well as new numerical modules can be implemented by external users (open-source on demand). Up to now, the following numerical modules have been realized: (a) The front contact can be treated either as a metal/semiconductor contact (Schottky contact) or as a metal/insulator/semiconductor contact (MIS contact). (b) The transport across each semiconductor/semiconductor interface can be modelled either by drift-diffusion currents or by thermionic emission. (c) The optical generation rate can be calculated taking into account coherent and incoherent multiple reflections.

Up to now, we use AFORS-HET mainly to simulate amorphous/crystalline silicon heterojunction solar cells of the structure TCO/a-Si:H(n)/a-Si:H(i)/c-Si(p)/a-Si:H(p⁺)/Al. These solar cells are processed by depositing 5 nm ultra-thin layers of amorphous hydrogenated silicon, a-Si:H, on top of a 300 μm thick crystalline silicon wafer, c-Si. In order to achieve solar cell performance with efficiencies greater than 17%, interface recombination has to be sur-

pressed. Thus, interface sensitive characterization techniques are needed. The corresponding simulations help to interpret the measurements and to compare their sensitivity to the a-Si:H/c-Si interface state density.

Before the calculation, an appropriate sequence of semiconducting layers and interfaces has to be stated (see Fig. 1). For the shown example, the corresponding semiconductor properties, namely the a-Si:H(n) thin-film emitter and the c-Si(p) silicon wafer, must be defined. Additionally, the defect density of states (DOS) has to be specified for all layers and, if needed, for the interfaces.

In order to specify the DOS for the thin-film a-Si:H layers, we use photoelectron yield spectroscopy with UV light excitation (UV-PEYS). With this method the position of the Fermi energy, the density of occupied states in the band gap and the valence band close to the band edge can be measured [1]. As an example, the measured defect distribution of occupied states for a nominal intrinsic and an n-doped a-Si:H layer is shown in Fig. 2. The measured slope of the valence band tail (Urbach energy) and the measured occupied dangling bond distribution are used as direct input parameters in AFORS-HET (compare Fig. 1). However, the Urbach energy of the conduction band tail has to be guessed.

A general interface model assumes a constant DOS of the a-Si:H/c-Si interface with a donor/acceptor behavior in the lower/upper part of the a-Si:H bandgap, respectively (compare Fig. 1). Using AFORS-HET, the sensitivity of various characterization techniques to the a-Si:H/c-Si interface state density can be studied numerically, see Fig. 3, and compared or even fitted to experimental results.

Up to now, approximately 120 AFORS-HET downloads have been recorded, and three updated versions have been published [2]. The program has been used by various groups within the a-Si:H/c-Si community [3–5], mainly in order (1) to evaluate maximum obtainable efficiencies for amorphous/crystalline heterojunction solar cells, (2) to derive design criteria for those solar cells and (3) to develop measurement methods for monitoring the a-Si:H/c-Si interface recombination.

- [1] M. Schmidt, A. Schoepke, L. Korte, O. Milch, W. Fuhs, *The gap state density distribution in extremely thin a-Si:H layers on crystalline silicon wafers*, J. Non-Cryst. Solids **338–340**, 211 (2004)
- [2] R. Stangl, M. Kriegel, K. v. Maydell, L. Korte, M. Schmidt, W. Fuhs, *AFORS-HET, an open source on demand numerical PC program for simulation of (thin film) heterojunction solar cells*, Version 1.2, Proc. IEEE-31, 31th IEEE Photovoltaics Specialists Conference, Lake Buena Vista, USA, January 2005, to be published
- [3] A.S. Gudovskikh, J.P. Kleider, R. Stangl, M. Schmidt, W. Fuhs, *Interface properties of a-Si:H/c-Si heterojunctions investigated by admittance spectroscopy*, Proc. 19th PVSEC, Paris, France, June 2004, 697
- [4] R. Stangl, D. Schaffarzik, A. Laades, K. Kliefoth, M. Schmidt, W. Fuhs, *Characterization of interfaces in amorphous/crystalline silicon heterojunction solar cells by surface photovoltage spectroscopy*, Proc. 19th PVSEC, Paris, France, June 2004, 686
- [5] M. Taguchi, H. Sakata, Y. Yoshimine, E. Maruyama, A. Terakawa, M. Tanaka, *An approach for the higher efficiency in the HIT cells*, Proc. IEEE-31, 31th IEEE Photovoltaics Specialists Conference, Lake Buena Vista, USA, January 2005, to be published

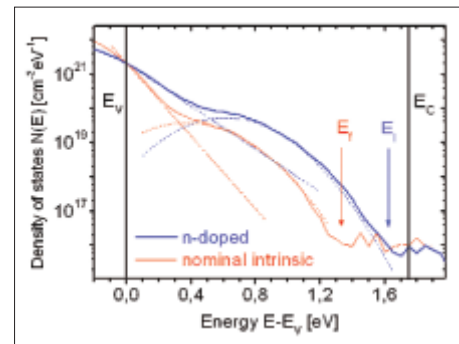


Fig. 2: Measured photoelectron yield spectroscopy data for nominal intrinsic and n-doped a-Si:H. The results are used to specify the density of states within the thin amorphous silicon layers.

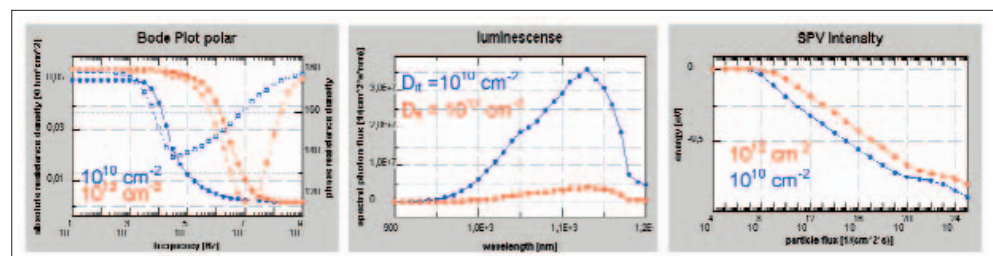


Fig. 3: Screenshots of typical AFORS-HET Output: Open-circuit Impedance (left), Photo-luminescence (middle) and illumination intensity dependend Surface Photovoltage (right), simulated for a-Si(n)/c-Si(p) solar cell structures, assuming two different a-Si/c-Si interface state densities $D_{it} = 10^{10} \text{ cm}^{-2}$ and 10^{12} cm^{-2} .

Corresponding author:

R. Stangl
stangl@hmi.de

Low-temperature Si epitaxy on polycrystalline Si seed layers on glass for thin-film Si solar cells

B. Rau¹, J. Klein¹, J. Schneider¹, M. Muske¹, E. Conrad¹, I. Sieber¹, M. Stöger-Pollach², P. Schattschneider², K. Petter¹, S. Brehme¹, S. Gall¹, K. Lips¹, W. Fuhs¹

■ 1 HMI, SE1 ■ 2 Technische Universität Wien, Austria

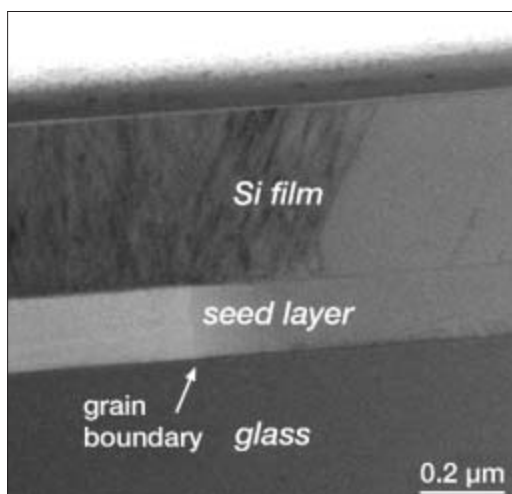


Fig. 1: TEM cross-section of a Si film grown on a poly-Si seed layer on glass. Right: epitaxy, left: fine-grained growth, no epitaxy (details see text)

The low-temperature epitaxial thickening of a large-grained polycrystalline Si (poly-Si) film on a foreign substrate like glass is a major challenge on the way to an efficient thin-film solar cell technology with a high potential for cost reduction. In such a concept [1] a thin poly-Si seed layer is used to enable, in principal, crystal growth with lateral grain sizes well above the thickness of the active layer of the solar cell. This seed layer is epitaxially (i. e. under retaining of its crystal information) thickened in a second step to form the absorber layer.

The substrate temperature of all processes involved is limited by the softening temperature of the glass to about 600°C. At these low temperatures it becomes necessary to apply deposition techniques which provide additional non-thermal energy to the surface of the growing film in order to obtain epitaxial growth of Si.

We have shown recently [2] that ion-assisted deposition techniques like electron-cyclotron resonance chemical vapour deposition (ECRCVD) using silane and hydrogen are suitable for epitaxial growth of Si at low temperatures. This technique features a high ion density and a moderate ion bombardment in a remote plasma configuration. Due to the impact of ions onto the growing film and the corresponding momentum transfer the adatom mobility is increased and epitaxial growth is enabled. But in contrast to conventional CVD at high temperatures (~1100°C) the substrate surface conditions (e.g. crystal orientation and surface cleanliness) still influence the epitaxial growth at low-temperatures strongly.

We developed a growth procedure that made it possible for the first time to realise epitaxial growth of Si by ECRCVD on glass based samples [3]. In Fig. 1 a transmission electron microscopy (TEM) sample cross section of a 400 nm thick Si film on a seed layer is given. The image shows the glass substrate (bottom), the seed layer (centre) and the Si film deposited by ECRCVD (top). A region of epitaxial thickening of the seed layer (upper right hand side) and a region of fine-polycrystalline growth (upper left hand side) are shown, caused by two differently oriented grains of the seed layer. The right grain is (100) oriented and has been epitaxially thickened with high crystal quality. The situation is strongly different on the left grain with a crystal orientation tilted with respect to (100). No epitaxy could be obtained here. From investigations of layers grown by ECRCVD on mono- and multicrystalline Si wafers we know, that only a crystal orientation of or close to (100) is favourable for Si epitaxy at temperatures below 600°C [4]. Therefore we used seed layers made by aluminium-induced crystallisation of amorphous Si [5] with a grain size of 10–20 μm and a high degree of (100) orientation. More than

80% of all grains were (100) oriented or were tilted less than 20° with respect to (100). Due to this high degree of preferential (100) orientation of the seed layers, we obtained epitaxy on up to 83% of the total area even at film thicknesses of about $1.8\ \mu\text{m}$.

The electronic properties of poly-Si thin-film solar cells with grain sizes well above the total thickness of the absorber layer are mainly influenced by intra-grain defects because of their activity as recombination centres for the transversal transport of generated charge carriers. Extended defects like dislocations and stacking faults and other defective regions can be made visible by etching the surfaces of samples by concentrated Secco etch. Secco etch preferentially etches the distorted regions around extended defects. As an example, the resulting etch pits in an epitaxially grown Si film on a monocrystalline Si(100) wafer are shown by a scanning electron microscopy (SEM) top-view image in Fig. 2. Different kinds of etch pits with characteristic shapes, sizes and crystallographic alignments were found. A typical total etch pit density for samples grown at 560°C is in the range of $10^8\ \text{cm}^{-2}$. This high density makes further sample treatments necessary in order to reduce the intra-grain defects (e.g. by rapid thermal annealing) or at least passivate them permanently by hydrogen-treatments.

Nevertheless, first glass/p⁺/p/n⁺ solar cell test structures using a slightly boron-doped ECRCVD grown absorber, a low-temperature, highly phosphorous-doped emitter (hydrogenated amorphous Si) and a ZnO film as transparent conducting window layer were prepared. Figure 3 shows the three major stages on the way to the solar cell. On a glass sub-

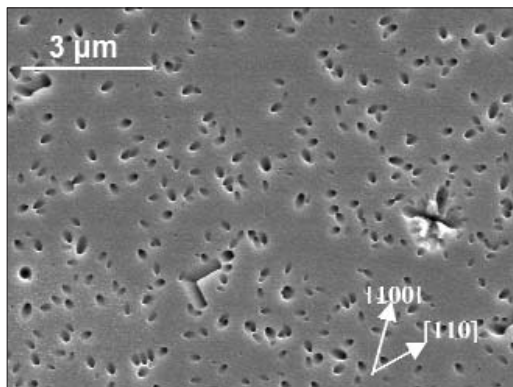


Fig. 2: SEM image of a Secco-etched surface of an epitaxially grown Si film (details see text)

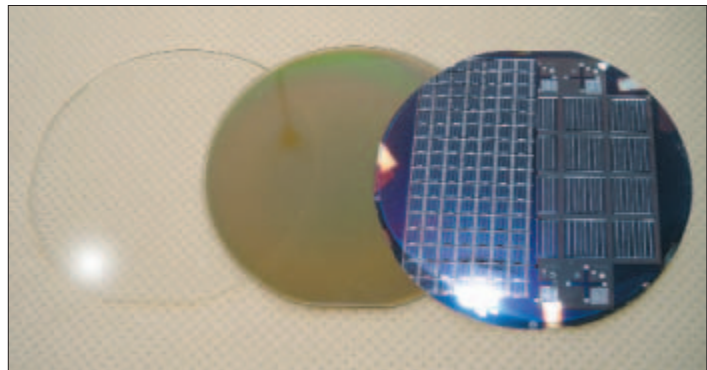


Fig. 3: The three major steps to a poly-Si thin-film solar cell on glass (substrate – seed layer – epitaxy and cell processing)

strate (left) a thin poly-Si film was created by metal-induced crystallisation of amorphous Si using the aluminium-induced layer exchange process (ALILE) (centre). This seed layer had now to be epitaxially thickened by ECRCVD to form an approximately $2\ \mu\text{m}$ thick absorber layer. Finally, after emitter and contact deposition, the cells were processed by photolithography (right). With such a structure we obtained first promising results with open-circuit-voltages of up to $284\ \text{mV}$. It is expected that an additional rapid high-temperature annealing step of the absorber layer and an effective defect passivation will lead to a strong improvement of the solar cell test structure. This is the challenge for the future work.

- [1] W. Fuhs, S. Gall, B. Rau, M. Schmidt, J. Schneider, *Solar Energy* **77**, 961 (2004)
- [2] J. Schwarzkopf, B. Selle, W. Bohne, J. Röhrich, I. Sieber, W. Fuhs, *J. Appl. Phys.* **93**, 5215 (2003)
- [3] B. Rau, I. Sieber, J. Schneider, M. Muske, M. Stöger-Pollach, P. Schattschneider, S. Gall, W. Fuhs, *J. Crystal Growth* **270**, 396 (2004)
- [4] B. Rau, I. Sieber, B. Selle, S. Brehme, U. Knipper, S. Gall, W. Fuhs, *Thin Solid Films* **451–452**, 644 (2003)
- [5] S. Gall, M. Muske, I. Sieber, O. Nast, W. Fuhs, *J. Non-Cryst. Solids* **299–302**, 741 (2002)

The work has been financially supported by the European Commission (METEOR project, ENK5-CT-2001-00543).

Corresponding author:

B. Rau
bjoern.rau@hmi.de

Compositional and electronic characterisation of Zn(O,OH) by PES for a better understanding of interfaces in chalcopyrite solar cells

M. Bär¹, J. Reichardt^{1*}, A. Grimm¹, I. Kötschau¹, I. Lauermann¹, K. Rahne¹, S. Sokoll¹, M. C. Lux-Steiner¹, Ch.-H. Fischer¹, L. Weinhardt², E. Umbach², C. Heske³, C. Jung⁴, W. Gudat⁴, T.P. Niesen⁵, S. Visbeck⁵

■ 1 HMI, SE 2 ■ 2 Exp. Physik II, Universität Würzburg, Germany ■ 3 Dept. of Chemistry, University of Nevada, Las Vegas, USA ■ 4 BESSY Berlin, Germany ■ 5 Shell Solar GmbH, Munich, Germany

* present address: Institute of Theoretical Physics, University of Bremen, Germany

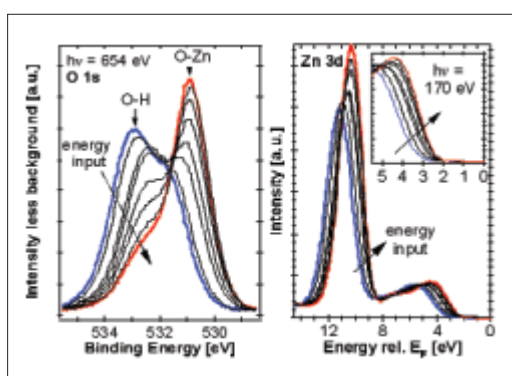


Fig. 1: Changes in PES detail spectra of an ILGAR-Zn(O,OH) layer on a CIGSSe absorber due to the energy input of the synchrotron beam (at $h\nu = 654$ eV).

left: O 1s emission at an excitation energy of $h\nu = 654$ eV.

right: Zn 3d emission and the valence band edge (insert) at an excitation energy of $h\nu = 170$ eV.

Nowadays, the necessity of alternative energy use is widely accepted. In photovoltaic solar energy technology, crystalline silicon cells are currently dominating in the market, though their cost reduction potential is seen to be limited. Thin film solar technology based on the chalcopyrites $\text{Cu}(\text{In}_{(1-X)}\text{Ga}_X)(\text{S}_Y\text{Se}_{(1-Y)})_2$ ("CIGSSe") with $0 \leq X \leq 1$ and $0 \leq Y \leq 1$ is very promising due to expected lower production costs and shorter energy pay back times. Meanwhile, the efficiency of CIGSe based laboratory cells (0.408 cm^2) has reached almost 20% [1], while industrially produced CIGSSe module prototypes ($60 \times 90 \text{ cm}^2$) have demonstrated efficiencies above 13% [2]. A chalcopyrite-based solar cell is a multilayer system and the quality of the interfaces crucially determines the photovoltaic performance of the cell. Successful interface engineering requires compositional and electronic material characterisation as a prerequisite

for understanding and intentionally generating interfaces. In the following, we present an example for such an approach. Photoelectron spectroscopy with synchrotron radiation is used for both, chemical analysis and determination of the valence band maximum. These data are successfully correlated with the process temperature of the layer deposition as well as with the resulting solar cell efficiencies.

In conventional chalcopyrite solar cells the buffer layer between absorber and window consists of CdS. Despite the small quantity, this is an ecological drawback. Consequently, there is a demand for a non-toxic, more transparent buffer material. One promising approach is the replacement of CdS by a ZnO buffer layer, deposited by the ion layer gas reaction (ILGAR) method. This method has already led to superior cell efficiencies compared to CdS-containing references [3]. Since the chemical, cyclic, and sequential ILGAR deposition of oxide layers occurs via the corresponding hydroxide [4], which is subsequently dehydrated in the heated reaction chamber, the process temperature directly determines the O/OH-ratio of the samples. Therefore, it is possible to prepare ILGAR layers ranging from almost pure $\text{Zn}(\text{OH})_2$ (deposition at room temperature) to nearly hydroxide-free ZnO (process temperature $> 200^\circ\text{C}$) [5]. Hence, these ILGAR buffers consist of a Zn(O,OH) compound when processed at slightly elevated process temperatures ($55^\circ\text{C} - 125^\circ\text{C}$), as in our case are used. For simplicity, we will still refer to this material as *ILGAR-ZnO*.

Experiments have shown a pronounced drop in solar cell performance when ILGAR-ZnO buffers are prepared above 100°C [3]. One suggested explanation was a deteriorating impact of an increasing O/OH-ratio, influencing the band alignment at the ILGAR-ZnO/CIGSSe hetero-interface.

In order to study this subject, the O/OH-ratio of ILGAR-ZnO layers was investigated in the CISSY apparatus by means of photoelectron spectroscopy (PES) and correlated with the determined position of the valence band maximum (VBM). An approx. 20 nm thick ILGAR Zn(O,OH) layer, consisting mainly of hydroxide, was irradiated with synchrotron radiation of 654 eV (at the undulator beamline U41-PGM) and the O 1s PES signal was measured in intervals of a few minutes (using a VG CLAM 4 electron analyser). One clearly sees that the oxide peak (530.9 eV) grows at the cost of the hydroxide peak (533.0 eV, peak assignments according to [6]) due to dehydration by the energy input of the synchrotron beam, which also heats the sample. Directly after each O 1s measurement, the excitation energy was tuned to 170 eV and the Zn 3d and valence band signals were recorded (Fig. 1, right). One can observe that the continuous dehydration of the ILGAR-ZnO layer goes along with a shift of the Zn 3d signal from 11.2 eV to 10.4 eV (typical for ZnO [7]) and a shift of the VBM at the surface from 3.8 eV to 2.4 eV. By fitting and integrating the hydroxide and oxide contributions to the O 1s emission, respectively, the ZnO/(ZnO + Zn(OH)₂) ratio at the surface could be determined.

The corresponding positions of the conduction band minimum (CBM) are estimated using the band gap energies E_g revealed by optical measurements of respective ILGAR-ZnO layers on glass. CBM and VBM data of the Zn(O,OH) are plotted against oxide content at the surface (Fig. 2, bottom). Previous results from x-ray- (XPS) and UV-light-excited photoelectron (UPS) as well as inverse photoemission spectroscopy (IPES) [6] (full triangles) are in good agreement with CBM and VBM values determined in this way. The dotted lines represent the data for the Cd²⁺/NH₃-treated CIGSSe substrate [6]. In Fig. 2 (top) the resulting power conversion efficiencies (η) of ILGAR-ZnO/CIGSSe cells versus the respective buffer compositions are shown. The η -drop may now be directly linked to the ZnO/(ZnO + Zn(OH)₂) ratio of the buffer. A detailed discussion will be published elsewhere [9]. However, while a predominantly flat conduction band offset (CBO) can be achieved for ZnO/(ZnO + Zn(OH)₂) ~ 0.56 with a decreasing hydroxide content (assuming that interface-induced band bending effects are negligible), an increasing spike-like CBO above 0.4 eV for oxide-rich ILGAR layers is predicted. The latter may partially (but not exclusively) explain the drop of the power conversion efficiency of resulting solar cells if the ILGAR-ZnO layer is prepared above a process temperature of 100°C, resulting in a hydroxide-poor buffer composition.

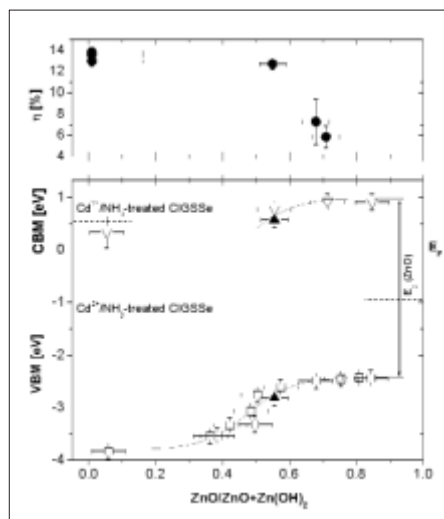


Fig. 2: bottom: The determined VBM values (squares) and estimated CBM (\approx VBM + E_g) values (open triangles) of ILGAR-ZnO layers with different ZnO/(ZnO + Zn(OH)₂) composition compared to previous values [6] for VBM and CBM (directly determined by UPS and IPES, full triangles). The CBM trend line is separated from the VBM trend line by

$E_g(\text{ZnO}) = 3.35 \text{ eV}$ [8]. The dashed lines represent the VBM and the CBM, respectively, of a Cd²⁺/NH₃-treated CIGSSe absorber [6]. **top:** Power conversion efficiency η of CIGSSe based solar cells with ILGAR-ZnO buffers deposited at different process temperatures [3], shown as function of the Zn(O,OH) composition of the buffer.

Acknowledgement

Financial support by the German BMBF (# 01SF0007) and BMWA (# 0329889) is gratefully acknowledged.

- [1] K. Ramanathan, M. A. Contreras, C. L. Perkins, S. Asher, F. S. Hasoon, J. Keane, D. Young, M. Romero, W. Metzger, R. Noufi, J. Ward, A. Duda, *Prog. Photovolt.: Res. Appl.* **11**, 225 (2003)
- [2] V. Probst, Technical Digest of the 14th International Photovoltaic Science and Engineering Conference, 2004, p. 663
- [3] M. Bär, Ch.-H. Fischer, H.-J. Muffler, B. Leupolt, T. P. Niesen, F. Karg, M. C. Lux-Steiner, *Proc. 29th IEEE Photovoltaic Specialists Conference*, New Orleans, USA, 636 (2002)
- [4] M. Bär, H.-J. Muffler, Ch.-H. Fischer, M. C. Lux-Steiner, *Sol. Energy Mater. Sol. Cells* **67**, 113 (2001)
- [5] Ch.-H. Fischer, H.-J. Muffler; M. Bär, S. Fiechter; B. Leupolt, M. Ch. Lux-Steiner, *J. Crystal Growth* **241**, 151 (2002)
- [6] L. Weinhardt, M. Bär, H.-J. Muffler, Ch.-H. Fischer, M. Ch. Lux-Steiner, T. P. Niesen, F. Karg, Th. Gleim, C. Heske, E. Umbach, *Thin Solid Films* **431–432**, 272 (2003)
- [7] S. W. Gaarenstroom, N. Winograd, *J. Chem. Phys.* **67**, 3500 (1977)
- [8] Landolt-Börnstein, *Halbleiter. II-VI Compounds*, III 22a, Springer Verlag, Berlin (1985)
- [9] M. Bär *et al.*, in preparation

Corresponding author:

Ch.-H. Fischer
fischer@hmi.de

Time dependent charge separation in a nanoporous TiO_2 model system studied by surface photovoltage

Th. Dittrich¹, I. Mora-Seró², J. Bisquert²

■ 1 HMI, SE2 ■ 2 Departament de Ciències Experimentals, Universitat Jaume I, Castello, Spain

Spatial charge separation is important in many biological, chemical and physical systems and can take place at extremely different time and length scales depending on the investigated system. For example, charge separation may proceed within tens of fs during ultra-fast injection from dye molecules into TiO_2 [1] or over long times during diffusion in a porous semiconductor [2]. On the other side, light-induced charge may be separated over distances between molecules up to the range of space charge regions. In devices such as nanostructured solar cells [3] or so-called eta (extremely thin absorber) solar cells, it is important to clarify the time and length scales at which the related processes of initial charge separation, carrier transport and recombination take place.

In contrast to time dependent optical investigations, surface photovoltage (SPV) measurements give information about both time *and* length scales of charge separation. This opens the opportunity to measure transport phenomena from the ns to the s range with excellent sensitivity. Figure 1 summarizes elementary processes dominating charge separation at extremely different time scales for a model system in which the positive light induced charge remains fixed near the surface and only electrons are mobile. In our SPV studies, the processes B–E were clearly distinguished.

Recently, SPV measurements were performed on different electron and hole conductors with adsorbed N3 ($\text{Ru}(\text{dcbpyH}_2)_2(\text{NCS})_2$) dye molecules [4]. Further, it has been shown that N3 dye molecules adsorbed at TiO_2 surfaces are very stable in vacuum at relatively high temperatures [5]. Following this experience, we realized a model system, similarly to the system shown in Fig. 1, for time and temperature dependent SPV measurements on nanoporous TiO_2 .

Nanoporous TiO_2 layers of interconnected anatase nanoparticles (diameter of the particles about 16 nm) were deposited on glass coated with conducting $\text{SnO}_2:\text{F}$. Only the surface region of the nanoporous TiO_2 layers was sensitized with dye molecules by short dipping in the dye solution. Spectral surface photovoltage measurements showed the typical absorption behavior of the N3 dye molecules.

SPV measurements were carried out in the capacitor arrangement with a thin mica layer as spacer. Light pulses of the 2nd harmonic of a Nd:YAG laser (wavelength 531 nm, duration time 120 ps) were used for excitation. At this wavelength, the light was absorbed only by N3 dye molecules but not by TiO_2 nanoparticles. The resolution time of the whole system was better than 2 ns. Before starting the SPV measurements, the sample was conditioned inside the evacuated cryostat at 270°C for 30 min.

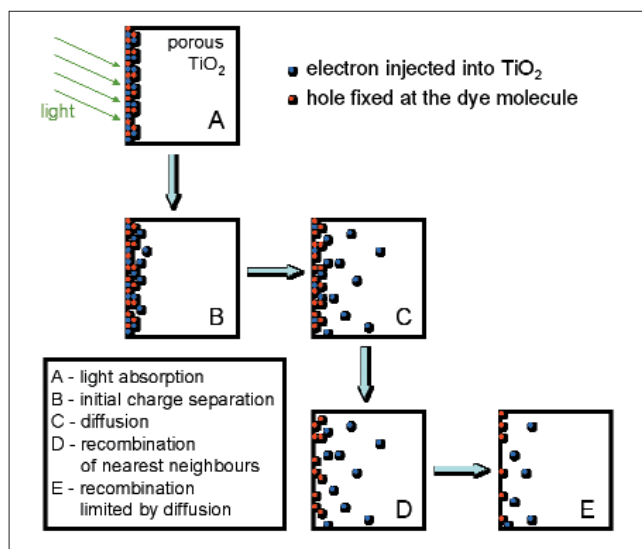


Fig. 1: Scheme of elementary processes in the investigated model system consisting of a nanoporous TiO_2 layer sensitized with dye molecules near the surface. In addition, dielectric relaxation has to be considered. The nanoporous TiO_2 can be treated as an effective medium. The photovoltage is given by the amount of separated charge and by the effective charge separation length.

Figure 2 shows examples for SPV transients in linear-log and log-log scales for a nanoporous TiO_2 layer sensitized with N3 dye molecules near the surface. The SPV transients were measured at different temperatures for quite low excitation intensity. The SPV signals increase in time, reach a characteristic maximum at times much longer than the laser pulse and decay. The characteristic maximum depends strongly on temperature and is determined mainly by dielectric relaxation.

The increase at the shorter times as well as the decrease at the long times (for higher temperatures) of the SPV transients follow power laws (Fig. 2b). The power laws indicate diffusion and dispersive transport during increasing charge separation length due to independent diffusion and during decreasing charge separation due to recombination limited by diffusion (processes C and E in Fig. 1), respectively. As remark, the power coefficients can be well interpreted in traditional time-of-flight experiments where the displacement current is measured. The situation is much more complicated for the interpretation of SPV transients. The creation of a sophisticated model and simulations of SPV transients are a great challenge for future.

At a fixed intensity of the laser pulse, the extrapolated on a log-log scale SPV transients have a common point of intersection for the different temperatures. The time at the point of intersection is independent of the intensity of the laser pulse and amounts to about 100 ps, i.e. the duration time of the laser pulse. At this time, the extrapolated SPV signal scales linearly with the intensity of the laser pulse. Therefore, dispersive transport sets on within the laser pulse and a respective initial charge separation length of 3–10 nm has been estimated (process B in Fig. 1) [6]. Further, the power-law approximation may open new opportunities for the investigation of initial charge separation at ultra-short times if working with much shorter laser pulses.

The fastest relaxation process of the SPV signal can be described by a logarithmic decay which probably indicates to recombination between nearest neighbors, i.e. to limitation by tunneling over a variable range of distances (process D in Fig. 1). A logarithmic decay time (τ_{LN}) can be defined (see the example in Fig. 2b).

At higher temperatures, τ_{LN} is thermally activated and independent of the intensity of the laser pulse [6]. The values of the activation energy and of τ_{LN}^0 are 0.65 eV and 2 ps, respectively. The observed activation energy is typical for the thermally activated conductivity in TiO_2 . This gives further evidence that the decay of the SPV transients is limited by the electron transport. The obtained value $\tau_{\text{LN}}^0 = 2 \text{ ps}$ is typical for multiple trapping, for example in amorphous Si, and it reflects the shortest possible time for charge transfer of an electron back into a charged dye molecule. Of course, this time may be much longer than the electron transfer from the adsorbed dye molecule into the TiO_2 nanoparticle [1].

We demonstrated that the SPV technique is a powerful tool to obtain information about spatial charge separation in a wide range of time scales from ps to s. Besides the signatures for diffusion and dispersive transport, a logarithmic decay was observed for photovoltage transients in porous TiO_2 sensitized at the surface with dye molecules [6].

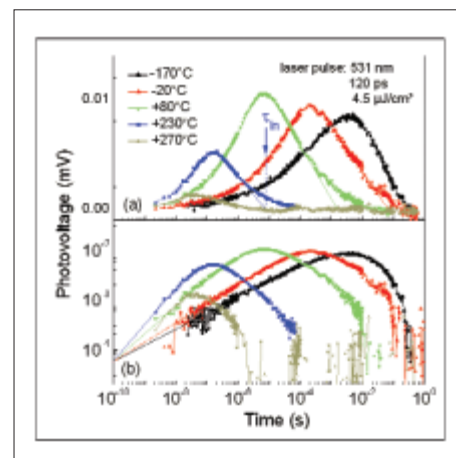


Fig. 2: SPV transients in linear-log (a) and log-log (b) plots for a nanoporous TiO_2 layer sensitized with dye molecules near the surface. The repetition rate of the laser pulses was 1 Hz.

- [1] see, for example, K. Schwarzburg, R. Ernstdorfer, S. Felber, F. Willig, *Coordination Chemistry Review* **248**, 1259–1270 (2004), and refs. therein
- [2] V. Duzhko, V. Yu. Timoshenko, F. Koch, Th. Dittrich, *Phys. Rev. B* **64**, 0752041–0752047 (2001)
- [3] M. Grätzel, *Nature* **414**, 338–344 (2001) and refs. therein
- [4] B. Mahrov, G. Boschloo, A. Hagfeldt, L. Dloczik, Th. Dittrich, *Appl. Phys. Lett.* **84**, 5455–5457 (2004)
- [5] Th. Dittrich, *phys. stat. sol. (a)* **201**, R69–R71 (2004)
- [6] Th. Dittrich, I. Mora-Sero, J. Bisquert, submitted

Corresponding author:

Th. Dittrich
dittrich@hmi.de

Electrical activity at grain boundaries of Cu(Ga, In)Se₂ thin films

D. Fuertes Marrón¹, S. Sadewasser¹, A. Meeder², Th. Glatzel¹, M. Ch. Lux-Steiner¹

■ 1 HMI, SE2 ■ 2 SULFURCELL Solartechnik GmbH

In comparison to grain boundaries (GBs) in Si, those in chalcopyrite semiconductors are by far not as well studied nor understood. Only very recently have some experimental and theoretical studies been conducted, motivated by the remarkably high solar energy conversion efficiencies of polycrystalline absorbers compared to those obtained so far from single-crystalline ones. Reaching efficiency figures close to 20% from any type of polycrystalline absorber (including as well Si or CdTe) necessarily requires a favourable behaviour of the GBs. Experimental studies have demonstrated electrical effects at p-type chalcopyrite GBs, both indirectly by Hall and conductivity measurements and directly using Kelvin probe force microscopy (KPFM); results were explained according to a GB model developed for Si, which assumes a depletion layer in the near-GB region induced by some charge storage at interface states.

This bends the bands downwards some 100 meV, representing an electrostatic barrier for the transport of holes (typically majority carriers) and a sink for electrons (minority ones). The depletion region on either side of the GB plane results from positively charged interface states. The minor detrimental role attributed to GBs in polycrystalline thin-film solar cells is accounted for within the frame of this *electronic* GB model by a certain reduction of the band bending at the GBs gained under illumination (i.e. under solar cell operating conditions), as a fraction of minority carriers are trapped at interface states, reducing the net stored charge and thus the associated electric field and depletion region.

In contrast to the *electronic* GB model, a recent theoretical study using first-principles modelling of GBs for selected grain orientations in CuInSe₂ proposed the appearance of an energetic barrier for holes arriving from the inner part of the grains without the presence of interface charge at GBs. A reduced *p-d* hybridization between group-I-cation and chalcogen-anion states, due to Cu-vacancy surface reconstruction, was proposed to lead to an overall downward shift of the valence band maximum in the near-GB region. This model can indeed account for the experimental observations based on electronic transport measurements mentioned above. The absence of available free holes at GBs prevents electron recombination, minimizing the detrimental effects for electronic applications as a result of minority carrier loss. This *structural* GB model explicitly excludes built-in potentials (i.e. stored charge) at GBs. This is understood as the result of a self-compensation of electronic point defects by their arrangement into neutral pairs of the type $2V_{-Cu} + In^{2+}_{Cu}$.

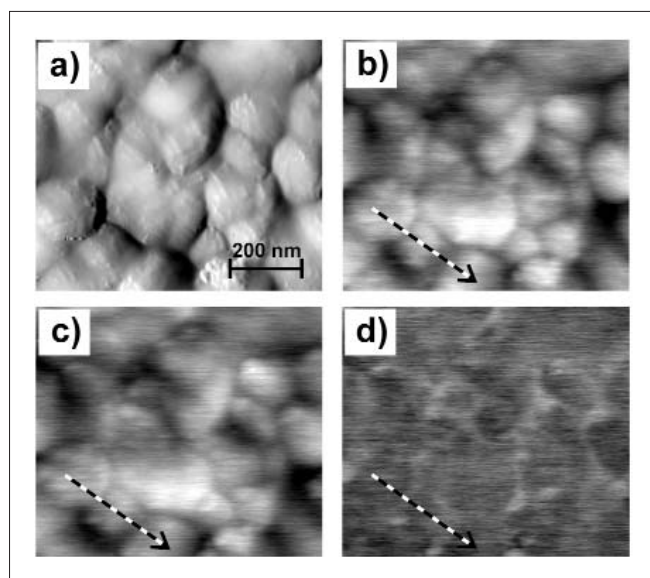


Fig. 1: KPFM measurement on the UHV-clean rear side of a CuGaSe₂ absorber film. **a)** Topography (height range = 92 nm), **b)** work function in dark (4.79–4.94 eV), **c)** work function under illumination (4.88–5.01 eV), and **d)** SPV image (41–140 mV). Different GB types are distinguished by the presence or absence of SPV. The line represents the position of the line scan in Fig. 2.

To investigate the applicability of the two GB models, we used KPFM in ultra-high vacuum (UHV) to study polycrystalline CuGaSe₂ (CGSe) thin-film samples grown in a two-stage process by chemical vapour transport onto Mo-coated soda-lime glass. Samples were peeled-off in UHV in order to expose a clean rear surface to the tip.

The topography image of the CGSe rear surface (Fig. 1a) shows a granular texture, corresponding to the base of columnar grains ($\sim 3\ \mu\text{m}$ long) with lateral dimensions between 50–400 nm; in contrast, typical grain widths at the film top surface lie in the micrometer range. GBs can be identified in the work function mapped in the dark in Fig. 1b by direct inspection and comparison to the topographical image, showing lower work function values than the crystallite surfaces. This effect is clearly seen along a representative line-scan shown in Fig. 2. Three adjacent grains build up GBs A and B. The work function lowering associated with the GBs is different in magnitude by a factor of approximately two. Due to the flat topography of the absorber's rear surface (height range $\sim 90\ \text{nm}$), any possible influence of surface roughness on the work function measurement can be largely excluded. This work function reduction at GBs as recorded in the dark is however not sufficient to favour the *structural* or the *electronic* GB model.

Thus, we additionally studied the electronics at energies above the Fermi level, i. e., the changes observed in the electrical activity at GBs induced by excess electrons, acting as minority carriers. If GBs were governed by *structural* (i. e., band offsets) rather than *electronic* (built-in potential) factors as described by the models, the impact of the excess minority carriers should only be minor. Illuminating the sample with super-bandgap light (laser diode, $\lambda = 675\ \text{nm}$) results in an overall increase of the work function (Fig. 1c) which saturates at high intensities ($\sim 60\ \text{mW}/\text{cm}^2$), an effect attributed to a reduction of the surface band bending in the scanned (sample-vacuum) surface plane. In Fig. 1d a surface photovoltage image ($\text{SPV} = \Phi^{\text{ill}} - \Phi^{\text{dark}}$) of the scanned area is presented, obtained by subtracting Fig. 1b (measured in the dark) from Fig. 1c (under illumination), which shows the presence of at least two distinct GB types, one showing a larger SPV than the grains (bright areas) and others which do not show up. A representative line scan in Fig. 2 shows a significant reduction of the work function drop recorded at GB B under illumination, together with the overall increase in work function attributed to SPV on the scanned surface plane; this shows up as a characteristic peak in the SPV line (bottom). At the same time, GB A shows almost no change under illumination. This leads us to conclude the existence of different types of GBs, presumably associated with particular crystallite orientations. This connection between crystallite orientation and GB electrical activity can explain the influence of

film texturing on the performance of high efficiency solar cells, in addition to a favourable band alignment between absorber and buffer layers, a point which has not yet received sufficient attention and which may in our opinion be of fundamental importance for further device optimisation.

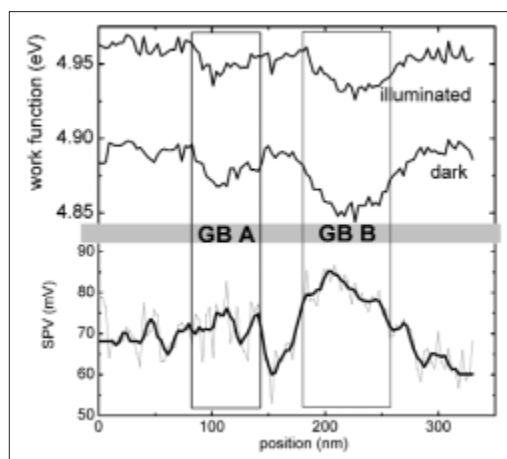


Fig. 2: Line scan along the line in Fig. 1. Upper panel: A drop in the work function (in dark and under illumination) at the position of the GBs is observed. GBs A and B are of different types as indicated by their different SPV characteristic (lower panel); the line is a smoothed curve of the data (gray line).

The reduction of the potential barrier at GBs associated with illumination cannot be accounted for within the frame of the *structural* GB model under the exclusive premise of an interface dipole. The decrease of the work function fits however into the *electronic* GB model: a reduction of the potential barrier is due to photo-generated minority carriers (electrons) being trapped at ionised donor-like electronic states at the GB. The mechanism of light-induced GB passivation within the *electronic* GB model does not seem to apply equally to all types of GBs. For example, the behaviour of GBs of type A, which shows almost no change under illumination, might well be explained to a large extent by the *structural* GB model. On the other hand, the illumination induced change in the GB of type B does require the *electronic* GB model.

This work was financially supported by the German Ministry for Research and Education (Contract No. 01SF0023).

This work has been published in Phys. Rev. B **71**, 033306 (2005)

Corresponding author:
D. Fuertes Marrón
fuertes-marron@hmi.de

Production of CuInS_2 baseline modules on $5 \times 5 \text{ cm}^2$ substrates with high yield

J. Klaer¹, R. Klenk², R. Scheer¹, H.-W. Schock¹

■ 1 HMI, SE3 ■ 2 HMI, SE2

Research in the department SE3 is focussed on the technology of thin-film photovoltaic devices with absorbers based on chalcopyrite compound semiconductors. A baseline process has been developed for the preparation of CuInS_2 solar cells and mini modules up to $10 \times 10 \text{ cm}^2$ in size. Samples originating from this baseline process are used for research on special questions and development of single process steps. For many purposes small area single cells are the adequate type of device.

In the face of future commercial application, modules are of particular interest. Additional process steps are necessary to fabricate modules that normally are not needed for single cells, e.g. integrated series connection and encapsulation. In 2003 the company Sulfurcell has been founded by the Hahn-Meitner-Institut scientists in order to fabricate commercial modules based on the process developed in the department SE3. A corporation contract between the Hahn-Meitner-Institut and Sulfurcell provides scientific support from the Hahn-Meitner-Institut.

Against this background it is of special importance to maintain a continuous fabrication of mini-modules in the SE3 baseline. This allows a consecutive process control and improvement of module related process steps. Additionally it is a proof of the stability of the process, an essential item for industrial suitability.

From July to December 2004 in total 128 modules have been fabricated on $5 \times 5 \text{ cm}^2$ glass substrates. Figure 1 shows the yield of the fabrication process for these modules: the blue histogram gives the number of modules in efficiency intervals of 0.1 %, respectively, while the red curve gives the accumulative yield. Only 10 modules have efficiencies less than 6.9%, the best module is close to 10 %, and the maximum of the distribution shows at 9%. According to the red curve, modules with 8% efficiency have been produced at a yield of about 75%, which means that 75% of all modules fabricated have efficiencies of 8% or more. For 7% modules the yield is about 90%.

Only modules produced with baseline parameters are included within the 128 modules shown in Fig. 1. Baseline devices, both solar cells and modules, are processed with well defined process parameters that have been evaluated as optimum and set as a standard. Besides these baseline devices a large number of additional samples with deliberately deviating process parameters have been processed. These experiments are essential in the context of research and process development, but they result in samples that are not relevant within a baseline statistics.

During the first 6 months of 2004 the efficiency distribution was much broader compared to Fig. 1, showing many modules with only poor or moderate efficiencies. This poor statistics can be attributed to various problems with processing that meanwhile could be solved. This underlines the necessity of continuous module preparation for process improvement.

Additionally to the devices on $5 \times 5 \text{ cm}^2$ substrates a couple of $10 \times 10 \text{ cm}^2$ modules have also been processed. Its number is too small to give meaningful statistics, but the best $10 \times 10 \text{ cm}^2$ module has achieved 8.9% efficiency so far. An example of such a module already encapsulated is shown in Fig. 2.

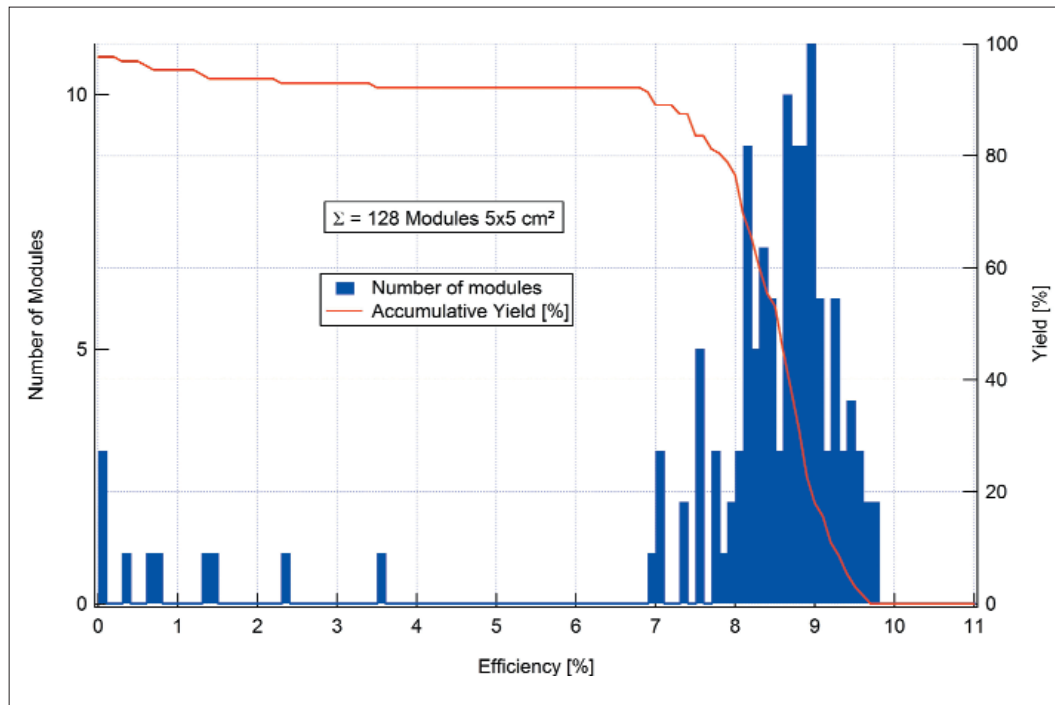


Fig. 1: Efficiencies of all baseline modules on $5 \times 5 \text{ cm}^2$ processed during 6 months July to December 2004. The blue histogram shows the number of modules in an efficiency range of 0.1%, respectively, the red curve shows the accumulative yield.

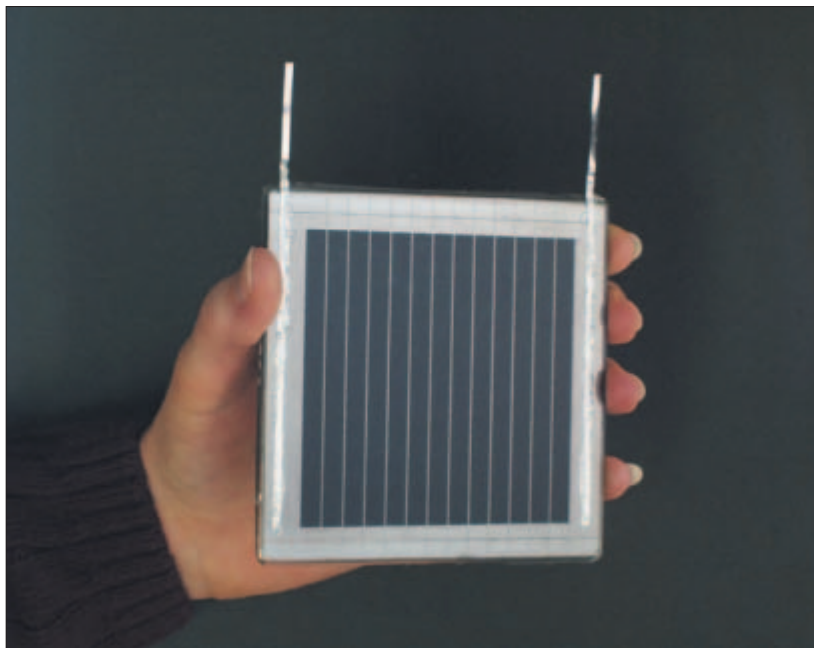


Fig. 2: Encapsulated CuInS_2 module with 13 integrated series connected cells on a $10 \times 10 \text{ cm}^2$ glass substrate

Thin film photovoltaics: diagnostics and repair

R. Scheer
 ■ HMI, SE3

The inherent advantage of thin film photovoltaic modules is the monolithic integration of a large number of solar cells on a substrate. These cells are series interconnected as a result of the production scheme and do not have to be interconnected ex post during module fabrication like in the wafer technology. However, this advantage may turn into a disadvantage if local failures on the substrate of typically $60 \times 120 \text{ cm}^2$ reduce the overall performance of the thin film module. Failure sources can be inhomogeneous processing along the dimensions of the substrate or simply micro defects due to particles.

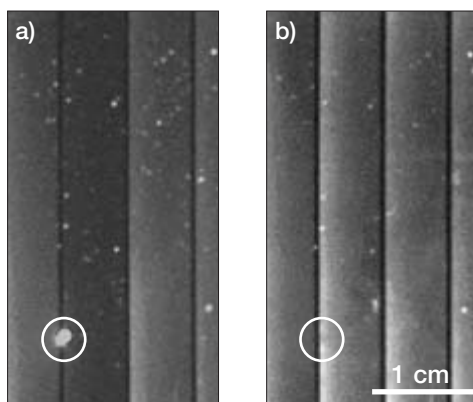


Fig. 1: Lock-in infrared thermography images of a CuInS_2 mini-module from the Hahn-Meitner-Institut baseline, **a)** before and **b)** after module repair. White contrast represents higher temperature due to higher electrical power dissipation. Vertical dark lines depict the positions of the series interconnections. Each grey vertical bar of 0.6 cm width represents one solar cell. White circles mark the position of shunt removal by an excimer laser. Note the reduced brightness of the second left bar in **a)** and its increased brightness after shunt removal.

What is the impact of a local shunt on the module performance? Due to the limited conductance of thin films, a local shunt or weak diode is electrically screened within a distance of typically $< 1 \text{ cm}$ [1]. If a local shunt, however, is located in the vicinity of the interconnect, the higher conductance of the metallic back electrode leads to a screening length of up to 10 cm. With a total cell length of 120 cm, a single shunt then can deteriorate the photovoltaic action of 20 cm or about 15% of a cell. If such a shunt occurs on several cells of the module, the power reduction can be in the range of 1% absolute performance loss.

A local shunt can be visualized by infrared thermography. If an electric current is passed through the module, the shunt represents a position of higher power dissipation and radiates more energy. Higher power dissipation at shunts can also be detected if the electric energy is generated within the module by the photovoltaic effect. This means the module can be put under electrical or light bias in order to record images of infrared response. Figure 1 gives an example of a module under electrical bias. In order to increase the spatial resolution, the lock-in thermography has been used. The left image in **a)** shows the module before repair. Along the interconnect of the second left cell (interconnects represented by vertical dark lines), we find a locally increased temperature due to a strong shunt. The second left cell exhibits a lower brightness in the thermographic image if compared to other cells. The shunt robs the current of the complete second cell during the electric bias as it would rob the current under photovoltaic action. Due to its proximity to the interconnect, the shunt cannot be screened within 1 cm. The current density and thus the thermal radiation of the rest of the second cell is reduced within a distance of 3 cm.

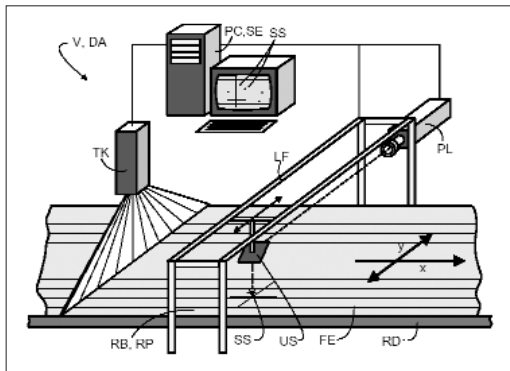


Fig. 2: Sketch of a suggested in-line machine for automatic module diagnosis and repair using a Thermocamera (TK) and a laser (PL). The substrate is moving in direction of x . Due to their higher power dissipation, local shunts (SS) are detected by the thermocamera and recorded by a computer (PC). In case of a local shunt detection, the mirror (US) is positioned above the shunt and a laser puls is directed onto the module surface at the defected area. The transparent conductive ZnO layer is selectively removed.

Local shunts can be eliminated by local abrasion of all semiconducting layers or by selective removal of the transparent front contact layer. While the former can be accomplished mechanically, we found that by use of an excimer laser, the transparent conductive ZnO layer of a ZnO/CdS/CuInS₂/Mo stack can be selectively removed. The laser wavelength and the puls length were 284 nm and 39 ns, respectively. The power threshold for the laser ablation was around 900 mJ/cm². For lower energy density, the ZnO ablation was not complete. A necessary condition for the selective removal of the ZnO layer is the application of only one laser puls. Under application of a second puls, the absorber layer is melted leading to new shunt paths. Figure 1b) shows a thermography image of the same module after local shunt removal using the excimer laser. No local heating is observed anymore, the temperature of the second cell due to the passing electrical current is equal to the one of the other cells. Local ablation of the front contact certainly disables the photovoltaic action of the ablated site. Due to the small focus of the laser, however, the site can be small. It is not visible in image b) of

Fig. 1. In the current example, the efficiency of the module rose from 7.71% before shunt removal to 8.42% after shunt removal.

The avoidance of local shunts in a photovoltaic thin film production is a matter of substrate processing and may be accomplished by an improved production equipment. On the other hand, it may be backed up by quality control using larger area IR thermography using modern IR line cameras. We suggested to combine quality control by IR thermography and cell repair by selective laser ablation in an in-line supervision and repair machine [2]. Figure 2 shows a possible set-up for such a diagnosis and repair machine. It provides a shunt statistic which can be used for quality assurance. This piece of equipment in the future may be useful to maintain high yield in photovoltaic thin film production and thereby reduce costs.

-
- [1] V.G. Karpov, A.D. Compaan, D. Shvydka, *Effects of nonuniformity in thin-film photovoltaics*, Applied Physics Letters, **80** (22), 4256 (2002)
 - [2] R. Scheer, *Verfahren und Vorrichtung zu Diagnose und Qualitätssicherung von halbleitenden Dünnschichtsolarmodulen*, Deutsches Patent- und Markenamt, 2004, Anmeldung 10 2004 046 324.7

Prototype development – flexible high efficiency $\text{Cu}(\text{In,Ga})\text{Se}_2$ thin film solar cells for space applications

A. Neisser¹, C. A. Kaufmann², R. Klenk², R. Scheer¹, H.-W. Schock¹

■ 1 HMI, SE3 ■ 2 HMI, SE2

Development of flexible thin film technologies for photovoltaic energy conversion are attracting increasing attention. One of the major driving forces is a growing interest from space industry in lightweight thin film solar arrays of improved power to weight ratio and radiation hardness.

The Dept. SE3 and SE2 of the Hahn-Meitner-Institut, Berlin and Dutch Space B.V., Leiden cooperate in a joint effort with the aim to develop a flexible thin film solar cell based on $\text{Cu}(\text{In,Ga})\text{Se}_2$ (CIGSe) to be integrated into an array structure for space applications. Since late 2003 the cooperation has been supported by the European Space Agency ESA as part of their Thin Film Solar Array Development Program. Furthermore, the Centre for Solar Energy and Hydrogen Research Baden-Württemberg, Stuttgart has joined this collaboration.

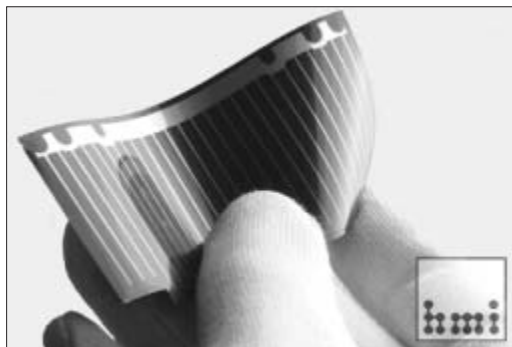


Fig. 1: Prototype of a lightweight flexible solar cell based on $\text{Cu}(\text{In,Ga})\text{Se}_2$. The total area (excluding busbar) is 27.1 cm^2 . This type of device has reached an efficiency of 15.0% under one-sun reference illumination (AM1.5).

Among the thin film technologies, chalcopyrite based solar cells bear the greatest potential; they have demonstrated energy conversion efficiencies of almost 20% on rigid glass substrates, show excellent radiation hardness in the laboratory as well as in in-flight tests, plus, they have successfully been deposited on flexible substrates. With an apt choice of lightweight material, heavy support structures as they are necessary in current space technologies become obsolete. As a consequence new, lightweight array designs with much higher power to weight ratio can be developed.

Starting point of the space cell development was a standard lab-scale preparation process (baseline) for high efficiency CIGSe thin film solar cells recently established by the Hahn-Meitner-Institut team. The CIGSe thin film devices comprises the layer sequence $\text{Mo/CIGSe/CdS/i-ZnO/ZnO:Al}$. Established technologies such as DC-sputtering (Mo), evaporation (NaF, CIGSe, Ni, Al, Au), chemical bath deposition (CdS), and RF-sputtering (i-ZnO, ZnO:Ga) are used. This technology could be successfully transferred to flexible titanium foil substrates without any major loss in cell performance [1]. However, the increase of the solar cell device area from a lab scale area (about 0.5 cm^2) to prototype dimensions necessary for the projected array structure is not straightforward. Therefore, recent efforts have been focused on advances in performance optimization of large area single solar cells (Fig. 1), produced on Ti-foil substrates with an area of up to 29.7 cm^2 (total area w/o busbar 27.1 cm^2) [2]. First devices showed very low fill factors and process reproducibility was poor. Device analysis revealed that the decrease in device performance was mainly due to parasitic leakage currents shunting the junction. Using lock-in thermography imaging these shunts could be assigned to local defects of the device structure caused by substrate irregularities. Hence a substrate pre-treatment step was introduced and as a result the homo-

geneity and reproducibility of the produced large area devices has been improved. Figure 2 shows a histogram of the number of finished 27.1 cm^2 samples versus their respective AM1.5 efficiency over a period of two months. The high reproducibility of the Hahn-Meitner-Institut baseline as illustrated by a narrow distribution around 12%–13% is an important prerequisite for the ongoing array development at Dutch Space. Current record efficiencies for a 27.1 cm^2 CIGSe thin film device are 15.0% under AM1.5. This represent the highest values so far reported for a large area thin film single solar cell. However, there is still a significant drop in device performance (particularly the fill factor) with increased area (see Table 1). Large area devices reach only 85%–90% of the performance of small ones. Ongoing process development large and the analysis of a large number of samples have shown that there are three main contributions to the observed scale-up loss:

- grid finger losses
- parasitic leakage currents – local shunts
- lateral inhomogeneities of device parameters due to material non-uniformities

About 8% of the observed scale-up loss is due to the higher grid finger losses caused by the much higher current transported by each grid finger in the large area cell compared to small area record devices. The impact of local defects on cell performance could be reduced to less than 3% of the total power generated by the device as $j(V)$ curve analysis of 37 prototype devices revealed. This was mainly due to the substrate pre-treatment optimization which resulted in a highly reduced number of local shunts. The remaining scale-up loss we attribute to lateral non-uniformities of the absorber layer composition of the cell. Indications for such non-uniformities have been obtained by laterally resolved spectral response measurements and by thermography. Studies of arrays of small area test cells on a $8 \times 4 \text{ cm}^2$ substrates are underway in order to quantify this effect.

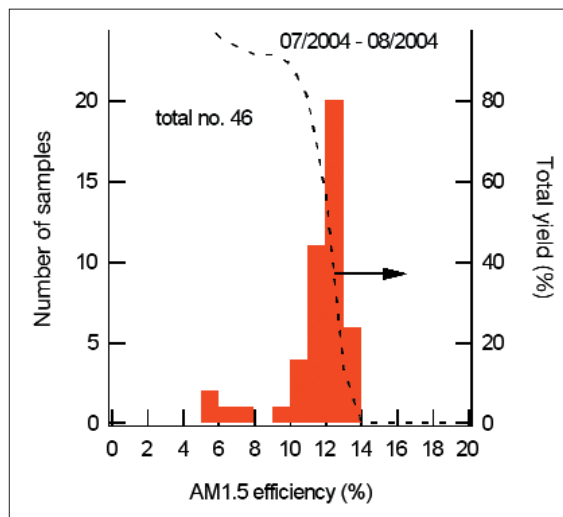


Fig. 2: Distribution of AM1.5 efficiencies of all processed 27.1 cm^2 devices of the Hahn-Meitner-Institut baseline over a period of two month. The narrow distribution reflects the high level of process reproducibility of the baseline process for flexible solar cells. The dashed line depicts the number of samples above a respective efficiency threshold value.

area [cm ²]	V_{oc} [mV]	j_{sc} [$\frac{\text{mA}}{\text{cm}^2}$]	ff [%]	η [%]
27.1	640	33.93	69.3	15.0
0.5	640	34.48	75.6	16.7

Table 1: Device parameters of best large area device (27.1 cm^2) on titanium foil under AM1.5 illumination (100 mW/cm^2). Parameters for a small area reference cell are included for comparison.

- [1] C. A. Kaufmann, A. Neisser, R. Klenk, R. Scheer, *Transfer of Cu(In,Ga)Se₂ thin film solar cells to flexible substrates using an in situ process control*, Thin Solid Films in press (2004)
- [2] A. Neisser, C. A. Kaufmann, R. Klenk, R. Scheer, M. A. Kroon, G. Oomen, H.-W. Schock, *Prototype Development – Flexible Cu(In,Ga)Se₂ Thin Film Solar Cells for Space Applications*, Proc. of 31st IEEE PVSC, Florida, 2005, accepted for publication

Corresponding author:

A. Neisser
axel.neisser@hmi.de

Hot electrons at the interface of p-InP

M. Neges, K. Schwarzburg, F. Willig

■ HMI, SE4

The theoretical limit for the efficiency of a photovoltaic converter operated under non-concentrated sunlight is 67%, whereas the limit of a single band gap solar cell is around 30% [1]. Conventional single junction solar cells simply cannot use the excess kinetic energy of those charge carriers created by the absorption of photons with energy greater than the band gap. Present physical models for solar cells ignore effects due to hot charge carriers and assume that all photo-generated carriers thermalize to the temperature of the crystal lattice prior to charge transport via diffusion and drift. However, if the thickness of the light-absorbing layer becomes smaller, this assumption is no longer valid. There is even the suggestion in the literature that a single band gap solar cell can approach the general efficiency limit of 67% [2] if all the hot carriers can be collected at an appropriate contact.

To obtain somewhat more quantitative data concerning dynamics of hot charge carriers at room temperature at low excess carrier densities, we carried out Monte Carlo simulations on *p*-type InP. The latter was selected as the model system, since relevant material parameters are available in the literature. Because of the small electron-hole effective mass ratio and the fast scattering rates for holes in *p*-type material, our modeling was restricted to the photo-generated electrons. Scattering with LO-phonons, acoustic phonons (deformation potential and piezoelectric), charged impurities, and holes was included in the model. Two geometries were considered for the light-absorbing layer. Firstly, a semi infinite half-space where the boundary acted as an ideal electron-collecting interface. This scenario (*bulk*) mimics the electrically neutral absorbing layer, comprising typically the whole wafer of a conventional pn-junction solar cell. The second structure (*slab*) was a 50 nm thin slab of InP:Zn, where the front and the back

side contacts were the electron collectors. This scenario is an approximation for a solar cell structure with several thin layers stacked or a cell consisting of large nm particles. Figure 1 shows the electron energy distribution for the *bulk* structure. The electron generation depth (10, 75, 750 nm) was varied and also the doping level (a: $N_A = 5E17 \text{ cm}^{-3}$, b and c: $N_A = 2E14 \text{ cm}^{-3}$, c with reduced LO-phonon scattering rate). From Fig. 1 it is evident, that the electron energy distribution is non-thermal even at room temperature unless the electrons are generated far away (750 nm) from the interface combined with a medium doping level. Thus, it is not possible to describe the actual energy distribution as a Maxwell-Boltzmann distribution at an elevated temperature. As can be expected, the deviations become the stronger the lower the electron-hole scattering rates (a→c). Figure 2 presents an analysis of the possible gain in energy conversion under different conditions. It shows the normalized energy flux at the interface under solar illumination conditions. The energy loss of hot electrons is small for the 50 nm thick *slab* structure, while the *bulk* absorber would be a bad hot-electron converter. In summary, the simulations demonstrate that hot carrier dynamics are important at the contact even at room temperature. The actual energy distribution of hot electrons must be determined using parameters characteristic for the specific material. It cannot be approximated by a thermal distribution at a high temperature. Hot carrier collection can become important in future generations of photovoltaic devices that incorporate thin layers or aim at utilizing hot carriers directly.

-
- [1] P. Würfel, T. Trupke, *Physik Journal* **2**, 45–51 (2003)
 [2] R. T. Ross, A. J. Nozik, *J. Appl. Phys.* **53**, 3813–3818 (1982)

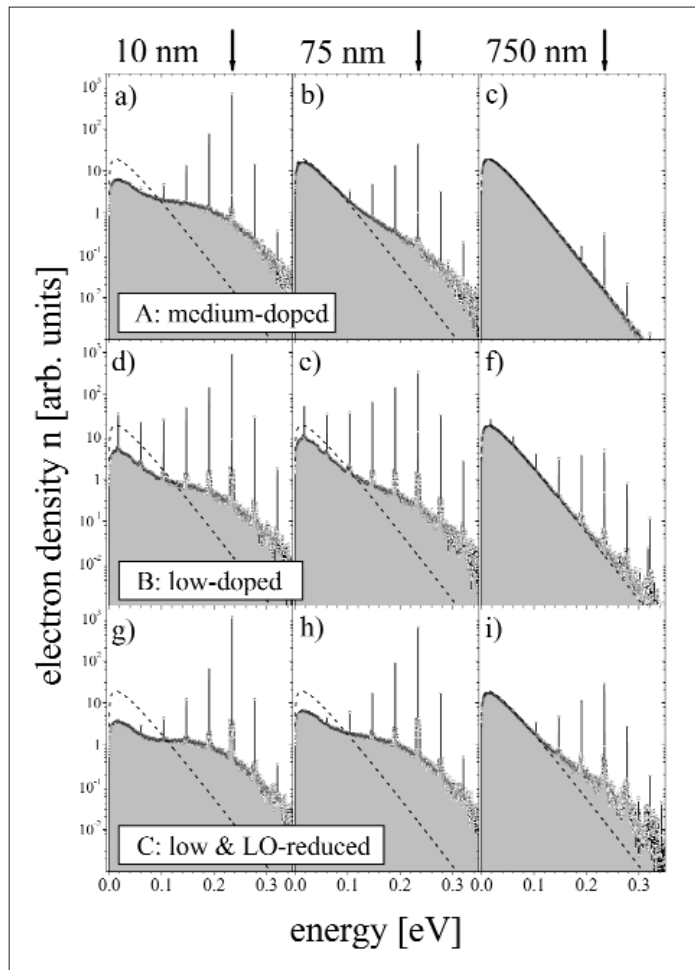


Fig. 1: Simulated energy distributions of the electron density in bulk-type InP:Zn at 300 K for electrons with generation depths of 10 nm (left), 75 nm (middle) and 750 nm (right). Each row corresponds to different material parameters (see text). The excitation energy is 234 meV above the conduction band minimum and is indicated by the arrows on top. Dotted lines show the corresponding Maxwell-Boltzmann distribution.

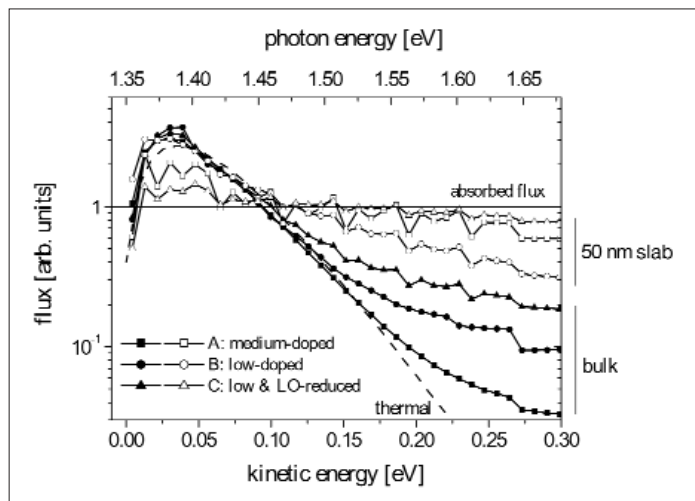


Fig. 2: Energy distribution of the total electron flux at the contact for the *bulk* scenario (closed symbols) and for a slab, 50 nm thick (open symbols). The distributions are normalized to the absorbed photon flux. The photon source was modeled as a black body with $T=5800$ K. For comparison also a thermal distribution is depicted.

Ultrafast electron dynamics measured with femtosecond two-photon photoemission

L. Gundlach¹, R. Ernstorfer¹, E. Riedle², R. Eichberger¹, F. Willig¹

■ 1 HMI, SE4 ■ 2 Biomolekulare Optik, LMU München

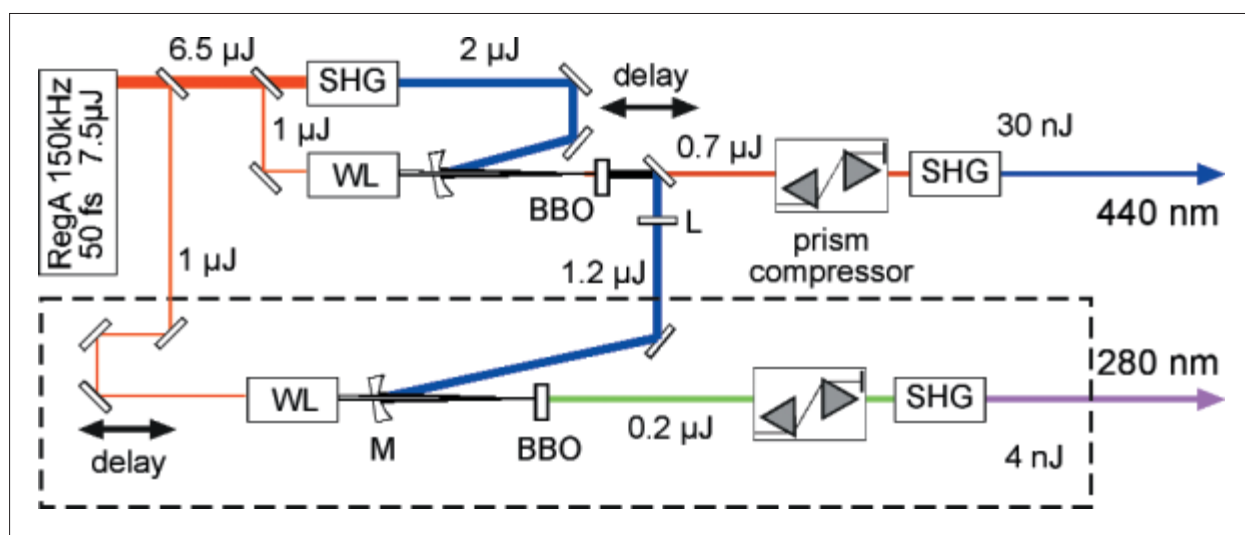


Fig. 1: Setup for two 150 kHz NOPAs pumped with one 400 nm SHG pulse (light blue). The second NOPA is shown inside the dashed box. The crosscorrelation of the output pulses is sub-30 fs.

Time-resolved two-photon photoemission (TR-2PPE) is the method of choice for investigating ultrafast photo-driven interfacial processes in the time domain, provided the respective interface can be exposed to ultrahigh-vacuum [1, 2]. The TR-2PPE measurement collects simultaneously information on the energy distribution of the photo-generated electrons and the time evolution of the intermediate state population near the interface. The 2PPE method offers unequaled sensitivity when compared with other pump-probe techniques, e.g. transient absorption, since the photoemitted electrons are counted directly by the detector. Hitherto, two different types of laser sources were employed for 2PPE measurements. On the one hand high repetition rate laser sources, i.e. systems operating at 100 kHz to MHz repetition rate were used, that deliver fairly long pulses with often limited wavelength tunability based on optical parametric amplification (OPA) for frequency tuning or harmonic generation. On the other hand low repetition rate laser sources with repetition rates up to 1 kHz and with a large number of photons per

pump pulse were employed. The latter systems allow only for slow signal accumulation, the superior noncollinear optical parametric amplification (NOPA) technology [3] can provide, however, extremely short and highly tunable pulses. Recently, tunable sub-20 fs ultraviolet pulses have been achieved with appropriate chirp management in the visible [4]. We report here on a significant improvement of the laser source for 2PPE measurements by adapting the NOPA scheme to operation at 150 kHz repetition rate. Furthermore, a second NOPA was operated simultaneously with one common pump system by utilizing the 400 nm pump pulse for the first NOPA again also in the second NOPA. This way two independently tunable ultrafast light sources are available (Fig. 1).

The improved tunability and shorter duration of the two laser pulses were tested in 2PPE measurements probing the lifetime of image potential states at Cu(111) and Ag(111) surfaces. Image potential states at metal surfaces have been studied extensively before [5]. The low-index surfaces of noble-metals exhibit a surface-projected bandgap centered at Γ (Fig. 2). An electron in front of such a surface is trapped by the induced image potential on one side and the bandgap on the other side. The resulting potential generates a Rydberg-like series of bound states in the direction of the surface normal. These states can be optically populated from the occupied surface state (SS) either resonantly or off-resonantly via quasi-elastic scattering. The main decay channel for the excited image potential state (IS) is governed by the overlap of the IS with the bulk. Earlier TR-2PPE studies by Schönlein et al. have proposed lifetimes of less than 20 fs for the $n=1$ and $n=2$ IS of Ag(111), respectively [6]. More recently, Lingle et al. have reported 32 ± 10 and sub-20 fs for the $n=1$ and $n=2$ IS of the same

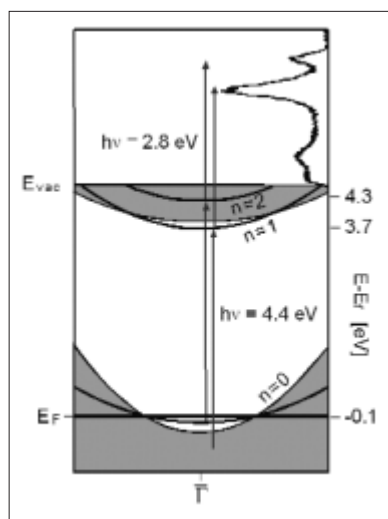


Fig. 2: Surface projected bulk band structure and dispersion of the $n=0$ surface state, $n=1$ and $n=2$ image potential state together with the TR-2PPE scheme for the Ag(111) surface. Effective electron masses and binding energies taken are from literature. The arrows indicate direct excitation from the $n=0$ surface state to the $n=2$ image potential state and indirect excitation from bulk states to the $n=1$ image potential state with photons $h\nu=4.4\text{ eV}$. The second pulse ($h\nu=2.8\text{ eV}$) generates the depicted kinetic energy spectrum of the photoemitted electrons.

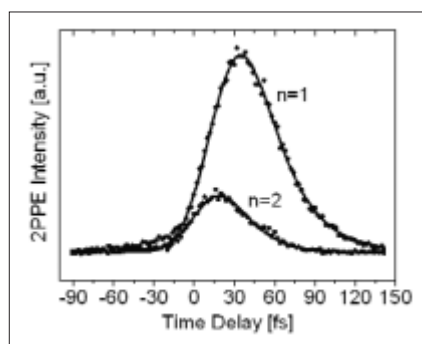


Fig. 3: Transient 2PPE signal for the $n=1$ and $n=2$ image potential state at Ag(111) together with the fitted curves obtained from the Bloch model. The lifetimes are 25 ± 2 fs and 18 ± 2 fs for the $n=1$ and $n=2$ image potential state, respectively.

system, respectively [7]. The pulse durations in the above experiments were up to six times longer than the reported lifetimes. The values had been extracted from the measurements by fitting the data with optical Bloch equations. This method relies on the exact knowledge of time zero, i.e. the time of maximum overlap between pump and probe pulse. With the improved laser setup described here, it was possible to obtain the IS lifetimes directly from the clear deviations of the measured signals from the crosscorrelation trace and to extract time constants as short as 12 fs by means of optical Bloch equations, as well as by fitting with a simple rate model (Fig. 3). The time scale of the thus measured lifetimes is in good agreement with values deduced earlier by other groups.

- [1] R. Haight, Surf. Sci. Rep. **21**, 275 (1995)
- [2] L. Töben, L. Gundlach, T. Hannappel, R. Ernstorfer, R. Eichberger, F. Willig, Appl. Phys. A **78**, 239 (2004)
- [3] G. Cerullo, M. Nisoli, S. De Silvestri, Appl. Phys. Lett. **71**, 3616 (1997)
- [4] P. Baum, S. Lochbrunner, E. Riedle, Appl. Phys. B **79**, 1027 (2004)
- [5] P. Echenique, R. Berndt, E. Chulkova, T. Fauster, A. Goldmann, U. Höfer, Surf. Sci. Rep. **52**, 219 (2004)
- [6] R. W. Schönlein, J. G. Fujimoto, G. L. Eesley, T. W. Capehart, Phys. Rev. B **43**, 4688 (1991)
- [7] J. R. L. Lingle, N.-H. Ge, R. E. Jordan, J. D. McNeill, C. B. Harris, Chem. Phys. **205**, 191 (1996)

Corresponding author:

L. Gundlach
gundlach@hmi.de

Improved structure and performance of the InP/GaAsSb interface in a resonance tunneling diode

Z. Kollonitsch¹, H.-J. Schimper¹, U. Seidel¹, K. Möller¹, S. Neumann², F.J. Tegude², T. Hannappel¹, F. Willig¹

■ 1 HMI, SE4 ■ 2 University Duisburg-Essen, Solid-State Electronics Department, Duisburg, Germany

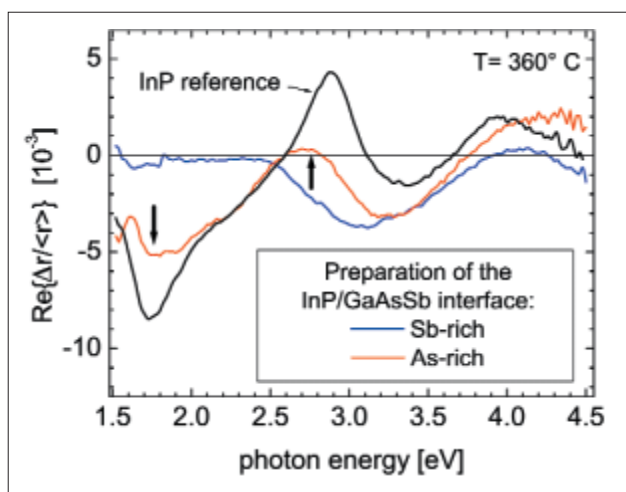


Fig. 1: Reflectance anisotropy (RA) spectra after InP was grown for 5 s (20–25 Å) on GaAsSb. The blue curve corresponds to InP growth on the Sb-rich GaAsSb(100)–(1×3) reconstruction, and the red curve to InP growth on the As-rich GaAsSb(100)–c(4×4) reconstruction. The black curve shows for comparison the spectrum of a homoepitaxially grown P-rich InP(100) surface.

A main challenge of metalorganic vapor phase epitaxy (MOVPE) and molecular beam epitaxy (MBE) process control is the improvement of III–V heterointerfaces. The InP/GaAsSb heterocontact is of interest for electronic devices based on the lattice constant of InP, e.g. multijunction solar cells, double heterojunction bipolar transistors, and resonance tunneling diodes (RTDs). Interfaces between an antimony (Sb) containing layer and a subsequent layer without Sb are known to suffer from Sb segregation [1]. It is still under investigation, how to reduce interdiffusion at the interfaces but most researchers would agree that control over the surface reconstruction of the Sb containing layer is a promising approach to reduce the Sb segregation. In a previous study on InAs/GaInSb heterointerfaces [1] Sb segregation was found quantitatively linked to the group V stoichiometry of the GaInSb surface reconstruction that served as the template for interface formation. Growth of InP on two different reconstructions of the GaAsSb(100) surface was investigated here, namely the Sb-rich (1×3) reconstruction and the As-rich c(4×4) reconstruction [2]. In the following the growth of InP on the Sb-rich (As-rich) GaAsSb(100) surface will be referred to as Sb-rich (As-rich) interface preparation.

The samples were prepared in an MOVPE reactor equipped with a patented exit for sample transfer into an ultrahigh vacuum (UHV) chamber [3]. The growth of the InP/GaAsSb heterointerface was monitored in the MOVPE environment with reflectance anisotropy/difference (RA/RD) spectroscopy. After transfer of the sample to UHV photoelectron spectroscopy (UPS/XPS) and low energy electron diffraction (LEED) were performed. The blue curve in Fig. 1 shows the in-situ RA spectrum after InP was grown for 5 s on the Sb-rich GaAsSb(100)–(1×3) reconstruction.

The RA spectrum is obviously very different from the reference RA spectrum of a homoepitaxially grown P-rich InP(100) surface (black curve). XPS and UPS measurements (not shown here) indicated that the group V elements intermix at the interface. The red curve in Fig. 1 shows the in-situ RA spectrum after InP was grown for 5 s on the As-rich GaAsSb(100)-c(4×4) reconstruction. Clearly, the red curve in Fig. 1 is much more similar to the black curve than the blue curve. This fact is attributed to the reduction in the interfacial diffusion of Sb. The peak at around 1.7 eV indicates that P-dimers are formed on the surface of InP [4]. The incomplete peak of the red curve at around 2.8 eV indicates intermixture of group V atoms in the second and third layer at the interface [4]. In conclusion, the As-rich preparation of the interface leads to an improved InP layer growth on GaAsSb compared to the Sb-rich preparation of the interface.

RTDs were prepared (upper panel in Fig. 2) in order to compare the electronic behavior of the Sb-rich and As-rich interface preparations. The preparation of the two RTDs was identical except for the Sb- versus As-rich termination of GaAsSb. The functionality of *p*-type RTDs is based on quantum mechanical tunneling of charge carriers through a double barrier in the valence band [5]. Each InP-barrier had a thickness of 7 nm. The nonlinear current-voltage (*I*-*V*) characteristic is sensitive to the quality of the interfacial layers. The *I*-*V* characteristics of the RTD with the differently prepared interface display the symmetry with respect to the sign of the voltage (center and lower panel in Fig. 2). Non-symmetric *I*-*V* curves are attributed to poor interfacial layers. Clearly, the RTD with the As-rich prepared interface showed a more symmetric *I*-*V* characteristic than that with the Sb-rich interface.

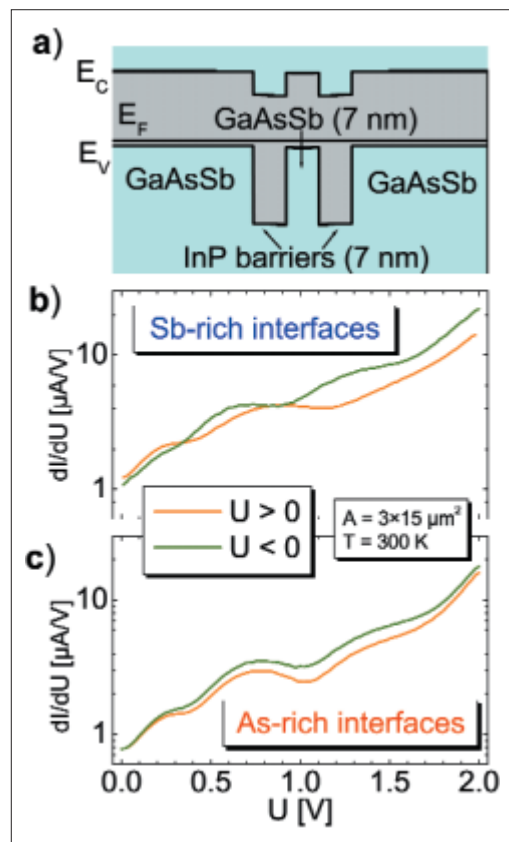


Fig. 2: a) Band diagram of the active region of the InP/GaAsSb *p*-type RTD. b) Non-symmetric *I*-*V* curves for the RTD with the Sb-rich InP/GaAsSb interfaces. c) Less non-symmetric *I*-*V* curves for the RTD with the As-rich InP/GaAsSb interfaces.

- [1] J. Steinshnider, J. Harper, M. Weimer, C.-H. Lin, S. S. Pei, D. H. Chow, *Phys. Rev. Lett.* **85**, 4562 (2000)
- [2] Z. Kollonitsch, K. Moller, F. Willig, T. Hannappel, *J. Cryst. Growth* **272**, 694 (2004)
- [3] T. Hannappel, S. Visbeck, L. Töben, F. Willig, *Rev. Sci. Instrum.* **75**, 1297 (2004)
- [4] C. Castillo, B. S. Mendoza, W. G. Schmidt, P. H. Hahn, F. Bechstedt, *Phys. Rev. B* **68**, 041310(R) (2003)
- [5] J. F. Lampin, F. Mollot, *Appl. Phys. Lett.* **71**, 1080 (1997)

Corresponding author:
Z. Kollonitsch
kollonitsch@hmi.de

Reactive magnetron sputtering of CuInS_2 : a new prospective deposition method for thin film solar cells?

T. Unold, K. Ellmer

■ HMI, SE5

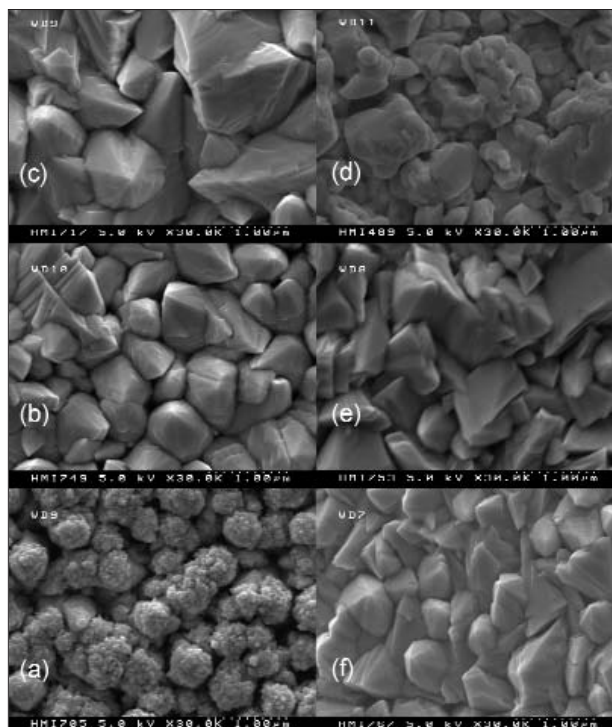


Fig. 1: REM images of CuInS_2 films prepared by reactive magnetron sputtering at different temperatures T_s and different Cu/In ratios r . **a)** $T_s=350^\circ\text{C}$, $r=1.1$ **b)** $T_s=420^\circ\text{C}$, $r=1.1$ **c)** $T_s=500^\circ\text{C}$, $r=1.1$ **d)** $r=2.3$, $T_s=500^\circ\text{C}$ **e)** $r=1.0$, $T_s=500^\circ\text{C}$ **f)** $r=0.9$, $T_s=500^\circ\text{C}$

Thin-film chalcopyrite solar cells are usually prepared by coevaporation or by a sequential process consisting of sputtering of the metal precursors followed by a sulfurization or selenization and recrystallization step at about 500°C [1]. For a large-scale production of thin-film solar cells a direct one-step deposition process of the absorber layer would be advantageous, allowing for an in-line deposition of all solar cell layers [2]. Magnetron sputtering is a well established deposition method, which allows for low temperature thin film growth on large areas. In fact, millions of square meters per year of architectural glass are being coated using magnetron sputtering at the present.

So far there have been very few studies investigating the deposition of electronic device-quality semiconductor materials by magnetron sputtering. Because of the sensitivity of electronic devices to even small (ppm) amounts of defects the requirements for the sputtering process in this case are much more stringent than in the case of optical coatings, where the main requirement is uniformity. In particular, the presence of high energy ions in the sputtering plasma pose a difficult challenge, since they may create structural and electronic defects in the growing film.

We have deposited CuInS_2 absorber layers by reactive magnetron sputtering from metallic copper and indium targets in an $\text{Ar-H}_2\text{S}$ atmosphere. In order to optimize the reactive sputtering process for our films, the substrate temperature, $\text{H}_2\text{S-Ar}$ ratio and Cu/In ratio have been systematically varied. The structural, optical as well as the solar cell properties were analysed by Raman spectroscopy, photoluminescence, Scanning Electron Microscopy (SEM), current-voltage and quantum efficiency measurements.

In Fig.1 we show SEM images for films sputtered at 3 different substrate temperatures, T_s , and three different Cu/In ratios ranging from $0.9 \leq \text{Cu/In} \leq 2.3$. For the films with $r = \text{Cu/In} \sim 1.1$ the film morphology changes considerably when the substrate temperature is raised from 350°C to 500°C . Whereas the film deposited at low temperature is very porous and *cereals-like*, the films become more dense and of columnar morphology at higher temperatures. Typical grain sizes evolve from about 350 nm at 420°C to about 1 micrometer at 500°C . Similarly for films grown at $T_s=500^\circ\text{C}$, the films become increasingly more dense with decreasing Cu/In ratio. This change in morphology is accompanied by a change in the structural phases present in the film as seen in the Raman spectra shown in Fig.2. The film grown at 350°C , shows very broad spectral features and in particular a strong signal due to the CuIn_3S_8 phase at 340 cm^{-1} which is found not to be helpful for

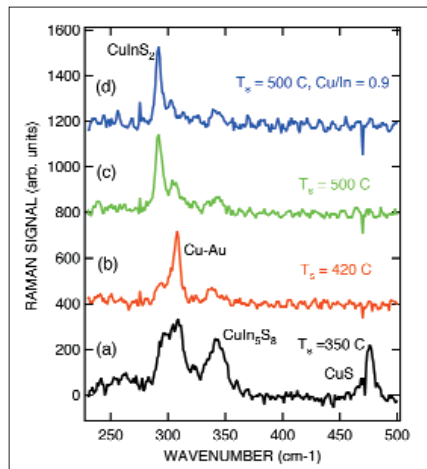


Fig. 2: Raman spectra for three copper rich films and one indium-rich film.

a) $T_s = 350^\circ\text{C}$, $r = 1.1$ **b)** $T_s = 420^\circ\text{C}$, $r = 1.1$
c) $T_s = 500^\circ\text{C}$, $r = 1.1$ **d)** $r \sim 0.9$, $T_s = 500^\circ\text{C}$

good solar cell performance. The film grown at 420°C shows a dominant CuInS_2 resonance around 300 cm^{-1} , however not the one corresponding to the chalcopyrite ordering, but rather to a Cu-Au defect ordering [3]. In previous work this defect ordering has been correlated with a deteriorated solar cell performance. The spectrum for the film grown at 500°C is dominated by the chalcopyrite resonance at 294 cm^{-1} with only small amounts of the defect ordering phase noticeable. These three films have been grown with a $\text{Cu/In} \sim 1.1$ (corresponding to Fig. 1a–c). On the top of the graph we show an indium-rich deposited film ($\text{Cu/In} \sim 0.9$, $T_s = 500^\circ\text{C}$). It can be seen that now the chalcopyrite mode is even a bit more pronounced. This result has been surprising considering previous results obtained for coevaporated and sequentially processed films, where $\text{Cu/In} \leq 1$ always led to an increased defect ordering. The fact that we observe the opposite points to some fundamental differences in the reactive sputtering growth process compared to the evaporation process. Stoichiometric or indium-rich deposition of CuInS_2 absorber layers would be desirable because it would eliminate the need for the KCN etching step currently used to remove the CuS surface layer present on copper-rich films.

We have also measured the photoluminescence properties of our films to get an estimate of the electronic quality of the reactively sputtered absorber layers. The photoluminescence measurements revealed level spectra very similar to the spectra found for films from the standard sequential and coevaporation processes. This indicates that the presence of ion bombard-

ment in the reactive sputtering process does not introduce fundamental qualitative changes to the defect structure of the films.

Solar cell devices have been produced from our optimized absorber layers, utilizing the Hahn-Meitner-Institut baseline processes consisting of a KCN etching step, a chemical bath deposition of the CdS buffer layer and magnetron sputtering of the ZnO top contact. The results for our best cell are presented in Fig. 3 showing an efficiency of $\eta = 8.8\%$, a short circuit current of 23 mA and an open-circuit voltage of 650 meV . Although this efficiency is still somewhat lower than the best efficiencies found for the sequential and the coevaporation processes ($\eta \sim 12\%$), it is nevertheless a promising step toward the goal of a solar cell exclusively prepared by sputtering processes. In our study we have not identified principle obstacles to the magnetron sputtering deposition of device-quality semiconducting films. Rather, the directly sputtered absorber films seem to show an improved film morphology, consisting of columnar grains without large voids and a relatively smooth surface. At the moment the efficiency of our devices is mainly limited by the open-circuit voltage of approximately 650 meV . We think that this is due to defects at the $\text{CuInS}_2/\text{CdS}$ hetero-interface, possibly caused by ion bombardment in the sputtering process. We are currently investigating further optimizations and changes to the magnetron sputtering process to overcome this limitation.

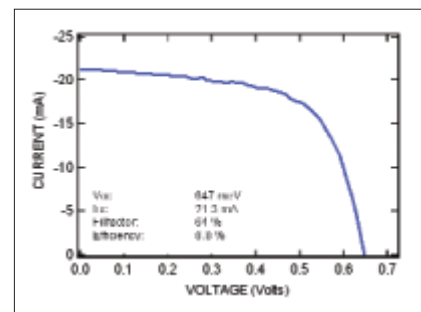


Fig. 3: AM1.5 illuminated current voltage characteristic for a ZnO/CdS/CuInS₂/Mo solar cell prepared by reactive sputtering, $T_s = 500^\circ\text{C}$, $r \sim 1.1$.

- [1] J. Klaer, *et al.*, *Efficient CuInS₂ Thin Film Solar Cells Prepared by a Sequential Process*, *Semicond. Sci. Tech.* **13**, 1456 (1998)
- [2] T. Unold, J. Hinze, K. Ellmer, *CuInS₂ Absorber Layers and Solar Cells Deposited by Reactive Magnetron Sputtering from Metallic Targets*, 19th Europ. Photovolt. Sol. En. Conf. (2004) Paris, 1917
- [3] J. Alvarez-García *et al.*, *Raman scattering structural evaluation of CuInS₂ thin films*, *Thin Solid Films* **387**, 216 (2001)

Corresponding author:

T. Unold
 unold@hmi.de

Surface passivation of MoS₂ or WSe₂ for optimised photoconversion efficiencies

T. Moehl, H. Tributsch

■ HMI, SE5

Photoelectrochemical microwave reflectivity measurements offer a deep insight into the interface between semiconductor and electrolyte. In addition to the light induced excess charge carriers that reach the external circuit and are detected via the photocurrent the microwave reflection simultaneously provides information about the photo-induced excess charge carriers which remain in the semiconductor. In this way it is possible to directly observe the influence of surface changes on the excess charge carriers at the interface and thus on photovoltaic quality [1].

The aim of this project is the passivation of surface states in layered type semiconductors like molybdenum disulfide (MoS₂) or tungsten diselenide (WSe₂). These compounds exhibit promising characteristics for the application in thin film solar cells [2]. They have high adsorption coefficients (up to $3 \cdot 10^5 \text{ cm}^{-1}$) with energy gaps of 1,2 to 1,7 eV. Single crystals of WSe₂ gave energy conversion efficiencies of 17% in wet iodine-iodide solar cells [3]. The crystal structure is strongly anisotropic revealing a chemical inert van der Waals surface perpendicular to the *c*-axis and a highly reactive surface consisting of unsaturated bonds parallel to the *c*-axis (Fig. 1). Like graphite these crystals have electronically and chemically diverse attributes depending on which surface is investigated.

The unsaturated bonds of molybdenum are held responsible for unfavoured side reaction of charge carriers. The first steps of (photo)corrosion of these crystals in aqueous electrolyte is starting at those and the recombination of light induced excess charge carriers is mainly taking place at unsaturated bonds at the crystal edges. In order to develop solar cells based on this compounds, single or polycrystalline, understanding of the behaviour of the unsaturated bonds at the crystal edges is necessary.

Tween 80 and related compounds possess a long aliphatic side chain at a sorbitol ring. The other alcoholic groups of the condensed Hexose are substituted by poly-oxo-ethylenic groups. This molecule intercalates with its hydrophobic group in between the van der Waals layers (which could be demonstrated by XRD) and the polar oxo groups interact with the unsaturated bonds at the crystal edges (Fig. 1). The effect of the modification could be clearly detected in the change of the photocurrent and the microwave reflection (Fig. 2).

Figure 2 shows the enhancement of the photocurrent (solid line) after the modification with Tween 80, which also starts at a lower potential vs. SCE (Saturated Calomel Electrode) because of the suppressed surface recombination. This is supported by the measured microwave reflection (dashed line) which indicates lower surface recombination by an earlier rise of the signal after the adsorption of Tween 80 ($\Delta V \approx 100 \text{ mV}$) and more accumulated excess charge carriers in the range of the steady state photocurrent ($V > 700 \text{ mV}$). The results show that Tween 80 blocks the adsorption sites for water and reduces the surface states induced by the dangling bonds.

On the way to polycrystalline solar cells out of MoS₂ and related layered compounds the understanding of the interaction of different functional groups of adsorbates with the crystal edges has to be understood. The impact of adsorbates on corrosion, recombination and charge transfer can be tested and studied by the simultaneous measurement of photocurrent and microwave reflection.

-
- [1] G. Schlichthorl, H. J. Lewerenz, *Journal of Electroanalytical Chemistry* **443**, 9–31 (1998)
- [2] *Photoelectrochemistry and Photovoltaics of Layered Semiconductors*; edited by A. Aruchamy; Kluwer Academic Publishers (Dordrecht, 1992)
- [3] O. N. Srivastava, G. Prasad, *J. Phys. D: Appl. Phys.* **21**, 1028–1030 (1988)

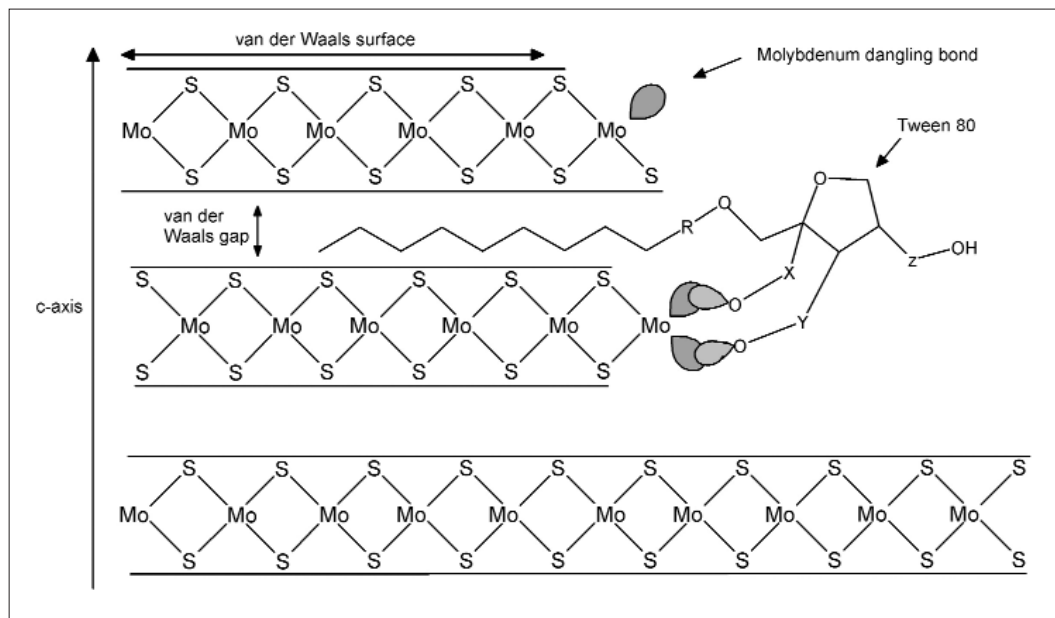


Fig. 1: Schematic figure of the different crystal surfaces in MoS₂ and possible adsorption mechanism of Tween 80 and related compounds (X, Y and Z are side chains of the $-(O-CH_2-CH_2)-$ type with different lengths).

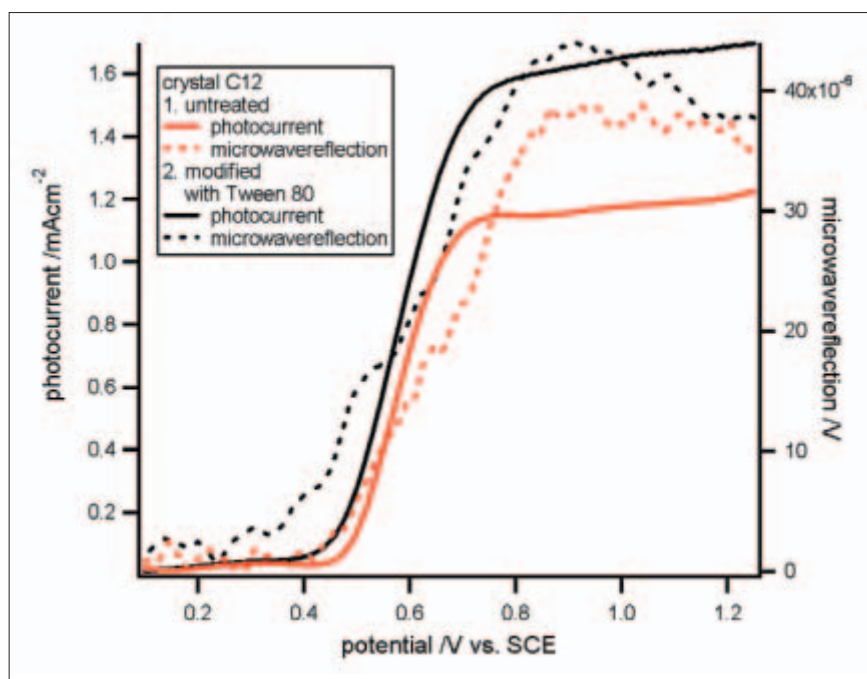


Fig. 2: MoS₂ (crystal charge c12) before and after the modification with Tween 80 (5 wt% aqueous solution for 15 h) under 8,7 mW/cm² halogen illumination in 0,5 M K₂SO₄ with 0,2 M K₃/K₄[Fe(CN)₆] and 20 mV/s cycle speed.

Polymer electrolyte membrane (PEM) fuel cells: new catalysts and bionic aspects

H. Tributsch, S. Fiechter, P. Bogdanoff

■ HMI, SE5

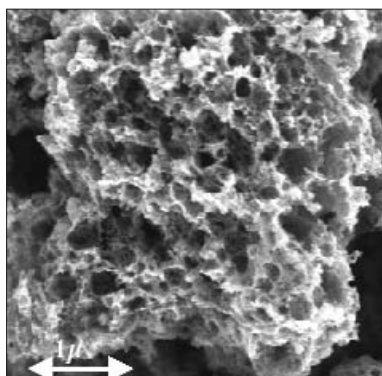


Fig. 1: Sponge-like catalyst prepared by pyrolysis of a cobalt porphyrin in the presence of iron oxalate.

Nature's regenerative strategy: Examples for bionic research.

Nature's regenerative strategy can be considered as a close example for a sustainable energy supply in a future industrial society. Striking natural phenomena are the light induced water splitting, the attachment of hydrogen to hydrocarbons as energy carriers and the reversible conversion of these chemical energies into a variety of other forms of energy, determining the activity of life. It is remarkable that

nature always utilizes electro-chemical energy as an intermediate in primary as well as secondary processes. It has to be emphasized that many complex energy-converting reactions can be catalyzed at ambient temperature or at low body temperature.

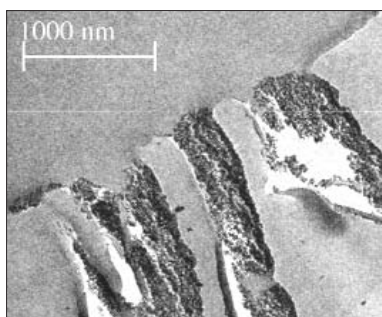


Fig. 2: Cross section of a polyethylene terephthalate (PET) membrane with pores filled with silica particles, the surface of which are covered by the proton-conducting amino acid layer (Lysin).

The aim of energy bionics is to learn from nature's energy technological paradigms. Prior to a technical application the natural mechanisms to be imitated have to be understood in detail. One conversion mechanism, nature has realized, concerns the effectiveness we know from fuel cells, i.e. the conversion of chemical into electrical energy. This active principle has already been realized in power plants of cells, the so-called mitochondria. Fuel cells consume oxygen for the same energy reason as human

beings in their respiration process.

The following cost-intensive components in PEM fuel cells were chosen to work out bionic solution strategies:

- replacement of platinum as electro-catalyst,
- development of alternative proton-conducting membranes,
- availability of hydrogen.

Catalysts without noble metals.

Contrary to technical catalysts, frequently utilizing noble metals, nature has solved catalyst issues by applying abundant transition metals working at low temperatures. Cytochrome oxidase is a typical example demonstrating the conversion of oxygen into water as it occurs in fuel cells. Nature manages with iron, cobalt and copper centers, which become effective in an adapted molecular environment. It is eye catching that the metal centers in biological catalysts are surrounded by nitrogen, as it is the case in porphyrins or in the heme-groups (hemoglobin, myoglobin, different cytochromes). In the electron transferring B12 vitamin, cobalt is present in a similar nitrogen ligand field. Since single metal centers are not able to store several electrons at least two centers are coupled with each other allowing a fast and cooperative supply of electrons. These natural catalysts are distinguished by saturation of all kinds of bonding possibilities to protect themselves against oxidation processes.

The main bionic challenge is to maintain the central part of the catalytic center, replacing the organic environment (protein matrix) by inorganic groups. This is achieved by integrating the cores of iron and cobalt porphyrins in a nearly amorphous graphite matrix. To obtain a highly active surface iron oxalate was added as a foaming agent in the preparation process. By this means, the metal-nitrogen environment essentially remained unchanged. Figure 1 shows a transmission electron micrograph of a sponge-like catalytic particle with integrated cobalt-nitrogen cores. Even though the metal content of the catalysts is small (1–2 wt%) the catalytic activity is comparable to that of platinum [1].

Proton-conducting membranes.

In PEM fuel cells expensive proton-conducting membranes on the basis of polytetrafluoro-ethylene-sulfonates (NAFION) are used. To find a natural analogon, mechanisms of proton con-

ductivity in nature have to be considered. In bacteriorhodopsin, for example, protons are conducted in channels, which are lined by amino acids. In a first approach, to mimic a bionic membrane, commercially available porous membranes have to be modified. From nanotechnology it is known that 15 nm sized silica particles can be attached at the surfaces of polymer channels. On the other hand, amino acids can be bonded via amino- or carboxyl-groups to the silica. Impregnating porous membranes by silica- and amino acid-containing solutions under vacuum, channels in the membranes were lined with amino acids as seen in the cross section of a transmission electron micrograph in Fig. 2. It could be demonstrated that these modified membranes exhibit protein conductivity in the order of commercial NAFION-membranes. Best results were obtained employing the amino acid lysine and porous polyethylene terephthalat (PET) [2].

Tandem membrane for direct solar hydrogen evolution

In the process of photosynthesis plants do not collect current but convert light via electrochemical energy directly to fuel. While the direct photo-induced generation of fuels was seriously discussed after the first energy crisis in the seventies of the last century the efforts to learn from nature in this respect were superseded by the prospect of very cheap solar cells. However few research initiatives investigated the feasibility to collect sufficient energy in serially switched photovoltaic structures via two electron excitation to directly generate hydrogen from water omitting current collection and without use of a specialized electrolyser. The record in this field, obtained with the collaboration of our research group, achieved a solar efficiency of 18% concerning hydrogen evolution utilizing a tandem solar cell of 20% efficiency [3]. This result shows that 90% of the photovoltaic energy can directly be converted into hydrogen applying adjusted catalysts. This yield is impressive when compared with the efficiency of photosynthesis cultivating sugar cane where even at three harvests per year only an mean efficiency of 0.5% can be obtained related to the conversion of light into chemical energy in form of biomass. However, the solar cell structures used based on the semiconductors gallium arsenid and silicon cannot be put offhand in contact with water. Therefore, to technically realize a photosynthetic membrane materials are in demand which are reactive in water, but at the same show long term stability.

It is well known for 30 years that TiO_2 absorbing ultraviolet light from the sunlight can oxidize water under oxygen evolution. During this process che-

mical radicals will be formed that can also be used to oxidize organic molecules to CO_2 and water. This property has been used in the last time with increasing interest to produce self-cleaning surfaces. Recently, as it was reported that carbon- and nitrogen-doped TiO_2 layers can shift the photosensitivity in the range of visible light it seemed to be time for the development of a water stable membrane mimicking photosynthesis. Figure 3 shows the concept pursued at the Hahn-Meitner-Institut. A titanium foil is oxidized at the one side adding an appropriate dopand and a suited catalyst. At the other side of the foil a simplified CuInS_2 solar cell is deposited by reactive sputtering. Replacing the highly conductive ZnO layer by TiO_2 no current collecting layer is any more necessary. In this way a membrane is available which is confined at both sides by a thermo-dynamically stable TiO_2 layer. Electrons extracted from water at the one side will be excited in two steps in the TiO_2 and the CuInS_2 layer passing to the opposite side where they will react with water under evolution of hydrogen. Unfortunately, the shift of the band gap of carbon- and nitrogen-doped TiO_2 layers in the visible range allowing water oxydation at lower energies could not be verified in our own electrochemical investigation using Differential Electrochemical Mass Spectroscopy (DEMS) [4]. Therefore, further research activities are needed to tailor an adapted oxide material with suitable band gap for this in principle functioning type of fuel generating photovoltaic membrane.

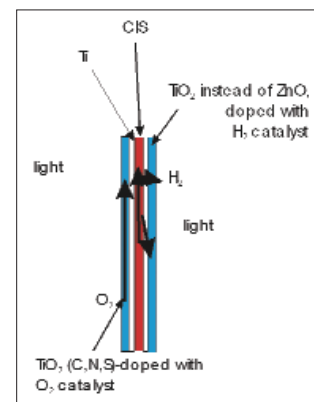


Fig. 3: Photosynthetic membrane composed of two confining TiO_2 layers, a titanium foil as substrate and a light absorbing CuInS_2 layer.

- [1] P. Bogdanoff, I. Herrmann, M. Hilgendorff, I. Dorbandt, S. Fiechter, H. Tributsch, *New Materials for Electrochemical Systems*, **7**, 85–92 (2004)
- [2] H.-J. Leem, J. Rojas-Chapana, S. Fiechter, H. Tributsch, *Bio-Analogue Amino Acid Lined Proton Conducting Channel for Fuel Cell Membranes*, in prep.
- [3] S. Licht, B. Wang, S. Mukerji, T. Soga, M. Umeno, H. Tributsch, *Efficient Solar Water Splitting, Exemplified by RuO_2 -Catalyzed AlGaAs/Si Photoelectrolysis*, *J. Phys. Chem. B* **104**, 8920–8924 (2000)
- [4] B. Neumann, P. Bogdanoff, H. Tributsch, S. Sakthivel, H. Kisch, *Electrochemical Mass Spectroscopic and Surface Voltage Studies of Catalytic Water Oxidation by Undoped and Doped Titania*, *J. Phys. Chem B.*, handed in

Corresponding author:

H. Tributsch
tributsch@hmi.de

Spectromicroscopy: investigating the ALILE process

W. Bremsteller¹, C. Lehmann¹, T. Plake¹, C. Pettenkofer¹, J. Schneider², J. Klein², M. Muske², S. Gall²

■ 1 HMI, SE6 ■ 2 HMI, SE1

Thin crystalline silicon solar cells have the potential for very high efficiencies. This has been shown by the preparation of a solar cell with an efficiency of 21.5% on a thinned-down monocrystalline Si wafer [1]. Unfortunately this is not a real Si thin-film but still a Si wafer technology. It is expected that only real Si thin-film manufacturing, which uses for example large-area glass substrates, can lead to a significant cost reduction on a long term. Such a thin-film technology requires the preparation of Si layers on glass with high structural and electronic quality by an industrially applicable process. The use of glass limits the processing temperatures to about 600°C. Thus, much interest has been focussed on amorphous Si (a-Si) as a precursor for polycrystalline Si (poly-Si) in a solid phase crystallization process which involves annealing temperatures of about 600°C. The use of metals can be favourable to achieve lower annealing temperatures as well as larger grain sizes. Nast *et al.* have demonstrated that aluminium-induced crystallization (AIC) of a-Si can be used to prepare large-grained poly-Si films on glass by annealing a glass/Al/a-Si stack and thus transforming it into a glass/poly-Si/Al+Si stack, as depicted in Fig. 1 [2]. Hence, it is called Al-induced layer exchange (ALILE) process.

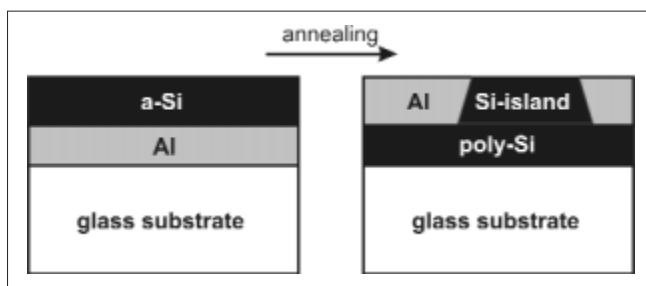


Fig. 1: Schematic of the ALILE process

The ALILE process can be easily observed in-situ in an optical microscope (e.g. [4]). However, it remains an open task to distinguish the grown structures by their chemical composition, i.e. to observe the annealing process in some kind of spectromicroscopy. At the Berlin electron synchrotron facility BESSY, we are able to resolve the chemical constituents of a sample surface using our photoemission electron microscope (PEEM) [3]. Hereby, electrons excited by a monochromated light beam having an energy of at least the sample's work function are emitted from the sample surface and subsequently imaged as in conventional electron microscopy. In the image plane, a microchannel plate is mounted to render the impinging electrons visible. An additional energy filter in the microscope column allows a selection of the electrons by their kinetic energy. In combination with monochromated x-ray light up to $h\nu=1000\text{eV}$ as provided by the BESSY undulator beamline U49/2 we were able to compose the PEEM image only of core electrons of the selected chemical species.

With the equipment at hand, we were able to study the ALILE process. Prior to PEEM investigations, the samples were inserted into the preparation chamber and Ar^+ sputtered for 90 min to remove the oxide from the a-Si top layer. Subsequently, a complete ALILE annealing process was carried out at 460°C for about 12 hours. Figure 2 presents the resulting sample surface contrast in the photoelectron micrographs. In Fig. 2a bright islands are visible which are areas of $\text{Si}2p$ photoelectron emission, i.e. those Si islands shown in Fig. 1. In a complementary fashion, the $\text{Al}2p$ emission stems from the area around the Si islands (Fig. 2b). Thus, we have found direct evidence for the chemical composition of the stack top layer after the layer exchange due to annealing.

Since XPEEM is able to produce integral real-time images within its field of view we were interested in the time-dependent change of the sample surface as the annealing process takes place. Figure 3 depicts a series of PEEM spectromicrographs generated with an excitation energy of $h\nu=200.0$ eV. The detection energy of the microscope is alternately set to Al2p (binding energy $E_B=74.1$ eV) and Si2p ($E_B=99.5$ eV). As the temperature is gradually increased from room temperature to a maximum of 380°C over a period of 3 hours, the homogeneously bright Si2p image starts to exhibit randomly distributed dark islands, i.e. areas with absence of Si (cf. t_0 , Fig. 3). Changing the detection energy to Al2p emission these islands can be clearly identified as Al. Initially, the diameter of those features is in the order of $1\ \mu\text{m}$. From only a few of these islands Al starts to spread laterally until the Si is dissolved (t_0+35 min, Fig. 3). The compact silicon islands detected in Fig. 2 would be formed upon persistent annealing due to Oswald ripening.

While optical microscopy is limited in resolution and to reflection analysis of the samples XPEEM offers much higher resolution of only a few nanometers as well as direct access to the chemical composition of the surface layer. We have succeeded in laterally resolved direct analysis of the chemical composition during an ALILE annealing process. The observations carried out demonstrate the vast potential of the photoemission electron microscope opera-

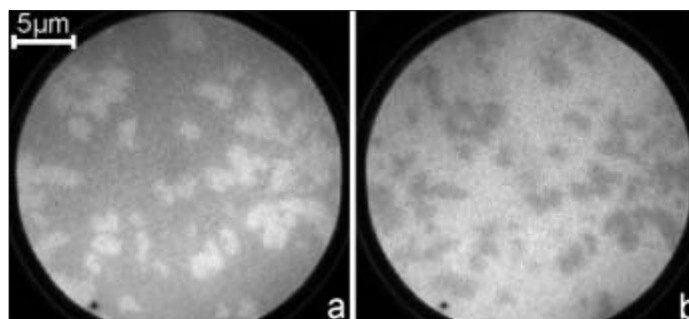


Fig. 2: Complementary photoelectron micrographs of a glass/300 nm Al/375 nm a-Si stack annealed for about 12 hours at 460°C . Bright areas represent (a) Si2p, (b) Al2p core level emission.

ted at the Berlin electron synchrotron to determine the chemical constituents and their lateral distribution in the surface of a planar sample. Having started with the investigation of the ALILE process we are certain that a number of groups will benefit from our PEEM analysis experimental setup in the future.

-
- [1] J. Zhao, *et al.* in: Proceedings of the 13th European Photovoltaic Solar Energy Conference, Nice, France, 1566 (1995)
 [2] O. Nast, *et al.*, Appl. Phys. Lett. **73**, 3214 (1998)
 [3] <http://www.elmitec.de/html/peem.html>
 [4] J. Schneider *et al.*, J. Non-Cryst. Solids **338–340**, 127 (2004)

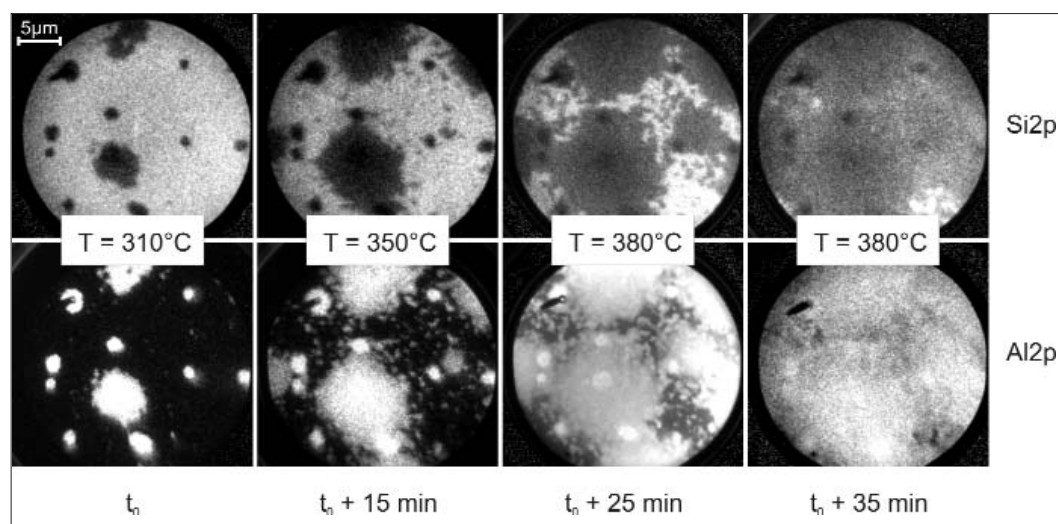


Fig. 3: ALILE process of a 300 nm Al/375 nm a-Si stack on glass during a period of 35 minutes. In the upper/lower row, bright areas correspond to Si2p/Al2p core level emission.

Corresponding author:

T. Plake
 plake@hmi.de

Band structure and effective masses for CuInS₂

C. Lehmann, W. Calvet, T. Plake, R. Hunger, C. Pettenkofer

■ HMI, SE6

Understanding the interface properties in heterogeneous solar cell junctions demands a firm understanding of the electronic structure of the materials involved. CuInS₂ is used as an absorber material in thin film cells. However, only little experimental work is reported on the valence band structure of chalcopyrites [1]. For example, it is possible to deduce the effective mass m^* from the valence band curvature. Along with the bulk band structure, one is also interested in the occurrence of surface states which may play a key role for the formation of intergap states at the interfaces of such a device.

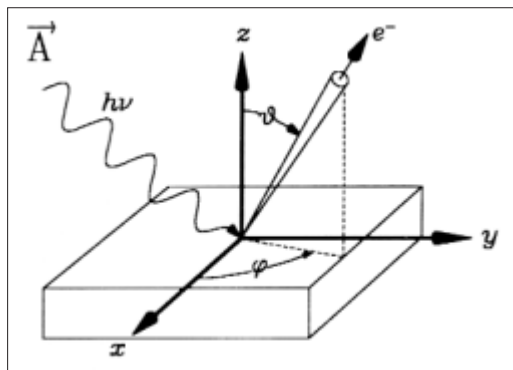


Fig. 1: Illustration of angle resolved photoemission spectroscopy

Angle resolved photoemission spectroscopy (ARPES) is the technique of choice to map the band structure of conductive solid states such as metals and semiconductors. In principle, an electron energy analyser is scanned across the half space of the sample surface which emits photoelectrons excited by an ultraviolet monochromated light source. For the latter, synchrotron radiation is desirable since it provides high photon flux, variable energies, and a well-defined polarisation vector. ARPES requires the knowledge of the crystal orientation, which can be determined by low-energy electron diffraction (LEED). Thus, one can scan the electron analyser stepwise along lines of high symmetry. For each step a kinetic energy spectrum of the photoexcited valence electrons is recorded.

From the position of the emission maxima and the detection angles (cf. φ and θ in Fig. 1) the valence band structure can be deduced.

At the Berlin electron synchrotron laboratory (BESSY) we run an ARPES machine (ADES/SoLiAS) at the TGM7 beamline with energies ranging from 6 eV to 35 eV and 25 eV to 120 eV. The experimental setup consists of several modules for preparation, sample treatment and analysis under ultrahigh vacuum (UHV) conditions.

One of the major difficulties in CuInS₂ is to obtain well-defined, smooth and clean crystal surfaces. We have chosen a cleaving method in UHV, which may be an elaborate task since only one out of ten samples yields satisfying results. However, the advantage of this procedure is to obtain pure and unstrained crystal surfaces which allow direct comparison with theoretical band structure calculations (e.g. [2]). For this work, we used CuInS₂ crystals that were grown in a Bridgeman process. Crystal-lites at a size of the order 5 mm × 5 mm × 5 mm were glued to the sample holder and cleaved in UHV.

Once a sample has been successfully cleaved it is checked by LEED for both the crystal quality and orientation. With this information, the sample is brought into position for photoemission spectroscopy. Figure 2 depicts a series of photoemission spectra for scanning from (112) to (110) direction at excitation energies of $h\nu = 20$ eV and $h\nu = 27$ eV. Hereby, the (inverted) second derivatives of the spectra are merged into a colour scale plot to facilitate a visible impression of the valence band structure. Values for k have been obtained via the equation

$$k_{\parallel} = \sqrt{\frac{2m_e}{\hbar^2} E_{kin}} \sin\theta \quad m_e = \text{electron mass}$$

The band closest to binding energy $E_B=0\text{ eV}$ is the valence band edge with a maximum at the Γ point, i.e. for a vanishing component of the k vector parallel to the sample surface ($k_{\parallel}=0$). Between binding energies of 2 eV and 5 eV, a number of highly dispersive bands can be seen. According to theory, those bands originate from Cu3d and S3p states. Separated at about $E_B=7\text{ eV}$, In-S bonds form a common band. Since the excitation energy is varied in both plots, the vertical component k_{\perp} of k is effected as well. Thus, both plots represent different cuts through k -space.

In order to determine the effective mass m^* at the centre of the Brillouin zone Γ we fitted the maximum of the valence band edge with a parabola $E_B=f(k)$ as depicted in Fig.3. From the fit parameters, we obtain via

$$\frac{1}{m^*} = \frac{1}{\hbar^2} \frac{f^2 E}{fk^2}$$

an effective mass for the chalcopyrite CuInS_2 of

$$|m^*/m_e|=0.45 \pm 0.06$$

In summary, we have presented unprecedented measurements of the valence band structure of a bulk CuInS_2 crystal. From the curvature of the valence band maximum we determined the effective mass of the material as $m^*=0.45 m_e$, which is similar to other semiconductor compounds such as GaAs. The information obtained here will later be compared to the electronic structure of epitaxial CuInS_2 films, which is subject to ongoing research.

- [1] R. Hunger *et al.*,
BESSY annual report (2004)
[2] J.E. Jaffe, A. Zunger,
Phys. Rev. B **28**, 5822 (1983)

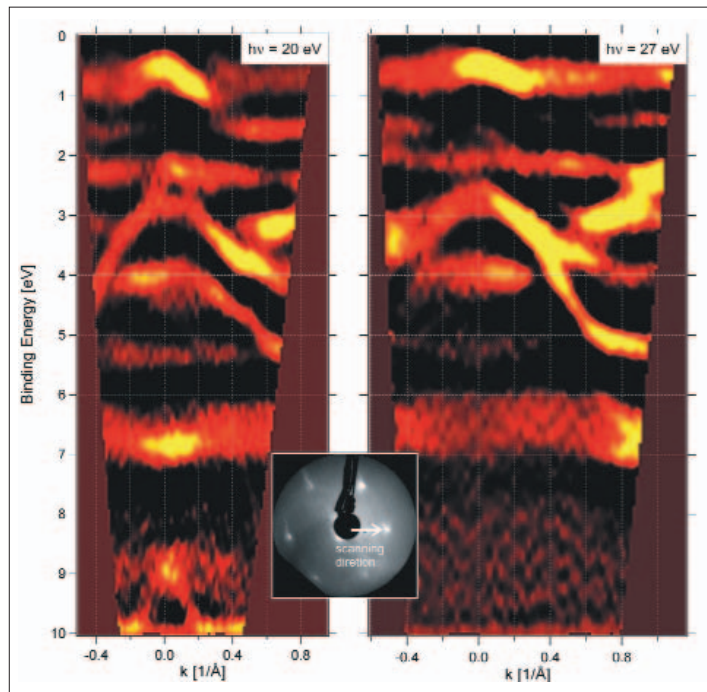


Fig. 2: Colour scale plots of the CuInS_2 valence band structure along a high symmetry path in the (112) face determined by angle resolved photoemission spectroscopy for two different excitation energies $h\nu=20\text{ eV}$ (left) and $h\nu=27\text{ eV}$ (right). Bright regions correspond to minima of the second derivative of the spectra.

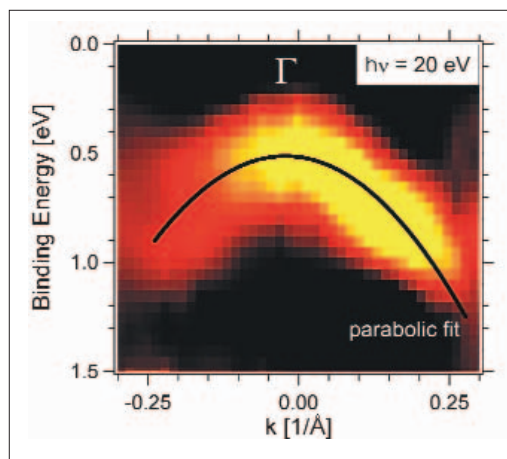
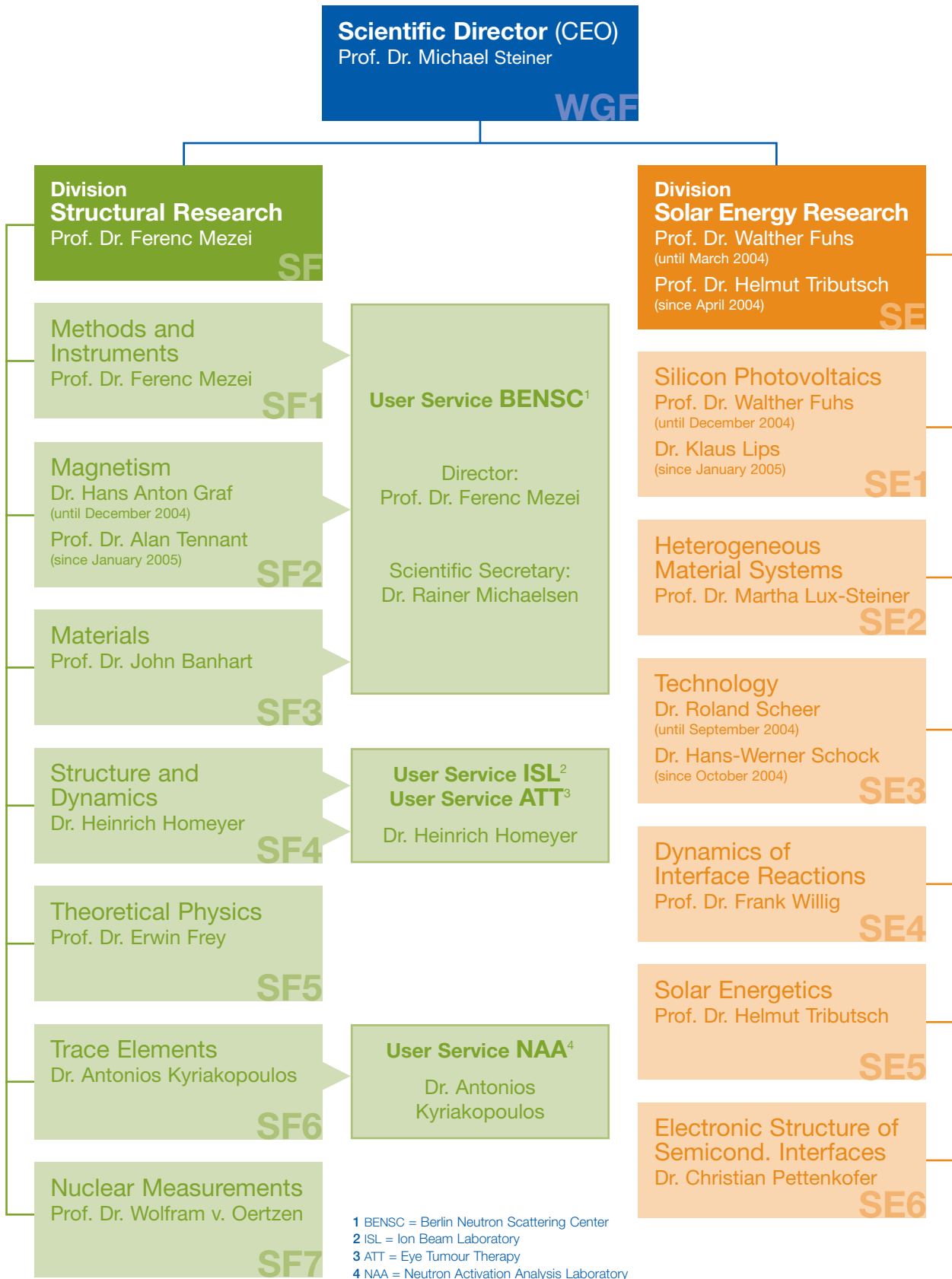


Fig. 3: Parabolic fit of the valence band maximum for determining the effective mass m^* .

HMI – Scientific Departments



Imprint

1. Edition
April 2005

Annual Report 2004
Selected Results
HMI-B 602

Published by

Hahn-Meitner-Institut Berlin GmbH
Glienicker Str. 100
14109 Berlin
Germany

info@hmi.de
<http://www.hmi.de>
Phone: (+49) (0) 30-8062-0
Fax: (+49) (0) 30-8062-2181

Member of the Helmholtz Association

Concept and Coordinating Editor

Dr. Paul Piwnicki
piwnicki@hmi.de

Coordination Solar Energy

Dr. Thomas Riedle
riedle@hmi.de

Book Design

focus werbeagentur, Potsdam
www.focuspotsdam.de

Printing

Druckerei Rüss, Potsdam
www.druckerei-ruess.de

© 2005 Hahn-Meitner-Institut

